Optical Switching via Quantum Interference Effects in a Multilevel Atomic System

By:

Ken Salit

INTRODUCTION

An all-optical switch is one that allows one beam of light, typically called the probe, to be controlled by another, typically called the switching beam. For some types of switches, the presence of this switching beam may control whether or not the probe is present at the output. All-optical switches have far reaching applications in both quantum and classical information processing [1,2,3,4].

All-optical switches may be used in classical communication. For long distance communication most signals may be carried in the form of light guided by optical fiber. This method is more efficient than sending signals electronically over long distances since the signal experiences less attenuation over long distances than electronic signals over standard transmission lines. Currently, however, switching within the network must take place electronically. Typically light brought by fibers needs to be converted to an electronic signal by optical to electronic transducers, processed electronically, and then converted back to an optical signal. An efficient all-optical switch, however, could eliminate the need for fiber to copper connections by being able to process the signal while in optical form.

In principle, such a switch could work at a single photon level, allowing direct control of one single photon pulse by another. This could be useful to the field of quantum information processing. This switch could serve as a way of producing entangled states, achieving non-demolition measurements, or implementing an optical logic gate, which in turn may have direct uses in the field of quantum computation. More immediately, a low light level switch could play

an important role in the field of classical information processing by allowing the switching of different individual channels in a many channel system, at a fraction of the input optical power required by current all-optical switches.

Most current all-optical switches depend on intense interactions between light and nonlinear media which may be extremely inefficient. The need for high switching beam powers has prevented all-optical switching from being very useful in most applications. Our research has been primarily aimed at increasing the strength of interactions between light and matter to produce more efficient switches. We have studied several different types of all-optical switches in atomic media. Our methods employ optical resonators and tapered optical nano-fibers which increase the intensity of the switching beam, thereby increasing the interaction strength.

The switching experiments discussed here are performed in Rubidium 85 atoms. One method for switching makes use of cold atoms in a magneto optical trap. Since trapped atoms can have very narrow resonance linewidths, it will be shown that switches in cold atoms can operate at extremely low input powers. Another type of switching is performed in hot Rubidium vapor. Due to Doppler broadening and transit time effects these atoms have a significantly larger resonance linewidth. This can produce broadband high speed switching, at the expense of having to increase, somewhat, the input power.

This thesis will be divided up in the following way. First I will review the theory of relevant atom-field interactions, including two level systems, three level systems, and the calculation of dipole matrix elements. I will then discuss the theory behind optical forces on atoms, saturated absorption, and all optical

switching for different configurations. Next I will discuss the development of the experimental apparatus, which includes the theory and experimental details of Magneto Optical Traps (MOTs), as well as tools which enhance atom-field interactions including cavities and tapered nano-fibers. Lastly I will discuss results obtained from various switching experiments. I will follow this section with an appendix which will include code for various simulations including saturated absorption, dipole matrix element calculations, cavity mode matching calculations, and two and three level system behavior.

THEORY

Atom-field interactions

In this section I will discuss the theory behind two level atomic systems, three level systems, and matrix elements for electric dipole transitions.

1.) Two-Level systems

I will first solve the Schrodinger equation for the case of a two level atomic interaction with a time dependent electric field [5,6, 7, 8]. For now, we will assume two level atom-field interaction and work in the basis for which the atomic energy eigenstates are

(1.1) $|1\rangle = \begin{bmatrix} 1 \\ 0 \end{bmatrix}$ and $|2\rangle = \begin{bmatrix} 0 \\ 1 \end{bmatrix}$

and any general state can be written as

(1.2) $\psi(t) = c_1(t)|1\rangle e^{-i\omega_1 t} + c_2(t)|2\rangle e^{-i\omega_2 t}$

This state evolves according to Schrodinger equation

(1.3) $i\hbar \frac{\partial \psi}{\partial t} = H\psi$

First note that the energy of an atom at rest interacting with an external time dependent electric field can be written as

(1.4) $H = H_0 + eE(r,t)\cdot\vec{r}$

where H_0 is the unperturbed atomic Hamiltonian

(1.5) $H_0 = \hbar \begin{bmatrix} \omega_1 & 0 \\ 0 & \omega_2 \end{bmatrix}$

and $H_I = eE(r,t)\cdot\vec{r}$ is the energy due to the dipole interaction where e is the electric charge, $E(x,t) = E_0\hat{x}\cos(kz)\cos(\omega t + \phi)$ is the electric field, and

$r = r_0\left(|1\rangle\langle 2| + |2\rangle\langle 1|\right)$ is the coordinate operator. We can rewrite H in the chosen basis as

$$(1.6)\quad H = \hbar\begin{bmatrix} \omega_1 & \frac{\Omega}{2}e^{i(\omega t+\phi)} \\ -\frac{\Omega}{2}e^{-i(\omega t+\phi)} & \omega_2 \end{bmatrix}$$

where $\Omega = \frac{eE}{\hbar}\langle 1|r|2\rangle$ is known as the Rabi frequency. This Hamiltonian takes into account the dipole approximation, where k^{-1} is much larger than the separation between the electron and nucleus, as well as the rotating wave approximation for which we assume $\langle 1|H|2\rangle \approx \frac{\Omega_0}{2}e^{i(\omega t+\phi)}$.

In order to solve for $\psi(t)$ we first make a transformation to remove the time dependence from the Hamiltonian. We then solve the time independent Schrodinger equation. Finally we transform back to the time dependent basis to solve for the complete, time dependent wave function.

The first step is to make the transformation with a matrix

$$(1.7)\quad Q = \begin{bmatrix} e^{i(\theta_1 t+\xi_1)} & 0 \\ 0 & e^{i(\theta_2 t+\zeta_2)} \end{bmatrix}$$

Such that

(1.8) $Q^{-1} = Q^{*}$

and

(1.9) $\dot{Q} = iMQ$

where

(1.10) $M = \begin{bmatrix} \theta_1 & 0 \\ 0 & \theta_2 \end{bmatrix}.$

We wish to solve the Schrodinger equation (1.3). By applying the Q transformation we find

(1.11) $i\hbar \frac{d(Q|\psi\rangle)}{dt} = i\hbar\left[(\dot{Q}|\psi\rangle + Q|\dot{\psi}\rangle\right] = i\hbar\left[(\dot{Q}|\psi\rangle + Q(\frac{-i}{\hbar}H|\psi\rangle))\right]$

This can be rewritten as

(1.12) $i\hbar \frac{d(Q|\psi\rangle)}{dt} = -\hbar M(Q|\psi\rangle + QHQ^{-1}Q|\psi\rangle))$.

Letting $|\tilde{\psi}\rangle = (Q|\psi\rangle$ this can be expressed as

(1.13) $$i\hbar\frac{d\left|\tilde{\psi}\right\rangle}{dt}=-\hbar M\left|\tilde{\psi}\right\rangle+QHQ^{-1}\left|\tilde{\psi}\right\rangle.$$

Next, if we let

(1.14) $$\tilde{H}=-\hbar M+QHQ^{-1}$$

we find

(1.15) $$\tilde{H}=\hbar\begin{bmatrix}\omega_1-\theta_1 & \frac{\Omega}{2}e^{i(\omega+\theta_1+\xi_1-\theta_2-\xi_2)t+i\phi}\\ \frac{\Omega}{2}e^{-i(\omega+\theta_1+\xi_1-\theta_2-\xi_2)t-i\phi} & \omega_2-\theta_2\end{bmatrix}.$$

If we choose $\theta_2-\theta_1=\omega$ and let $\theta_1=\omega_1$, $\xi_1=0$, and $\xi_2=\phi$ we find

(1.16) $$\tilde{H}=\hbar\begin{bmatrix}0 & \frac{\Omega}{2}\\ \frac{\Omega}{2} & -\delta\end{bmatrix}$$

where $\delta=\omega-(\omega_2-\omega_1)$ is the laser detuning. Note that all time dependence has been removed from this effective Hamiltonian. The time independent effective Schrodinger equation may now be written as

(1.17) $$i\hbar\frac{d|\tilde{\psi}\rangle}{dt}=\tilde{H}|\tilde{\psi}\rangle.$$

We can now find the general solution in the following way. First note that if we write the solution for $|\tilde{\psi}\rangle$ in terms of the eigenstates of $\tilde{H}$ (which form a complete orthogonal set) such that

(1.18) $$|\tilde{\psi}(t)\rangle=\sum c_n(t)|n\rangle$$

Putting this into equation [1.17] we see

(1.19) $$i\hbar\sum\dot{c}_n(t)|n\rangle=\sum E_n c_n(t)|n\rangle$$

where E_n are the eigen-energies associated with the Hamiltonian eigenstates. Multiplying by the eigenstate $\langle m|$ from the left, we find

(1.20) $$i\hbar\sum\dot{c}_n(t)\langle m|n\rangle=\sum E_n c_n(t)\langle m|n\rangle$$

and since $\langle m|n\rangle=\delta_{mn}$, we find

(1.21) $$i\hbar\dot{c}_n(t)=E_n c_n$$

for which

(1.22) $c_n(t) = c_n(t=0)e^{-i\frac{E_n}{\hbar}t} \equiv c_{n0}e^{-i\frac{E_n}{\hbar}t}$.

The general solution can then be written as

(1.23) $\left|\tilde{\psi}(t)\right\rangle = \sum c_{n0}e^{-i\frac{E_n}{\hbar}t}\left|n\right\rangle$.

If we take any wave function at time t=0 and write it in terms of the eigenstates of the Hamiltonian, this solution shows how to propagate the wave function in time. In general, the eigenstates of the time independent Hamiltonian are

(1.24) $\left|+\right\rangle = \begin{bmatrix} \frac{\delta + \sqrt{\delta^2 + \Omega^2}}{\Omega} \\ 1 \end{bmatrix}$ *and* $\left|-\right\rangle = \begin{bmatrix} \frac{\delta - \sqrt{\delta^2 + \Omega^2}}{\Omega} \\ 1 \end{bmatrix}$

with corresponding eigen-energies $E_+ = \frac{\hbar}{2}(-\delta + \sqrt{\delta^2 + \Omega^2})$ and

$E_- = \frac{\hbar}{2}(-\delta - \sqrt{\delta^2 + \Omega^2})$. These eigenstates are referred to as the dressed states. The energies associated with the dressed states are referred to as light shifted energies and are shown schematically below.

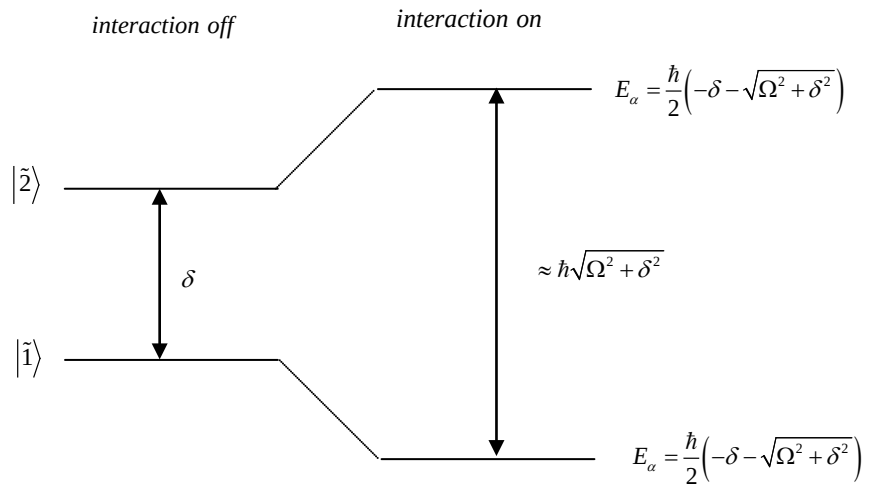

Figure 1.1: Light shifted dressed states

This diagram represents the eigenstates for the cases for which a field is interacting with the atoms (right side) and for which a field is not interacting (left side). When the interaction is off, the energies of the system are the sum of the photon and atomic energies. When the interaction is turned on, the states are shifted in energy due to the dipolar interaction between the atom and field. For $\delta >> \Omega$, this light shift is approximately equal to $\frac{\Omega^2}{4\delta}$. This shift in energy can be made useful for optical switching as well as other QIT applications [9,10].

To understand the behavior of the effective Schrodinger equation, let us analyze the simple case for $\delta = 0$. For this case

(1.25) $|+\rangle = \begin{bmatrix} 1 \\ 1 \end{bmatrix}$ *and* $|-\rangle = \begin{bmatrix} -1 \\ 1 \end{bmatrix}$

and the eigen-energies are $E_+ = \frac{\Omega}{2}$ and $E_- = -\frac{\Omega}{2}$. Note that in terms of the unperturbed atomic eigenstates, the ground and excited states can be written as

(1.26) $$|1\rangle = \begin{bmatrix} 1 \\ 0 \end{bmatrix} = \frac{1}{2}\begin{bmatrix} 1 \\ 1 \end{bmatrix} - \frac{1}{2}\begin{bmatrix} -1 \\ 1 \end{bmatrix} = \frac{1}{2}|+\rangle - \frac{1}{2}|-\rangle$$

(1.27) $$|2\rangle = \begin{bmatrix} 0 \\ 1 \end{bmatrix} = \frac{1}{2}\begin{bmatrix} 1 \\ 1 \end{bmatrix} + \frac{1}{2}\begin{bmatrix} -1 \\ 1 \end{bmatrix} = \frac{1}{2}|+\rangle + \frac{1}{2}|-\rangle$$

If we start with the initial condition that the atom is in the ground state, $c_{10} = 1$ and $c_{20} = 1$, then $c_{+0} = \frac{1}{2}$ and $c_{-0} = -\frac{1}{2}$. Our wave function can then be written as

(1.28) $$|\tilde{\psi}(t)\rangle = \frac{1}{2}|+\rangle e^{-i\frac{\Omega}{2}t} - \frac{1}{2}|-\rangle e^{+i\frac{\Omega}{2}t}$$

which may be rewritten as

(1.29) $$|\tilde{\psi}(t)\rangle = \frac{1}{2}\begin{bmatrix} e^{-i\frac{\Omega}{2}t} + e^{+i\frac{\Omega}{2}t} \\ e^{-i\frac{\Omega}{2}t} - e^{+i\frac{\Omega}{2}t} \end{bmatrix} = \begin{bmatrix} \cos\left(\frac{\Omega}{2}t\right) \\ -i\sin\left(\frac{\Omega}{2}t\right) \end{bmatrix} = \cos\left(\frac{\Omega}{2}t\right)|1\rangle - i\sin\left(\frac{\Omega}{2}t\right)|2\rangle$$

The oscillations between the ground and excited states are referred to as Rabi flopping.

We can also find the solution for the wave function in the frame not rotating with the field. To do this we simply apply the inverse of the Q matrix to the solution of the wave function so that

(1.30)

$$\left|\psi(t)\right\rangle = Q^{-1}\left|\tilde{\psi}(t)\right\rangle = \begin{bmatrix} \cos\left(\frac{\Omega}{2}t\right)e^{-i\omega_1 t} \\ -i\sin\left(\frac{\Omega}{2}t\right)e^{-i(\omega_2+\phi)t} \end{bmatrix} = \cos\left(\frac{\Omega}{2}t\right)e^{-i\omega_1 t}\left|1\right\rangle - i\sin\left(\frac{\Omega}{2}t\right)e^{-i(\omega_2+\phi)t}\left|2\right\rangle.$$

In general a statistical ensemble of atoms is present, and a density matrix representation is needed. The density matrix is written as

(1.31) $$\rho = \begin{bmatrix} \rho_{11} & \rho_{12} \\ \rho_{21} & \rho_{22} \end{bmatrix}$$

where $\rho_{11} = c_1^2$, $\rho_{22} = c_2^2$ and $\rho_{12} = c_1 c_2^* = \rho_{21}^*$. When normalized, ρ_{11} determines the population of the ground state, ρ_{22} determines the population of the excited state, and ρ_{12} determines the fraction of atoms in a coherent superposition of the ground and excited states. ρ_{12} is related to the dipole moment of the field through

(1.32) $$\left\langle x\right\rangle = Tr(\rho x) = x_0(\rho_{12} + \rho_{21}^*).$$

To find the density matrix in the rotated frame, we apply the Q transformation to ρ and find

(1.33) $\tilde{\rho} = \begin{bmatrix} \tilde{\rho}_{11} & \tilde{\rho}_{12} \\ \tilde{\rho}_{21} & \tilde{\rho}_{22} \end{bmatrix}$

where

(1.34) $\tilde{\rho}_{12} = \rho_{12} e^{-i\omega t}$

(1.35) $\tilde{\rho}_{21} = \rho_{21} e^{i\omega t}$

(1.36) $\tilde{\rho}_{11} = \rho_{11}$

(1.37) $\tilde{\rho}_{22} = \rho_{22}$.

Note that in the frame evolving with the electric field, a phase associated with $\tilde{\rho}_{12}$ would tell us how out of phase the motion of the dipole moment is with the driving electric field. If $\tilde{\rho}_{12}$ is purely imaginary, then the dipole motion is 90 degrees out of phase with the driving field, radiating a field 180 degrees out of phase with the driving field (shown from the solution for dipole radiation) [11]. The driving field adds destructively with the radiated field diminishing in intensity as it travels through the medium. This shows qualitatively that imaginary $\tilde{\rho}_{12}$ is associated with absorption (and gain). If the phase of $\tilde{\rho}_{12}$ is purely real, then the dipole motion may be in phase with the driving field, radiating a field 90 degrees out of phase with the driving field. As the driving

field adds with the radiated field, a net field is produced that is behind in phase to the original driving field. This shows qualitatively that the real part of $\tilde{\rho}_{12}$ is associated with index of refraction. We will soon see how these associations of absorption and index of refraction are quantitatively connected to polarization.

To find how $\tilde{\rho}$ evolves with time we need to solve the optical Bloch equations which are written as:

(1.38) $$\dot{\tilde{\rho}} = \tilde{\rho}_H + \dot{\tilde{\rho}}_{phen}$$

where

(1.39) $$\tilde{\rho}_H = \frac{i}{\hbar}[\rho, H]$$

and $\dot{\tilde{\rho}}_{phen}$ is the phenomenologically added term which accounts for decay

(1.40) $$\dot{\tilde{\rho}}_{phen} = \begin{bmatrix} \Gamma\tilde{\rho}_{22} & -\frac{\Gamma}{2}\tilde{\rho}_{21} \\ -\frac{\Gamma}{2}\tilde{\rho}_{12} & -\Gamma\tilde{\rho}_{22} \end{bmatrix}.$$

We can plot the solutions to $\tilde{\rho}_{11}$ and $\tilde{\rho}_{22}$ to observe how the state evolves when decay is included. This is done by solving the optical Bloch equations, and then making the linear approximation that

(1.41) $\tilde{\rho}(t) \approx \tilde{\rho}(t-\Delta t) + M\,\tilde{\rho}(t-\Delta t)\Delta t$

where M is the matrix soltution for $\dot{\tilde{\rho}}$ governed by the Bloch equations. Below I have shown plots for $\Omega < \Gamma$ and for $\Omega > \Gamma$.

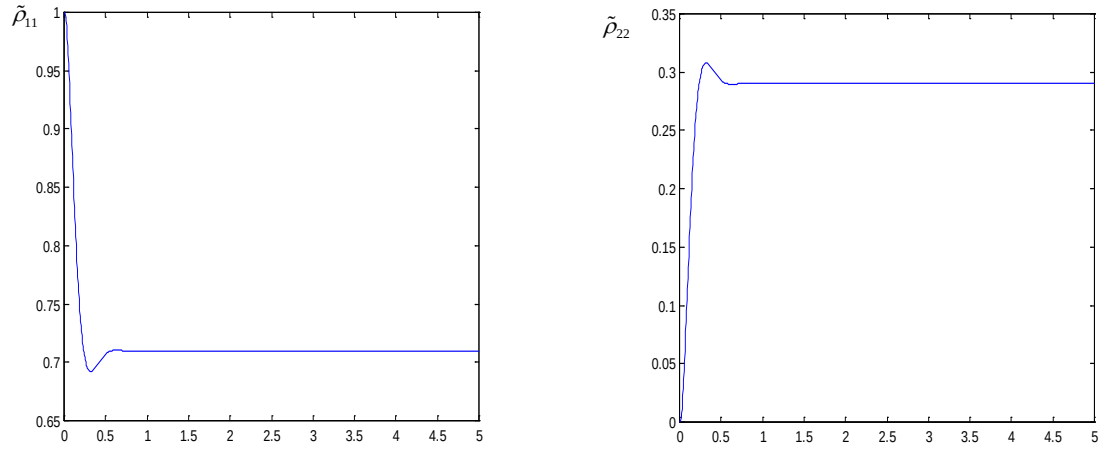

Figure 1.2a: Ground and excited state population as function of time for $\Omega < \Gamma$

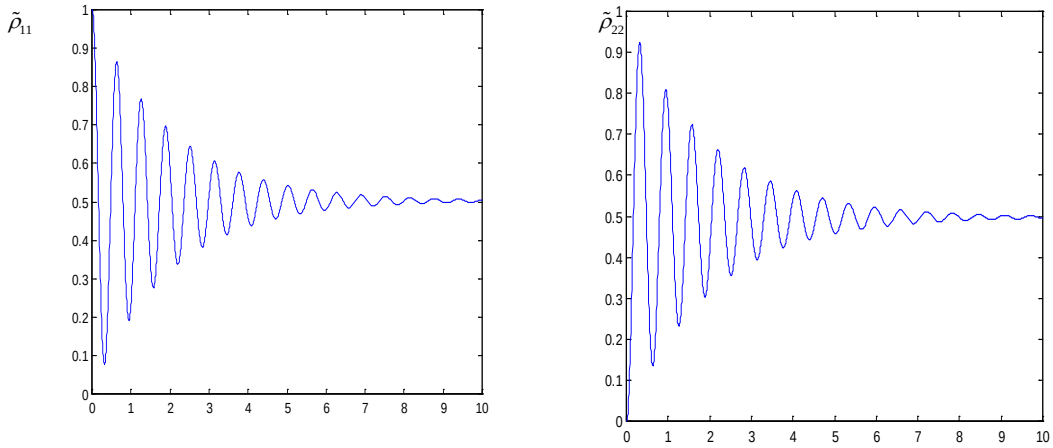

Figure 1.2b: Ground and excited state population as function of time for $\Omega > \Gamma$

We find that Rabi oscillations become damped, and that both $\tilde{\rho}_{11}$ and $\tilde{\rho}_{22}$ evolve to a steady state. Above saturation intensity, when $\Omega > \Gamma$, the steady state value for both $\tilde{\rho}_{11}$ and $\tilde{\rho}_{22}$ is $\frac{1}{2}$. We can find the steady state solutions directly by solving the optical Bloch equations for $\dot{\rho} = 0$ along with the condition $\tilde{\rho}_{11} + \tilde{\rho}_{22} = 1$, and we find.

(1.42) $$\tilde{\rho}_{11} = 1 - \frac{\Omega^2}{2\Omega^2 + \Gamma^2 + 4\delta^2}$$

(1.43) $$\tilde{\rho}_{12} = \frac{i(\Omega\Gamma - 2i\Omega\delta)}{2\Omega^2 + \Gamma^2 + 4\delta^2}$$

(1.44) $$\tilde{\rho}_{21} = \frac{-i(\Omega\Gamma + 2i\Omega\delta)}{2\Omega^2 + \Gamma^2 + 4\delta^2}$$

(1.45) $$\tilde{\rho}_{22} = \frac{\Omega^2}{2\Omega^2 + \Gamma^2 + 4\delta^2}.$$

One relation that will be important when discussing optical forces will be

(1.46) $$\tilde{\rho}_{12} - \tilde{\rho}_{21} = \frac{2i\Gamma}{\Omega}\tilde{\rho}_{22}.$$

Next, we discuss the behavior of a field traveling through a two level material. We can do this in the following way. First using the expression

(1.47) $P = \varepsilon_0 \chi E$

where P is the polarization, E is the electric field, and χ is the susceptibility. Plugging this into the wave equation

(1.48) $-\nabla^2 \vec{E} - \mu_0 \varepsilon_0 \frac{d^2 \vec{E}}{dt^2} = \mu_0 \frac{d^2 \vec{P}}{dt^2}$

we find

(1.49) $\nabla^2 E = \tilde{\varepsilon} \mu_0 \frac{\partial^2 E}{\partial t^2}$

where

(1.50) $\tilde{\varepsilon} \equiv \varepsilon_0 (1 + \chi) = \varepsilon_0 \left(1 + \frac{P}{\varepsilon_0 E} \right).$

If we assume traveling wave solutions of the form $E = E_0 e^{i(kz - \omega t)}$ we find that k can be split into real and imaginary parts in the following way

(1.51) $k = \sqrt{\tilde{\varepsilon} \mu_0} \omega \equiv k_R + i k_I .$

where the imaginary part k_I is associated with gain (k_I <0) or loss (k_I >0) We can also write the polarization as

(1.52) $P = Ne\langle x \rangle$

where N is the atomic density, e is the charge of the electron and $\langle x \rangle$ is the average dipolar separation. Using the quantum mechanical description of the dipolar separation, namely $\langle x \rangle = Tr(x\rho) = x_0\rho_{12} + c.c.$ where x_0 is the average distance between the electron and proton, as well as the definition of the Rabi frequency, and dropping the complex conjugate terms, we find

(1.53) $P = N\frac{\hbar\Omega}{E}\rho_{12}$

inserting this into equation (1.50) we find

(1.54) $k = \left(\mu_0\omega^2\varepsilon_0\right)^{1/2}\left[1+\frac{N\hbar\Omega}{\varepsilon_0 E^2}\rho_{12}\right]^{1/2}$

Taking a Taylor expansion in the second term and plugging in explicitly for ρ_{12} we find that the absorption coefficient can be written as:

(1.55) $$\alpha \equiv k_I = \frac{k_0 \Omega \hbar N}{\varepsilon_0 \mathrm{E_0}^2} \mathrm{Im}(p_{12}) = \frac{k_0 \Omega \hbar N}{\varepsilon_0 \mathrm{E_0}^2} \frac{\Omega \Gamma}{\Gamma^2 + 2\Omega^2 + 4\delta^2}.$$

In terms of the intensity we find the absorption coefficient to be:

(1.56) $$\alpha = \frac{k\hbar N \Gamma \frac{I}{I_{sat}}}{\varepsilon_0 (2\eta I)\left(1 + 2\frac{I}{I_{sat}}\right)}.$$

A plot of the absorption coefficient is plotted below as a function of δ.

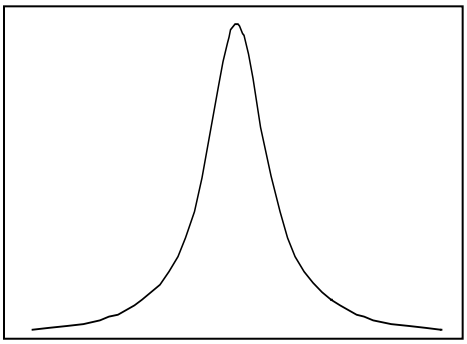

Figure 1.3: Lineshape of absorption coefficient as a function of detuning

The real part of k is associated with the phase velocity of the field, and thus related to the index of refraction $n = \frac{c}{v}$. We find that

(1.57) $$k_R = k_0 \left[1 + \frac{N\hbar\Omega}{2\varepsilon_0 E^2} \mathrm{Re}(\rho_{12})\right].$$

From this expression, we find the index of refraction can be written as

$$(1.58)\quad n=\left[1+\frac{N\hbar\Omega}{2\varepsilon_0 E^2}\mathrm{Re}(\rho_{12})\right]$$

and is plotted below as a function of δ.

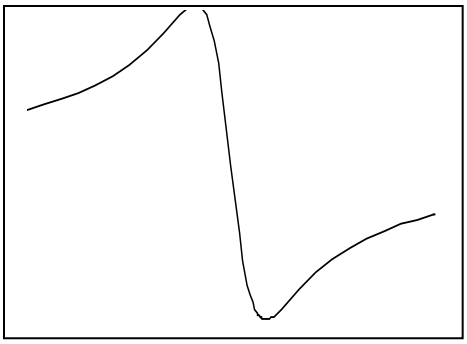

Figure 1.4: Lineshape of refractive index as a function of detuning

Note that a pulse has many frequency components, each of which will experience a different index of refraction. For this reason, the group velocity of the pulse is related to the derivative of the index in respect to the frequency. For a negative dispersion such as that shown above fast light can be achieved for which there are many applications [12,13,14]. In a two level system, however, this is accompanied by absorption.

2.) Three-Level systems

I will now discuss the basic theory of the three level Λ-system. If two fields, $E_{12}=\hat{\varepsilon}_{12}E_{012}\cos(k_a z-\omega_a t+\phi_a)$ and $E_{32}=\hat{\varepsilon}_{32}E_{032}\cos(k_b z-\omega_b t+\phi_b)$, are

applied to a semi-classical three level atomic system, the Hamiltonian should consist of the atomic energy terms and a dipole interaction term $H_{interaction} = \vec{d} \cdot \vec{E}$:

(2.1)

$$H_{atom} + H_{interaction} = \hbar \begin{pmatrix} \omega_1 & \Omega_{12}\cos(k_a z - \omega_a t + \phi_a) & 0 \\ \Omega_{12}\cos(k_a z - \omega_a t + \phi_a) & \omega_2 & \Omega_{32}\cos(k_b z - \omega_b t + \phi_b) \\ 0 & \Omega_{32}\cos(k_b z - \omega_b t + \phi_b) & \omega_3 \end{pmatrix}$$

and our atomic energy level diagram appears as:

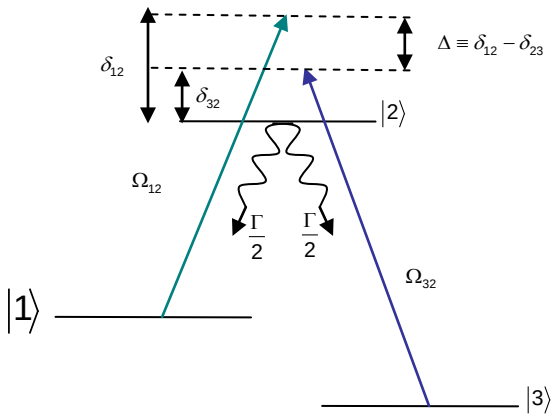

Figure 2.1: 3 Level Semi-classical System

After making the dipole approximation, the rotating wave approximation, and performing the rotating wave transformation using the Q-matrix

(2.2) $$Q = \begin{bmatrix} e^{i\theta_1 t} & 0 & 0 \\ 0 & e^{i\theta_2 t} & 0 \\ 0 & 0 & e^{i\theta_3 t} \end{bmatrix}$$

(2.2a) $\theta_1 = \omega_1$

(2.2b) $\theta_2 = \omega_a + \omega_1$

(2.2c) $\theta_2 = (\omega_a - \omega_b) + \omega_1$,

our effective time independent Hamiltonian becomes:

(2.3) $$\tilde{H} = \begin{pmatrix} 0 & \frac{\Omega_{12}}{2} & 0 \\ \frac{\Omega_{12}}{2} & -\delta_{12} & \frac{\Omega_{32}}{2} \\ 0 & \frac{\Omega_{32}}{2} & -\Delta \end{pmatrix}$$

where:

(2.4) $\Omega_{12} = \frac{d_{12}E_{012}}{\hbar}$

(2.5) $\Omega_{32} = \frac{d_{32}E_{032}}{\hbar}$

(2.6) $\delta_{12} = \omega_a - (\omega_2 - \omega_1)$

(2.7) $\delta_{32} = \omega_b - (\omega_2 - \omega_3)$

Note that in this time independent basis our energy level diagram may be presented as:

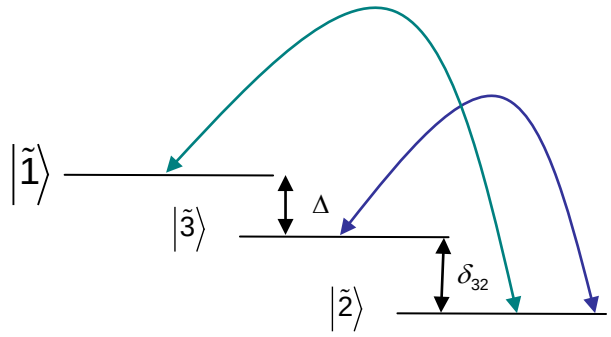

Figure 2.2: 3 Level Semi-classical System in Time Independent Basis

If we let our difference detuning $\Delta = 0$, we find an important eigenstate of our time independent Hamiltonian for which there is no probe absorption:

$$(2.8)\quad |-\rangle \equiv \frac{-\Omega_{32}|1\rangle + \Omega_{12}|3\rangle}{\sqrt{{\Omega_{32}}^2 + {\Omega_{12}}^2}}$$

which is known as the dark state, and the resulting induced transparency is referred to as Λ-type Electromagnetically Induced Transparency, (EIT) [15,16,17,18,19]. In this state the transition amplitudes between $|1\rangle$ and $|2\rangle$, and between $|3\rangle$ and $|2\rangle$ cancel one another, and the result is that the excited state remains unpopulated for all time.

This can be seen by restoring time dependence and solving for the rate of transition to the excited state $\dot{c}_2$:

$$(2.9)\,\dot{c}_2 = c_1\langle 1|H|2\rangle e^{-i\delta_{12}t/\hbar} + c_3\langle 3|H|2\rangle e^{-i\delta_{32}t/\hbar} = 0$$

Note that this state can only be dark when the difference detuning between the ground states is zero.

Next let us consider the density matrix solution for a three level system with decay. Using the decay matrix:

$$(2.10)\quad \dot{\tilde{\rho}}_{decay} = \begin{pmatrix} \frac{\Gamma}{2}\tilde{\rho}_{22} & -\frac{\Gamma}{2}\tilde{\rho}_{12} & 0 \\ -\frac{\Gamma}{2}\tilde{\rho}_{21} & -\Gamma\tilde{\rho}_{22} & -\frac{\Gamma}{2}\tilde{\rho}_{23} \\ 0 & -\frac{\Gamma}{2}\tilde{\rho}_{32} & \frac{\Gamma}{2}\tilde{\rho}_{22} \end{pmatrix}$$

and by using the Schrödinger equation we find our first order o.d.e. for the density matrix to be:

$$(2.11)\quad \dot{\tilde{\rho}} = \frac{-i}{\hbar}\left[\tilde{H}, \tilde{\rho}\right] + \dot{\tilde{\rho}}_{decay} = 0$$

Plots of $\tilde{\rho}_{11}(t)$, $\tilde{\rho}_{22}(t)$, $\tilde{\rho}_{33}(t)$ are below, showing the dynamics of the three level system. The first case is the general case for which $\Omega_{12}, \Omega_{32} < \Gamma$ and the applied fields have different detunings. The second case is for $\Omega_{12}, \Omega_{32} > \Gamma$ and the fields have the same detunings as the first case. The third plot is for $\Omega_{12}, \Omega_{32} > \Gamma$, but the difference detuning of the two fields are zero.

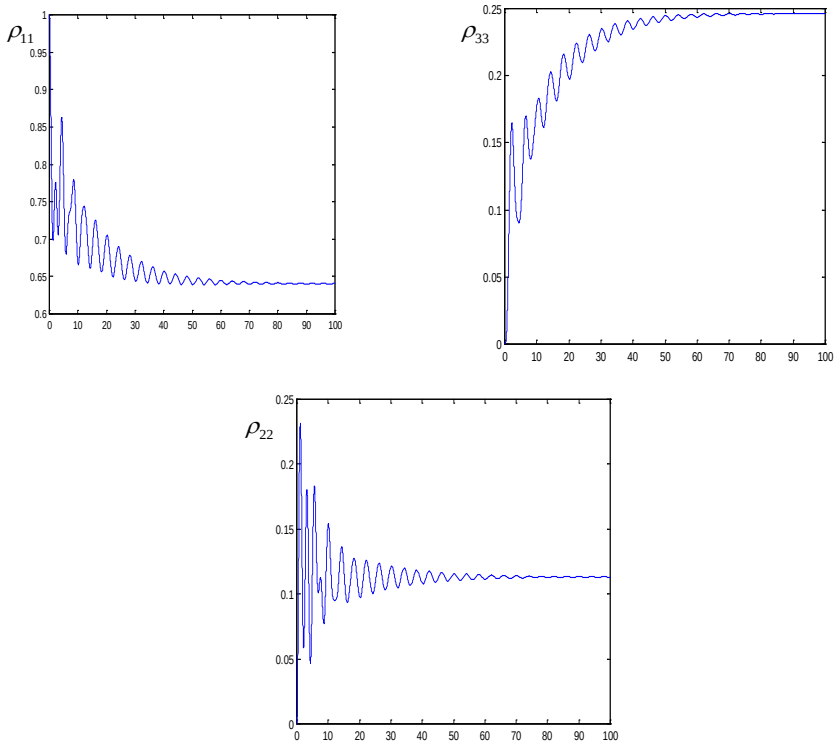

Figure 2.3a: Density matrix dynamics with different detunings and $\Omega_{12},\Omega_{32} < \Gamma$

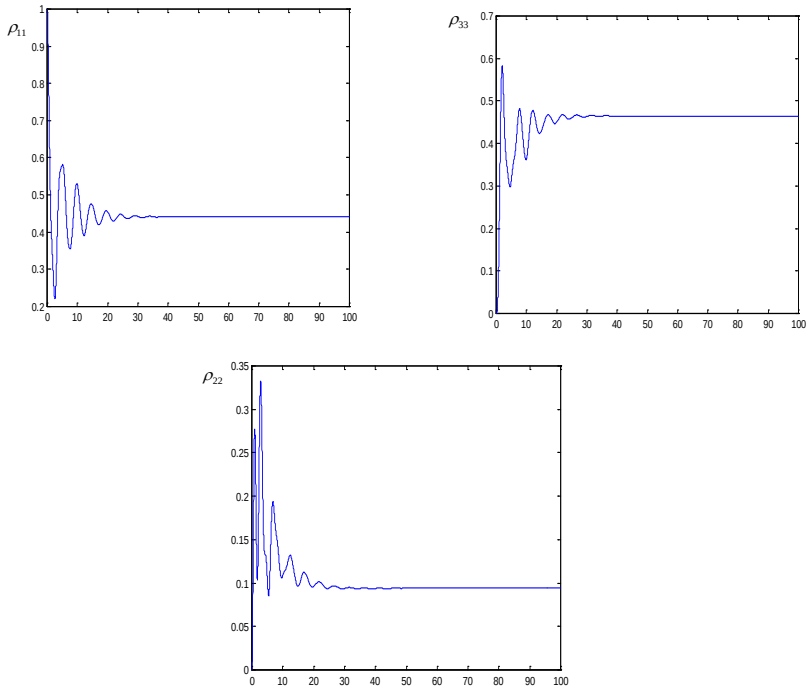

Figure 2.3b: Density matrix dynamics with different detunings and $\Omega_{12},\Omega_{32} > \Gamma$

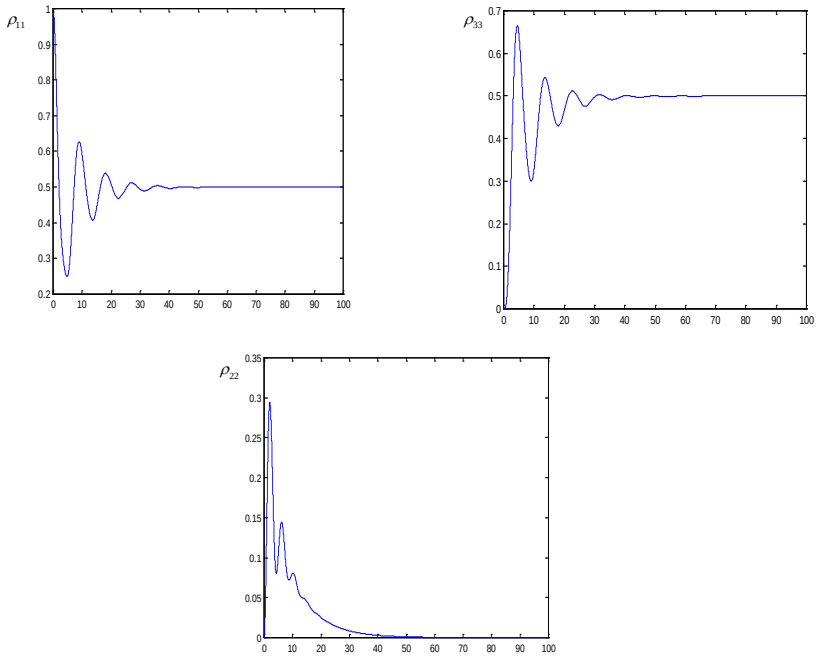

Figure 2.3c: Density matrix dynamics with matchedt detunings and $\Omega_{12},\Omega_{32} > \Gamma$

Note that when the difference detuning of the two fields is zero, the plot of $\tilde{\rho}_{22}$ shows that the steady state value becomes zero. This is the condition for which the state evolves into the dark state.

By setting $\dot{\tilde{\rho}} = 0$ we can explicitly find the steady state solution for our system. By plotting the imaginary part of $\tilde{\rho}_{12}$ as a function of frequency, we can plot the absorption of the field coupling states $|1\rangle$ and $|2\rangle$.

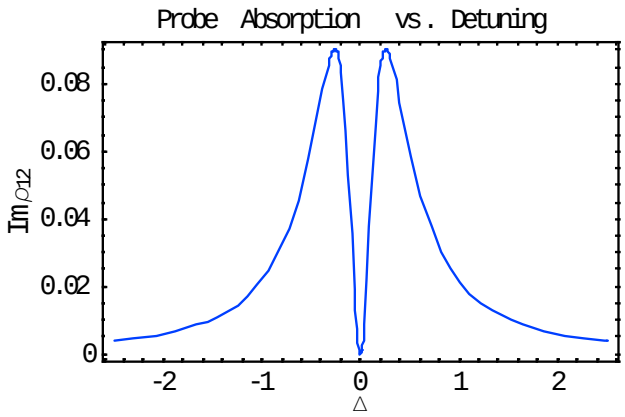

Figure 2.4: Steady State Absorption Profile of 3-Level System

We see that when the difference detuning is zero we get a large dip in our probe absorption curve. This point, where we get total transmission of the probe, again corresponds to the dark state of the three level system and is referred to as electromagnetically induced transparency (EIT). Plotting the real part of $\tilde{\rho}_{12}$, we see that this transparency is accompanied by a large positive dispersion, as shown below.

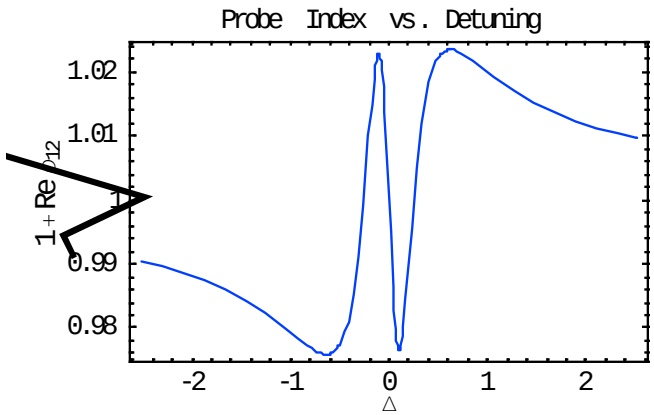

Figure 2.5: Steady State Dispersion Profile of 3-Level System

This large positive dispersion has many applications in slow light experiments [20,21,22].

If we consider the rate at which atoms are transferred from the dark state $|-\rangle$ to the bright $|+\rangle$ state where:

$$(2.12)\quad |+\rangle \equiv \frac{-\Omega_{32}|1\rangle - \Omega_{12}|3\rangle}{\sqrt{\Omega_{32}{}^2 + \Omega_{12}{}^2}}$$

we find this rate to be of the order of $\langle +|\tilde{H}|-\rangle = \Delta$. The rate at which atoms are transferred from the bright state $|+\rangle$ to the dark state $|-\rangle$, on the other hand, should be on the order of $\frac{\Omega^2}{\Gamma}$, assuming, for the moment, equal pump and probe coupling constants Ω. This can be seen in the following way. Treating the bright state $|+\rangle$ and the excited state $|2\rangle$ as a two level system, the steady state population of $|2\rangle$ would be approximately $\rho_{22} \approx \frac{\Omega^2}{\Gamma^2}\rho_{++}$. Noting that the decay rate of the excited state $|2\rangle$ is Γ, it follows that the rate at which atoms enter the dark state is approximately $\frac{\Omega^2}{\Gamma}$. This can be seen in the figure below.

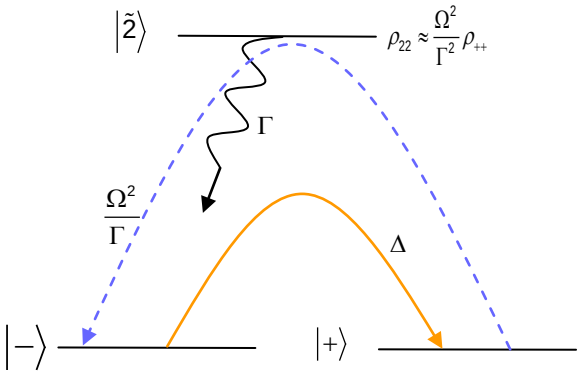

Figure 2.6: 3 Level System Consisting of Dark, Bright, and Excited States

Note that once the rate at which atoms leave the $|-\rangle$ state becomes larger than the rate at which atoms enter the $|-\rangle$ state, that is when $\Delta > \frac{\Omega^2}{\Gamma}$, atoms are no longer trapped in this dark state. From this argument we expect the linewidth of EIT to be of the order of $\frac{\Omega^2}{\Gamma}$.

If we assume that one of the fields coupling our atomic levels contains only one or few photons, we must quantize the field to properly model the behavior of the system. If we quantize the weak (probe) field for traveling wave modes we find:

$$(2.13)\quad E_{probe} = \hat{\varepsilon}\left(\frac{\hbar\omega_{12}}{2\varepsilon_0 V}\right)^{1/2}(ae^{ikz} + a^{\dagger}e^{-ikz})$$

and our field Hamiltonian becomes:

(2.14) $H_{probe} = \hbar\omega_{12}(a^{\dagger}a + \frac{1}{2})$

for which our eigenstates are photon number states with energy $(n + \frac{1}{2})\hbar\omega_{12}$, that is:

(2.15) $H_{probe}\left|n\right\rangle = (n + \frac{1}{2})\hbar\omega_{12}$.

The interaction Hamiltonian, letting $kz = 0$, becomes:

(2.16) $H_{interaction} = \vec{d}\cdot\vec{E} = \hbar g_0(a + a^{\dagger})$

where:

(2.17) $\hbar g_0 = \left\langle 1\left|\vec{d}\cdot\hat{\varepsilon}\right|2\right\rangle\left(\frac{\hbar\omega_{12}}{2\varepsilon_0 V}\right)^{1/2}$.

This will give us our total Hamiltonian matrix elements. If we repeat the same procedure for the strong (pump) field, and allowing N laser photons to interact with our 3 level system we find the Hamiltonian to be:

(2.18)

$$H = \hbar \begin{pmatrix} \omega_1 + \omega_{23}(N - \frac{1}{2}) + \frac{3}{2}\omega_{12} & \frac{g_0}{2} & 0 \\ \frac{g_0}{2} & \omega_2 + \omega_{23}(N - \frac{1}{2}) + \frac{1}{2}\omega_{12} & \frac{\sqrt{N}g_1}{2} \\ 0 & \frac{\sqrt{N}g_1}{2} & \omega_3 + \omega_{23}(N + \frac{1}{2}) + \frac{1}{2}\omega_{12} \end{pmatrix}$$

which can also be described by the energy diagram below.

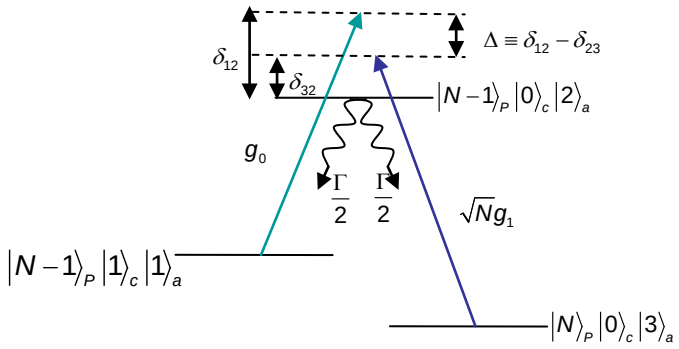

Figure 2.7: 3 Level System with quantized fields

Note that the pump is a coherent state with a large mean photon number N. The probability of measuring a particular photon number state for a given coherent state has a Poisson probability distribution of $P(n) = e^{-N}\frac{N^n}{n!}$. This distribution is shown below with variance and mean equal to N.

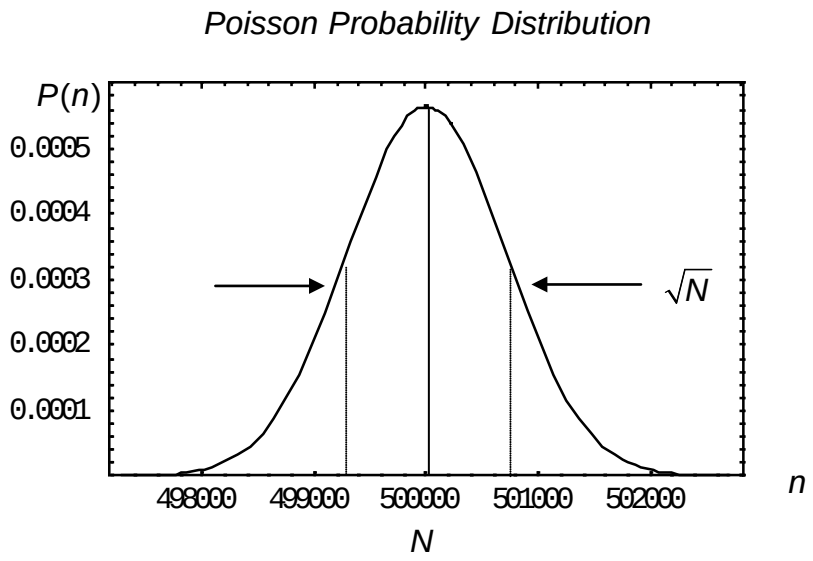

Figure 2.8: Photon number probability distribution for a coherent state

Within the standard deviation of this Poisson distribution exists a manifold of states with different pump photon number states. This is shown below.

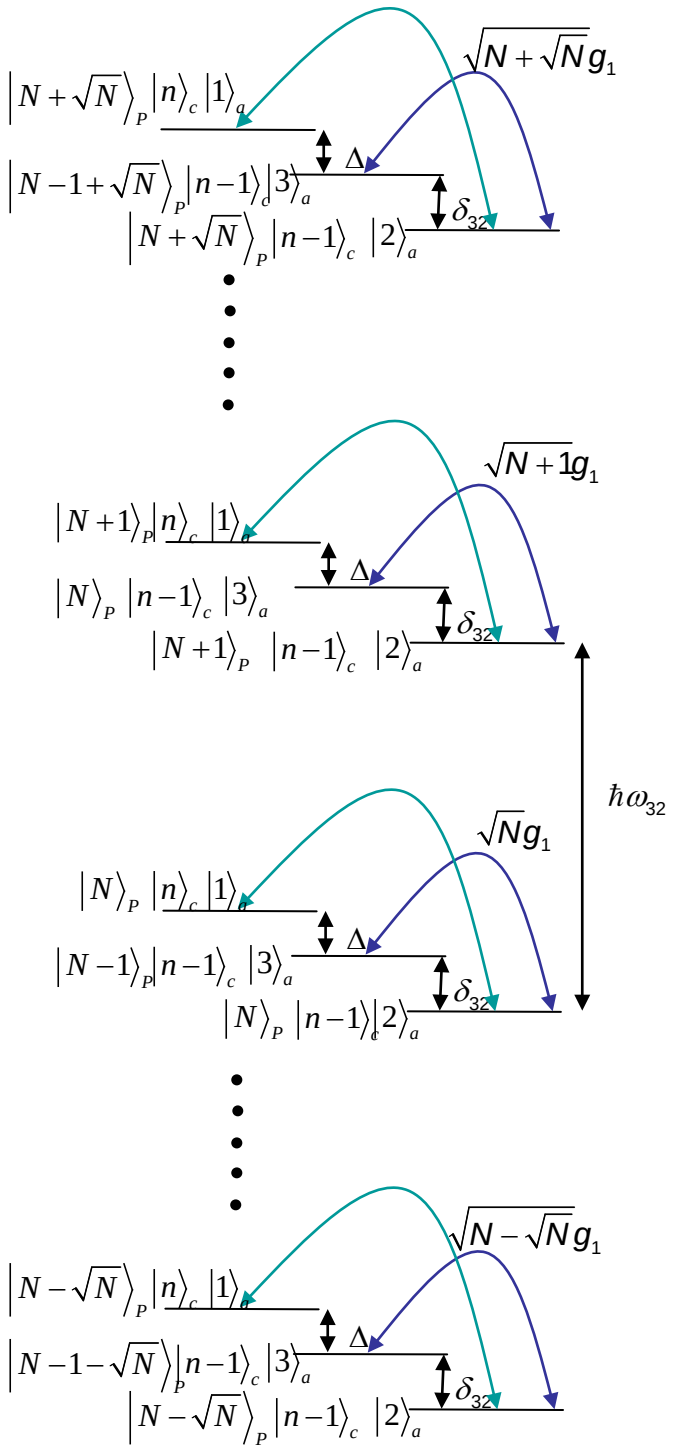

Figure 2.9: Levels in energy manifold for coherent state pump field

Note that for large N, $\sqrt{N} << N$. Therefore

$g_1\sqrt{N-\sqrt{N}} \approx g_1\sqrt{N} \approx g_1\sqrt{N+1} \approx g_1\sqrt{N+\sqrt{N}}$, so that all the systems within the pump's standard deviation have similar behavior. We therefore ignore the photon number information for the pump states, replacing $\sqrt{N}g$ with Ω_{32}.

Then, if we subtract off the common energy of the $|1\rangle_c |1\rangle_a$ state from each element we find our Hamiltonian to be:

$$(2.19)\quad H = \begin{pmatrix} 0 & \frac{g_0}{2} & 0 \\ \frac{g_0}{2} & -\delta_{12} & \frac{\Omega_{32}}{2} \\ 0 & \frac{\Omega_{32}}{2} & -\Delta \end{pmatrix}$$

which has the exact same form as $\tilde{H}$, the time independent effective Hamiltonian, derived using semi-classical methods. This assures us that all of the math done in the semi-classical regime up to this point is still valid for the fully quantized model.

Methods for using three level systems and EIT for all optical switching will be discussed further in subsequent sections.

3.) Dipole Matrix Elements

In this section, we will calculate the dipolar hyperfine transition matrix elements and find a general rule for which hyperfine fine transitions may occur.

This can also be found in references [23,24,2526]. We will begin by assuming we have an atom in the state $\left|n,F,m_f,j,i,l\right\rangle$ and we will allow the atom to interact with a near resonant field of polarization $\hat{\varepsilon}$. We will find to which final states the atom may transition, and with what relative probabilities. We will use the dipole approximation which states that since the wavelength of light is much larger than atomic distances, we will ignore spatial variation of the field, as well as only considering electric dipole interactions in the Hamiltonian.

We start with time dependent first order perturbation theory. From the Schrodinger equation we have

(3.1) $$i\hbar\frac{\partial}{\partial t}\left|\psi\right\rangle = H\left|\psi\right\rangle$$

and let

(3.2) $$H(t) = H_0 + H_1(t)$$

where

(3.3) $$H_0\left|\psi_n^{(0)}\right\rangle = E_n^{(0)}\left|\psi_n^{(0)}\right\rangle$$

H_0 is the time independent Hamiltonian, $H_1(t)$ is the time dependent interaction Hamiltonian, and $\left|\psi_n^{(0)}\right\rangle$ are the eigenstates of the unperturbed Hamiltonian. We can expand $\psi(t)$ in terms of the orthonormal basis by

(3.4) $$\left|\psi\right\rangle = \sum_n c_n(t) e^{-\frac{iE_n^{(0)}t}{\hbar}} \left|\psi_n^{(0)}\right\rangle .$$

Plugging this into the Schrodinger equation and multiplying both sides by $\left\langle\psi_m^{(0)}\right| e^{\frac{iE_m^{(0)}t}{\hbar}}$ we find that

(3.5) $$i\hbar\dot{c}_m(t) = \sum_n c_n(t) H_{mn}^{(1)} e^{i\omega_{mn}t}$$

where $H_{mn}^{(1)} \equiv \left\langle\psi_m^{(0)}\right| H_1 \left|\psi_n^{(0)}\right\rangle$ and $\omega_{mn} \equiv \frac{E_m - E_n}{\hbar}$. This shows that the rate at which transitions occur into state m from state n is proportional to the Hamiltonian matrix elements $H_{mn}^{(1)}$. In terms of the hyperfine transitions, we wish to find these elements $\mathrm{H}_{\mathrm{mn}}^{(1)} = \left\langle nF'm_f'\right| -e\vec{r}\cdot\vec{E} \left| nFm_f \right\rangle$ which will tell us the relative rates at which these transitions occur. If we represent the field by the vector $\vec{E} = \hat{\varepsilon}E(t)$, where $\hat{\varepsilon}$ is the polarization vector, then the rates at which these transitions occur are proportional to the matrix elements $\left\langle nF'm_f'\right| \vec{r}\cdot\hat{\varepsilon} \left| nFm_f \right\rangle$.

Our next step is to expand the vector $\vec{r} = x\hat{x} + y\hat{y} + z\hat{z}$ in terms of the orthogonal spherical basis states. These basis states can be written as

(3.6*a*) $\hat{u}_{cw} = \frac{1}{\sqrt{2}}(\hat{x} + i\hat{y})$

(3.6*b*) $\hat{u}_0 = \hat{z}$

(3.6*c*) $\hat{u}_{ccw} = -\frac{1}{\sqrt{2}}(\hat{x} - i\hat{y})$

Expanding the Cartesian coordinates in terms of this basis

(3.7*a*) $\hat{x} = \frac{1}{\sqrt{2}}(\hat{u}_{cw} - \hat{u}_{ccw})$

(3.7*b*) $\hat{z} = \hat{u}_0$

(3.7*c*) $\hat{y} = \frac{-i}{\sqrt{2}}(\hat{u}_{cw} + \hat{u}_{ccw})$

we find that

(3.8) $\vec{r} = x\hat{x} + y\hat{y} + z\hat{z} = \frac{1}{\sqrt{2}}(x - iy)\hat{u}_{cw} + z\hat{u}_0 - \frac{1}{\sqrt{2}}(x + iy)\hat{u}_{ccw}$

By using the definition of the spherical harmonics, namely

(3.9a) $Y_1^0 = \sqrt{\frac{3}{4\pi}}\frac{z}{r}$

and

(3.9b) $Y_1^{\pm 1} = \mp\sqrt{\frac{3}{8\pi}}\frac{(x \pm iy)}{r}$,

we find

(3.10) $\vec{r} = \sqrt{\frac{4\pi}{3}} r(Y_1^{-1}\hat{u}_{cw} + Y_1^0\hat{u}_0 + Y_1^{+1}\hat{u}_{ccw})$

Next we repeat the same procedure for the vector $\vec{E}(r) = E_x\hat{x} + E_y\hat{y} + E_z\hat{z}$ and find that

(3.11) $\vec{E}(r) = \frac{1}{\sqrt{2}}(E_x - iE_y)\hat{u}_{cw} + E_z\hat{u}_0 - \frac{1}{\sqrt{2}}(E_x + iE_y)\hat{u}_{ccw}$

Looking at the terms in parenthesis we see that if we add time dependence of $e^{i\omega t}$, these terms could represent fields of orthogonal polarization where the terms $(E_x - iE_y)e^{i\omega t}$ and $(E_x + iE_y)e^{i\omega t}$ would represent oppositely polarized light of circular polarization, whereas the term $E_z\, e^{i\omega t}$ would represent linearly polarized light in the z direction. This also gives a nice representation of the spherical basis vector $\vec{u}$ that $\vec{E}$ and $\vec{r}$ was expanded in, and can be represented by the diagram below.

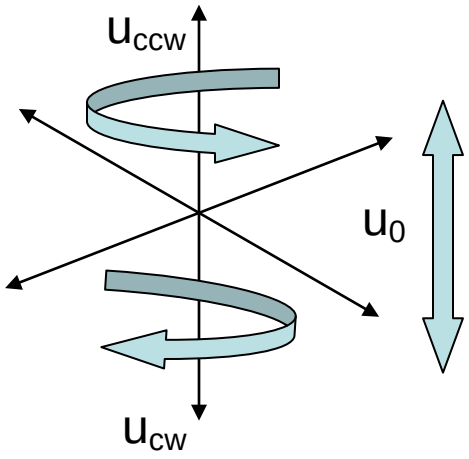

Figure 3.1: Unit vector representation in spherical basis

If we let $E_{\sigma^+} = (E_x - iE_y)e^{i\omega t}$ and $E_{\sigma^-} = (E_x + iE_y)e^{i\omega t}$ we can rewrite $\vec{E}$ as

(3.12) $\vec{E}(r) = (E_{\sigma^+}\hat{u}_{ccw} + E_{\pi}\hat{u}_0 + E_{\sigma^-}\hat{u}_{cw})$

Therefore we find that the transition matrix element can be written as

(3.13) $\left\langle F', m_f' \middle| \vec{r}\cdot\vec{E} \middle| F, m_f \right\rangle = \left\langle F', m_f' \middle| \sqrt{\frac{4\pi}{3}} r(E_{\sigma^+}Y_1^{+1} + E_{\pi}Y_1^0 + E_{\sigma^-}Y_1^{-1} \middle| F, m_f \right\rangle.$

This tells us that the rate of transition from $\left|F, m_f\right\rangle$ to $\left|F', m_f'\right\rangle$ for different polarizations of light is as follows:

(3.14a) *transition rate for* σ^+: $\left\langle F', m_f' \left| \sqrt{\frac{4\pi}{3}} r E_{\sigma^+} Y_1^{+1} \right| F, m_f \right\rangle$

(3.14b) *transition rate for* π: $\left\langle F', m_f' \left| \sqrt{\frac{4\pi}{3}} r E_0 Y_1^0 \right| F, m_f \right\rangle$

(3.14c) *transition rate for* σ^-: $\left\langle F', m_f' \left| \sqrt{\frac{4\pi}{3}} r E_{\sigma^-} Y_1^{-1} \right| F, m_f \right\rangle$

Our next goal is to find and compare matrix elements for a given $j \rightarrow j'$ transition. Note that we can write these transition rates, which we have in terms of the F and m_f states, in terms of the J, m_j, I, m_I representation by writing

(3.15) $\left| F, m_f \right\rangle = \sum_{m_j, m_i = m_f - m_j} \left\langle J, m_j, I, m_i \left| F, m_f \right. \right\rangle \left| J, m_j, I, m_i \right\rangle$.

Note that $\left\langle J, m_j, I, m_i \left| F, m_f \right. \right\rangle = C^{f,j,i}_{m_f, m_j, m_i}$ are the Clebsch Gordon coefficients relating the $\left| F, m_f \right\rangle$ state to a superposition of $\left| J, m_j, I, m_i \right\rangle$ states. We can now write similar transition rate matrix elements for a given polarization in terms of the J, m_j, I, m_I quantum numbers.

(3.16a)

transition rate for σ^+:

$$\left\langle F', m_f' \left| \sqrt{\frac{4\pi}{3}} r E_{\sigma^+} Y_1^{+1} \right| F, m_f \right\rangle = \sum_{m_j, m_i = m_f - m_j} \sum_{m_j', m_i' = m_f' - m_j'} C^{f,j,i}_{m_f, m_j, m_i} C^{f',j',i'}_{m_f', m_j', m_i'} \left\langle j', m_j', i', m_i' \left| r Y_1^1 \right| j, m_j, i, m_i \right\rangle$$

(3.16b)

transition rate for π:

$$\left\langle F', m_f' \left| \sqrt{\frac{4\pi}{3}} r E_0 Y_1^0 \right| F, m_f \right\rangle = \sum_{m_j, m_i = m_f - m_j} \sum_{m_j', m_i' = m_f' - m_j'} C^{f,j,i}_{m_f, m_j, m_i} C^{f',j',i'}_{m_f', m_j', m_i'} \left\langle j', m_j', i', m_i' \left| r Y_1^0 \right| j, m_j, i, m_i \right\rangle$$

(3.16c)

transition rate for σ^-:

$$\left\langle F', m_f' \left| \sqrt{\frac{4\pi}{3}} r E_{\sigma^-} Y_1^{-1} \right| F, m_f \right\rangle = \sum_{m_j, m_i = m_f - m_j} \sum_{m_j', m_i' = m_f' - m_j'} C^{f,j,i}_{m_f, m_j, m_i} C^{f',j',i'}_{m_f', m_j', m_i'} \left\langle j', m_j', i', m_i' \left| r Y_1^{-1} \right| j, m_j, i, m_i \right\rangle$$

The next step is to actually evaluate these matrix elements. In order to proceed we must use the Wignar-Eckart theorem which states that the matrix elements will separate into radial and angular components. To see this explicitly let us calculate the matrix element $\left\langle n', j', m_j' \left| r Y_1^q \right| n, j, m_j \right\rangle$ *for* $q = ccw, cw, 0$ in the following way. First note that

(3.17) $$\left| n, j, m_j \right\rangle = \sum_{m_l, m_s = m_j - m_l} C^{j,l,s}_{m_j, m_l, m_s} \left| s, m_s \right\rangle \otimes \left| n, l, m_l \right\rangle$$

can be rewritten as

(3.18) $$\left|n, j, m_j\right\rangle = \sum_{m_l, m_s = m_j - m_l} C^{j,l,s}_{m_j, m_l, m_s} \left|s, m_s\right\rangle \otimes R^l_n(r) Y^m_l(\theta, \phi)$$

in coordinate space where $R^l_n(r)$ are the radial Laguerre functions which depend on the n and l quantum numbers, and $Y^m_l(\theta, \phi)$ are the angular spherical harmonic functions which depend on the m and l quantum numbers. Now we can rewrite the matrix element we wish to evaluate as

(3.19)

$$\left\langle n', j', m_j' \right| r Y^q_1 \left| n, j, m_j \right\rangle = \sum_{m_l, m_s = m_j - m_l} \sum_{m_{l'}, m_{s'} = m_{j'} - m_{l'}} C^{j,l,s}_{m_j, m_l, m_s} C^{j',l',s'}_{m_j', m_l', m_s'} \left\langle s', m_s' \right| s, m_s \left\rangle \otimes \int R^{l'*}_{n'} r R^l_n r^2 dr \int Y^{m'*}_{l'} Y^q_1 Y^m_l d\Omega$$

We see that the integral depending on the radial component can be separated from the angular integral. This in turn may be finally be rewritten using equation (3.17) as

(3.20)

$$\begin{aligned} \left\langle n', j', m_j' \right| r Y^q_1 \left| n, j, m_j \right\rangle &= \sum_{m_l, m_s = m_j - m_l} \sum_{m_{l'}, m_{s'} = m_{j'} - m_{l'}} C^{j,l,s}_{m_j, m_l, m_s} C^{j',l',s'}_{m_j', m_l', m_s'} \left\langle s', m_s' \right| s, m_s \left\rangle \otimes \left\langle n', l' \right\| r \left\| n, l \right\rangle \left\langle l' m_l' \right| 1, q, l, m_l \right\rangle \\ &= \left\langle n', j' \right\| r \left\| n, j \right\rangle \left\langle j' m_j' \right| 1, q, j, m_j \left\rangle \end{aligned}$$

where the first matrix element is radially dependent and the second matrix element is angularly dependent. Therefore we see that the matrix elements we wish to calculate can be separated into angular and radial components.

Using this result we can now fully derive the matrix elements of the Hamiltonian $\left\langle F', m_f' \middle| rY_1^q \middle| F, m_f \right\rangle$. From equation (3.15) we found that

(3.21)

$$\left\langle F', m_f' \middle| rY_1^q \middle| F, m_f \right\rangle = \sum_{m_j, m_i = m_f - m_j} \sum_{m_j', m_i' = m_f' - m_j'} C^{f,j,i}_{m_f, m_j, m_i} C^{f',j',i'}_{m_f', m_j', m_i'} \left\langle j', m_j' \middle| \otimes \left\langle i', m_i' \middle| rY_1^q \middle| j, m_j \right\rangle \otimes \middle| i, m_i \right\rangle$$

This can be rewritten as

(3.22)

$$\left\langle F', m_f' \middle| rY_1^q \middle| F, m_f \right\rangle = \sum_{m_j, m_i = m_f - m_j} \sum_{m_j', m_i' = m_f' - m_j'} C^{f,j,i}_{m_f, m_j, m_i} C^{f',j',i'}_{m_f', m_j', m_i'} \left\langle j', m_j' \middle| rY_1^q \middle| j, m_j \right\rangle \otimes \underbrace{\left\langle i', m_i' \middle| i, m_i \right\rangle}_{\delta_{i,i'} \delta_{m_i', m_i}}$$

Note that you get a delta function when combining the bra and ket of the nuclear spinors since they are not coupled by the coordinate operator. Next we use equation (3.20) and find

(3.23)

$$\left\langle F', m_f' \middle| rY_1^q \middle| F, m_f \right\rangle = \sum_{m_j, m_i = m_f - m_j} \sum_{m_j'} C^{f,j,i}_{m_f, m_j, m_i} C^{f',j',i}_{m_f', m_j', m_i} \left\langle j', m_j' \middle| 1, q, j, m_j \right\rangle \left\langle n', j' \middle\| r \middle\| n, j \right\rangle .$$

This may finally be rewritten as

(3.24) $$\left\langle F', m_f' \middle| rY_1^q \middle| F, m_f \right\rangle = \left\langle n', j' \middle\| r \middle\| n, j \right\rangle \sum_{m_j, m_i = m_f - m_j} \sum_{m_j'} C^{f,j,i}_{m_f, m_j, m_i} C^{f',j',i'}_{m_f', m_j', m_i'} C^{j',1,j}_{m_j', m_j, m_q}$$

which is just the radial function multiplied by the sum over a product of three Clebsch-Gordon coefficients. Since the radial term which is multiplied by the product of coefficients is depends only on n, n', j, and j' you may calculate the relative transition rates for all $j \to j'$ transitions without needing to know the actual value of the radial function.

The general mathematical idea is illustrated below

$$\underbrace{\underbrace{Y_1^q}_{\text{Angular component of Dipole operator}} \underbrace{|l, m_l\rangle}_{\text{initial state}}}_{\text{acts on state}} = \underbrace{|1, q, l, m_l\rangle}_{\text{new state is vector sum of two angular momenta}} = \underbrace{\sum \underbrace{\langle l', m_l' | Y_1^q | l, m_l \rangle}_{\text{Clebsch Gordan coefficient coupling new state to final state}} \underbrace{|l', m_l'\rangle}_{\text{Angular momentum associated with final atomic state}}}_{\text{Linear superpostion of final atomic states}}$$

Basically the angular component of the dipole operator, which depends on the helicity of the photon, acts on an initial atomic state. This forms a new state where the angular momentum of both the photon and initial atomic state are combined. This in turn may be rewritten as a superposition of final atomic states that the atom may transition to, weighted by their respective Clebsch-Gordon coefficients.

Below I have qualitatively shown such a transition from the $l = 0$ state to an $l = 1$ state ($s \to p$ transition).

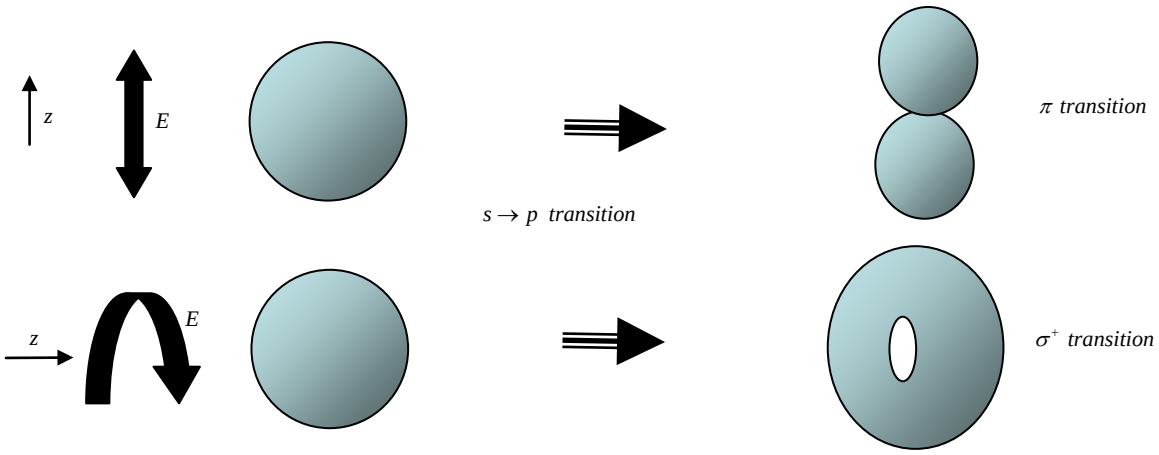

Figure 3.2: Example of dipole transitions

For the first case the spherically symmetric s-state atom combines with a linearly polarized π-photon and will produce the dumbbell shape. In the second case, the atom absorbs the circularly polarized σ^+-photon and transitions to a doughnut shaped state. More complicated transitions are shown below starting from the p-state $|l=1, m_l=1\rangle$. The depicted size of each of the final states represents their associated Clebsch-Gordon coefficient.

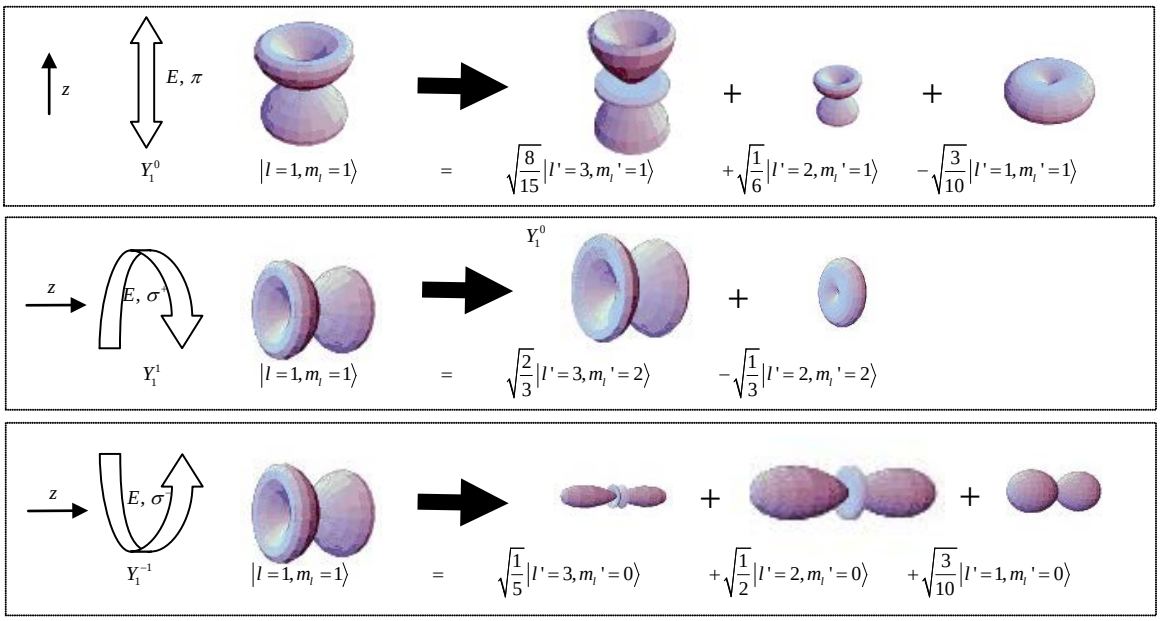

Figure3.3: Examples of dipole transitions for different helicities of light. The relative size of the spherical harmonic represents the value of the Clebsch-Gordon Coefficient.

Next we will find, in general, which transitions are allowed, i.e. the selection rules. First note that $\vec{r}$ does not couple to spin states, therefore $\Delta s,\ \Delta i,\ \Delta m_s,\ \Delta m_i = 0$. Next, solving the angular integral to find Δm_l

(3.25) $$\langle l', m_l' | 1, q, l, m_l \rangle = \int Y_{l'}^{m'*} Y_1^q Y_l^m d\Omega = \int_0^{2\pi} F(\theta) d\theta \int_0^{\pi} e^{-im_l'\phi} e^{iq\phi} e^{im_l\phi} d\phi = \delta_{m_l+q,m_l'}$$

so we get the following conditions:

for σ^+ transitions $\Delta m_l = m_l' - m_l = +1$

for σ^- transitions $\Delta m_l = m_l' - m_l = -1$

for π transitions $\Delta m_l = m_l' - m_l = 0$

Next, we note that since $m_j = m_l + m_s$ and because $\Delta m_s = 0$ we find

$\Delta m_j = m_j' - m_j = 0, \pm 1$.

Also, since $m_f = m_j + m_i$, and because $\Delta m_s = 0$ we also find that

$\Delta m_f = m_f' - m_f = 0, \pm 1$.

Finally we note that since a photon imparts angular momentum of $l = 1$, the orbital angular momentum selection rule should be $\Delta l = l' - l = \pm 1$. Note that $\Delta l \neq 0$ since the parity of the spherical harmonics goes like $(-1)^l$. Lastly from the condition on Δl, $\Delta j = j' - j = \pm 1, 0$ and $\Delta f = f' - f = \pm 1, 0$. Note that even though $\Delta l \neq 0$, $\Delta j = 0$ $\Delta f = 0$ are allowed. This is because L couples to S and therefore you can have states where $\Delta j = 0$ or $\Delta f = 0$ even though $\Delta l \neq 0$ such as the transition $\left| j = \frac{3}{2}, l = 1 \right\rangle \rightarrow \left| j = \frac{3}{2}, l = 2 \right\rangle$.

In summary the selection rules may be written as

(3.26a) $\Delta s,\ \Delta i,\ \Delta m_s,\ \Delta m_i = 0$

(3.26b) $\Delta m_l,\ \Delta m_j, \Delta m_f = \pm 1, 0$

(3.26c) $\Delta l = \pm 1$

(3.26d) $\Delta f, \Delta j = \pm 1, 0$.

Using the procedure of calculating the dipole matrix elements, all allowed transition rates may be calculated. In the appendix I have included a program in MAPLE which calculates all matrix elements. Also included is a diagram which illustrates all the relative transition strengths for each of the hyperfine transitions in Rubidium for the D_1 and D_2 transitions.

Optical Forces

4.1) Radiation Pressure

This section will discuss the kinds of force that a light field can impart on an atom. These forces can be used to slow and trap atoms, reducing the energy of the atoms to tens of microKelvin [27,28]. Optical scattering forces were first observed by Askin in 1970 [29]. These methods were then proven useful for atom cooling and trapping by Chu and others [30,31]. We will discuss the basics of optical forces, and will then discuss trapping techniques in detail.

In order to find the force on an atom imparted by a light field, we use the quantum mechanical force operator **F** defined as

(4.1) $\langle F \rangle = \frac{d}{dt}\langle p \rangle$.

The time evolution of a time independent expectation value can be written as:

(4.2) $$\frac{d}{dt}\langle A\rangle = \frac{i}{\hbar}\langle [H, A]\rangle$$

and the commutator of H and p is

(4.3) $$[H, p] = i\hbar\frac{\partial H}{\partial z}$$

so we find that

(4.4) $$F = -\left\langle \frac{\partial H}{\partial z}\right\rangle .$$

For atoms experiencing a force due to dipole interaction this may be written as

(4.5) $$\langle F\rangle = e\left\langle \frac{\partial}{\partial z}(\vec{E}\cdot\vec{r})\right\rangle$$

By using the dipole approximation, we may neglect the spatial variation of the field over the length of the atom and rewrite the force as

(4.6) $$\langle F\rangle = e\frac{\partial}{\partial z}\langle (\vec{E}\cdot\vec{r})\rangle$$

Using $\langle A \rangle = Tr(\rho A)$ we find that

(4.7) $$\langle F \rangle = \hbar \left(\frac{\partial \Omega}{\partial z} \tilde{\rho}_{21}{}^{*} + \frac{\partial \Omega^{*}}{\partial z} \tilde{\rho}_{21} \right)$$

where again, $\tilde{\rho}_{21}$ is the time independent matrix element $\tilde{\rho}_{21} = \rho_{21} e^{i\omega t}$.

If we split $\frac{\partial \Omega}{\partial z}$ into its real and imaginary parts, we can write it as:

(4.8) $$\frac{\partial \Omega}{\partial z} = (q_r + i q_i)\Omega .$$

Note for a traveling wave field, if E is of the form $E_0 e^{i(kz-\omega t)}$, q_i is nonzero while $q_r = 0$, while for traveling waves of the form $E(z)e^{i\omega t}$, q_r is nonzero while $q_i = 0$. Inserting this into the expression for the force we find:

(4.9) $$\langle F \rangle = \hbar q_r \left(\Omega \tilde{\rho}_{21}{}^{*} + \Omega^{*} \tilde{\rho}_{21} \right) + i\hbar q_i \left(\Omega \tilde{\rho}_{21}{}^{*} - \Omega^{*} \tilde{\rho}_{21} \right).$$

For a traveling wave of the form

(4.10) $$E(z) = \frac{E_0}{2} \left(e^{i(kz-\omega t)} + c.c. \right)$$

the gradient of the Rabi frequency is proportional to the surviving negative frequency component of the field after making the RWA. In this case $q_i = k$, and the force is equal to

(4.11) $\langle F \rangle = i\hbar k\left(\Omega\tilde{\rho}_{21}{}^{*} - \Omega^{*}\tilde{\rho}_{21}\right)$

and from the solutions to the steady state Bloch equations, specifically eq (1.46), we find,

(4.12) $\langle F \rangle = \hbar k\Gamma\tilde{\rho}_{22}$

This force is associated with absorption followed by spontaneous emission as will be discussed below, and is referred to as the radiation pressure force. This force differs from that of a traveling wave having a field amplitude gradient rather than a phase gradient. These forces depend on the amplitude of the field and are associated with light shifts resulting from stimulated emission. For a standing wave of the form

(4.13) $E(z) = E_0\cos(kz)\left(e^{-i\omega t} + c.c.\right)$

the corresponding force can be found

(4.14) $$F = \frac{2\hbar k \delta s_0 \sin 2kz}{1 + 4s_0 \cos^2 kz + (2\delta/\Gamma)^2}$$

Let us now describe the radiation pressure force physically. Radiation pressure is the force which transfers momentum from a photon to an atom, and can be understood from the diagram below.

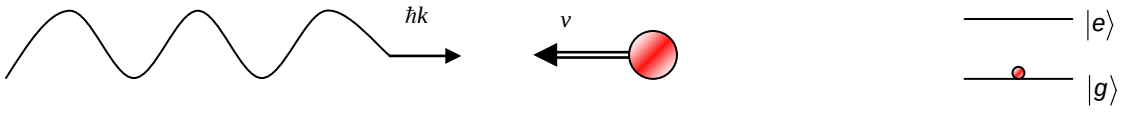

atom starts in ground state $|g\rangle$, photon has momentum ħk

atom absorbs photon, decreases in velocity by $\frac{\hbar k}{m}$, and is excited to $|e\rangle$

atom spontaneously decays, falls back to ground state $|g\rangle$

Figure 4.1: Figure illustrating the basics of radiation pressure force

A photon with momentum $p = \hbar k$ is absorbed by an atom in the ground state $|g\rangle$, traveling with velocity v. Upon absorption the atom transitions to the excited

state $|e\rangle$ and its velocity is decreased to $v-\frac{\hbar k}{m}$. Since spontaneously emitted photons are emitted in a random direction, for a group of atoms which spontaneously decay, the average momentum transfer due to the photon recoil is zero. These atoms end in the ground state with a velocity $v-\frac{\hbar k}{m}$. Note that the momentum transferred from photon recoil for atoms undergoing stimulated decay is always in the opposite direction of the force since the emitted photon is along the same direction as the absorbed photon. The net force in this case is zero.

We deduce that the radiation force should be proportional to the rate of spontaneous decay multiplied by the momentum of the photon:

(4.15) $$F=\frac{\partial p}{\partial t}=\hbar k\Gamma\rho_{22}=\hbar k\Gamma\frac{\Omega^2}{2\Omega^2+\Gamma^2+4\delta^2}$$

Where Ω is the Rabi frequency, Γ is the rate of spontaneous decay, and δ is the detuning from atomic resonance. This is the same result we derived earlier in eq. (4.12). Further more if we use the fact that the ratio $\frac{\Omega^2}{\Gamma^2}=\frac{I}{I_{sat}}$, where I is the intensity of the field and I_{sat} is the saturation intensity, and the substitution for the detuning that a moving atom experiences as $\delta=\delta_{rest}-\vec{k}\cdot\vec{v}$ we find:

$$(4.16)\quad F = \hbar k \Gamma \frac{I/I_{sat}}{2\,I/I_{sat} + 1 + \left(\frac{2(\delta_{rest} - \vec{k}\cdot\vec{v})}{\Gamma}\right)^2}$$

where δ_{rest} is the laser's detuning from resonance in the laboratory frame.

The most efficient cooling occurs for atoms with velocities such that $\left|2(\delta_{rest} - \vec{k}\cdot\vec{v})\right| \le \Gamma\sqrt{1+\frac{I}{I_{sat}}}$. Atoms not within this velocity range, however, experience little to no slowing, and even atoms that are within this range are quickly decelerated out of this range.

One solution to improve the efficiency of slowing is to sweep the laser frequency at a constant rate proportional to the rate at which the atom is slowing. Then as the atom is slowed, it stays at resonance condition with the chirped beam. If V(t) is the central velocity of an atomic beam, then let the laser sweep such that $\delta_{rest} = \delta' - kV(t)$. For this condition, the detuning from resonance seen in the atom's frame will always be δ'. We find:

$$(4.17)\quad F = \hbar k \frac{\Gamma}{2} \frac{I/I_{sat}}{I/I_{sat} + 1 + \left(\frac{2\delta'}{\Gamma}\right)^2} = Ma$$

and we find that the rate at which we should scan the chirp laser should be:

$$(4.18)\quad \dot{\delta}_{rest} = -ka = -\hbar k \frac{\Gamma}{2M} \frac{I/I_{sat}}{I/I_{sat} + 1 + \left(\frac{2\delta'}{\Gamma}\right)^2}$$

We will discuss chirp cooling further when discussing the details of the magneto optical trap.

PUMP-PROBE THEORY

In the following section I will discuss several different types of systems which consist of two beams (a pump and a probe), and either two or three atomic levels. Within pump-probe systems, the pump beam is used to affect the interaction of the probe with an atomic medium. We will investigate how to use a pump to induce probe transparency within the medium, and discuss the switching applications of these systems.

The systems we will consider are the following. First we will look at a two level co- and counter-propagating pump-probe system with the pump and probe having the same polarization. Next we will investigate three level counter-propagting pump-probe systems, also of the same polarization, and see how these systems lead to V-type EIT. We will then see how linearly cross polarized co- and counter-propagating pump and probe behave in a two level atom. Lastly we will explore how the cross polarized co- and counter-propagating pump and probe behave in a three level atom.

5.) Co-propagating Saturated Absorption

One method for inducing transparency in a system is by saturation. The simplest example of this is that of an overlapped co-propagating pump and probe traveling through an atomic vapor. Consider this for a two level system in the following way. First note that if a resonant weak probe ($\Omega_{probe} << \Gamma$) is sent through a collection of two level atoms, the output probe intensity would decrease as photons from the field are absorbed and fluoresced in random directions.

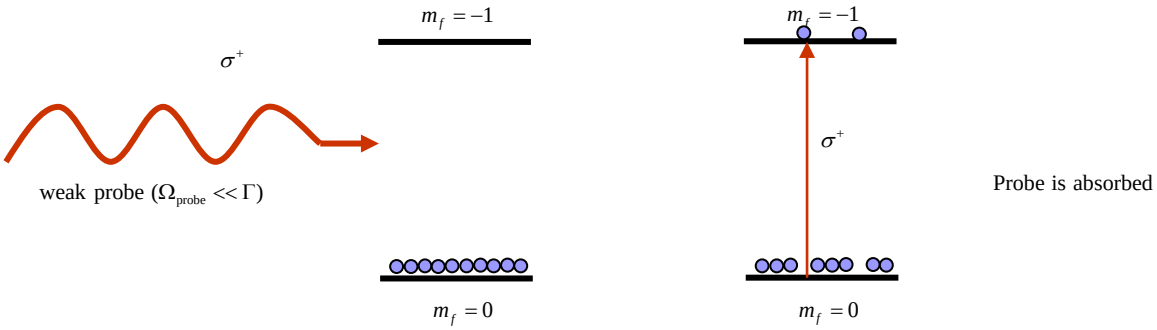

Figure 5.1: Absorption of a probe in a two level system

Next, assume a resonant strong pump is overlapped and co-propagating with the weak probe and sent through the system. If the pump is sufficiently strong ($\Omega_{pump} >> \Gamma$), the system will become saturated, having equal number of atoms in the ground state and excited state. At this point, atoms in the system can no longer absorb photons, and the medium will be transparent to the weak probe.

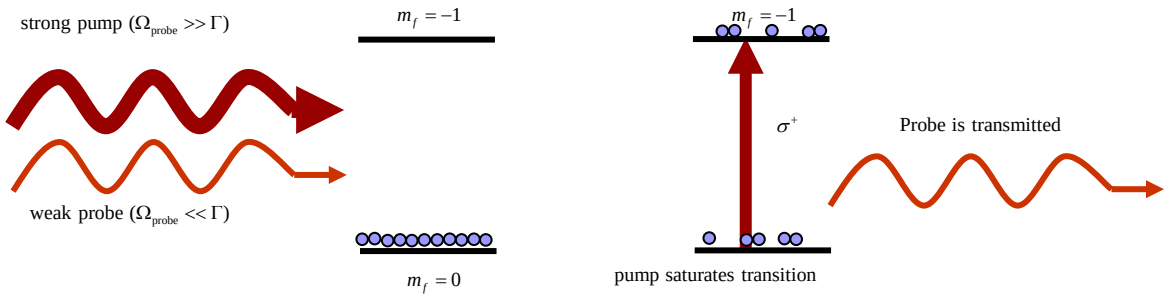

Figure 5 .2: Saturation induced transparency of probe in two level system

6.) Counter-propagating Saturated Absorption

Doppler free spectroscopy, otherwise known as counter-propagating saturated absorption, allows one to resolve hyperfine levels in a Doppler broadened atomic medium[32]. In an atomic vapor atoms have a velocity spread corresponding to the Boltzmann energy distribution. If a scanning beam is sent an atomic vapor to probe atomic resonance, a broad resonance profile on the order of a GHz would be measured even though the actual linewidth of Rubidium is on the order of MHz. The profile measured can be thought of as a convolution or a weighted averaged of the Doppler free absorption profile with the Boltzman distribution as shown in the diagram below.

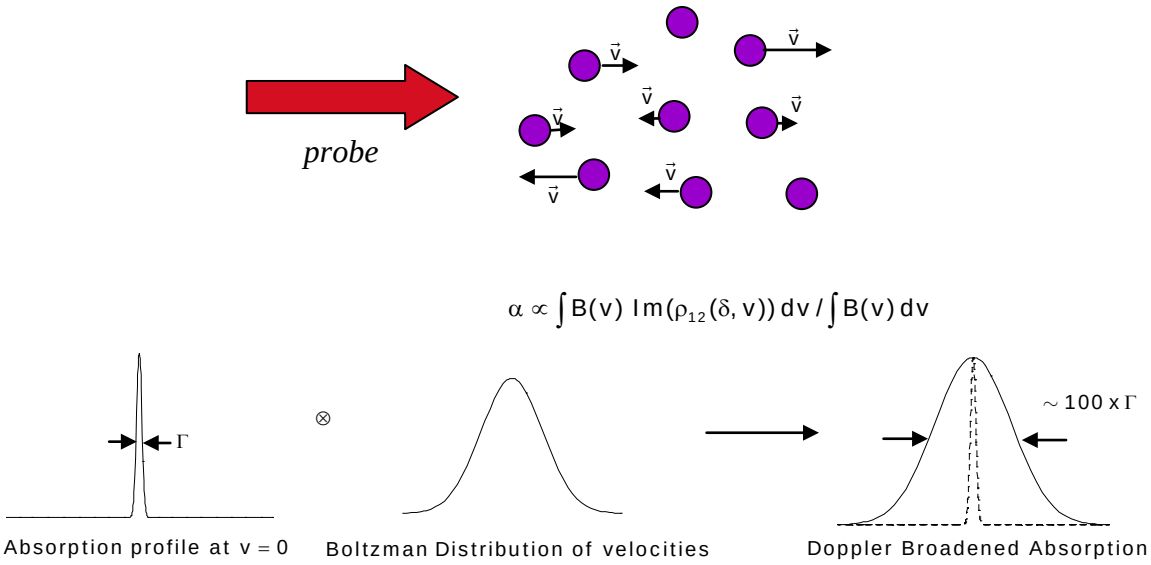

Figure 6.1: Illustration of Doppler Broadening of Linear Absorption

This linear absorption profile is shown below for the F=3, D2 transitions in Rb85.

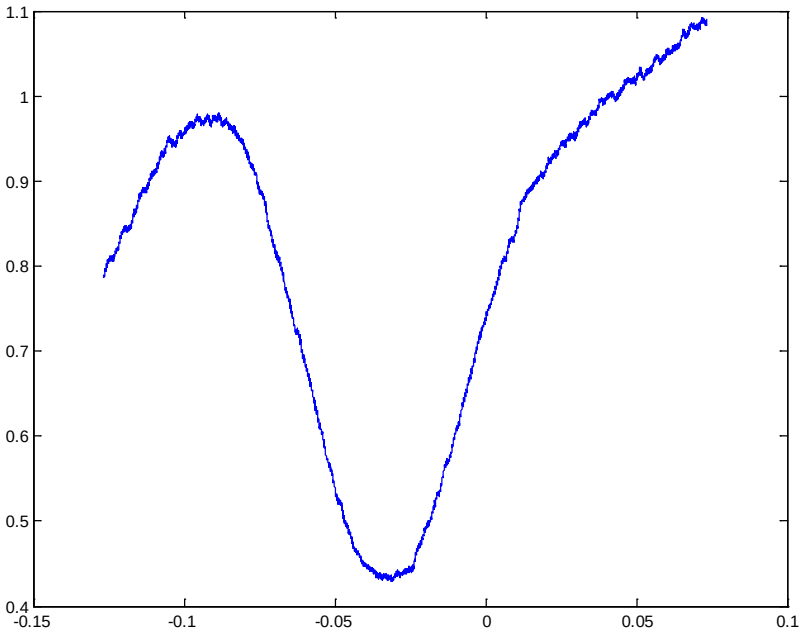

Figure 6.2: Intensity vs frequency trace of Doppler Broadened linear absorption for Rb 85, $5S_{1/2}F = 3$ *transtions*

In order to resolve the hyper fine energy levels, we can send a counter-propagating pump of the same frequency, derived from the same laser, through the atomic vapor. Note that with a counter-propagating pump and probe, the zero velocity atoms are the only velocity group which will see the probe and pump at the same frequency. For example, if, as the probe frequency is scanned, a velocity group other than the zero velocity group experiences a resonant probe, the pump will either be red or blue shifted from resonance depending on the direction of motion. If the pump is strong enough to saturate the atomic transition at resonance condition, these zero velocity atoms will be transparent to the probe field, even though other atoms within the Doppler profile will still absorb the probe, as it is scanned through their Doppler-shifted resonances.

We note that for a co-propagating pump and probe as discussed above, all velocity groups see the two fields at the same frequency. Therefore the behavior is identical to that of the counter-propagating saturated absorption at the zero velocity group.

The result for counter-propagating beams in a multilevel system is shown below for the F=3, D2 transition in Rb85, having three hyperfine transitions, and three cross-over peaks, which will be discussed below.

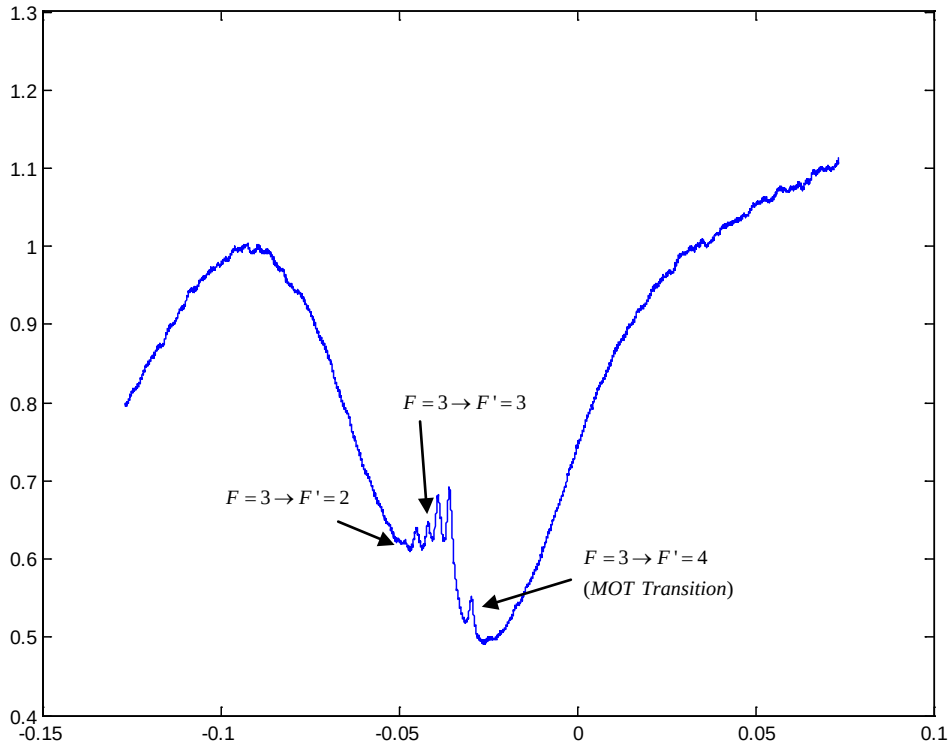

Figure 6.3: Intensity vs frequency trace of saturated absorption in Rb85, $5S_{1/2}F=3$ *showing zero velocity peaks and V-type EIT cross over peaks (see below for details)*

7.) Three Level Counter-Propagating Pump-Probe System of the same Polarization (V-type EIT)

Note that even though there are only three hyperfine transitions, six peaks are present. These extra peaks are known as cross-over peaks. This induced transparency is caused by a different mechanism than saturation discussed above. When the laser is scanned to a frequency half way between two resonant

frequencies, the velocity group at $\frac{\Delta\omega}{2k}$ experiences a probe Doppler shifted towards resonance for one transition and the pump oppositely Doppler shifted towards resonance for the other transition. This is shown in the diagram below for a cross-over peak located half way between $F=3\rightarrow F'=2$ and $F=3\rightarrow F'=3$.

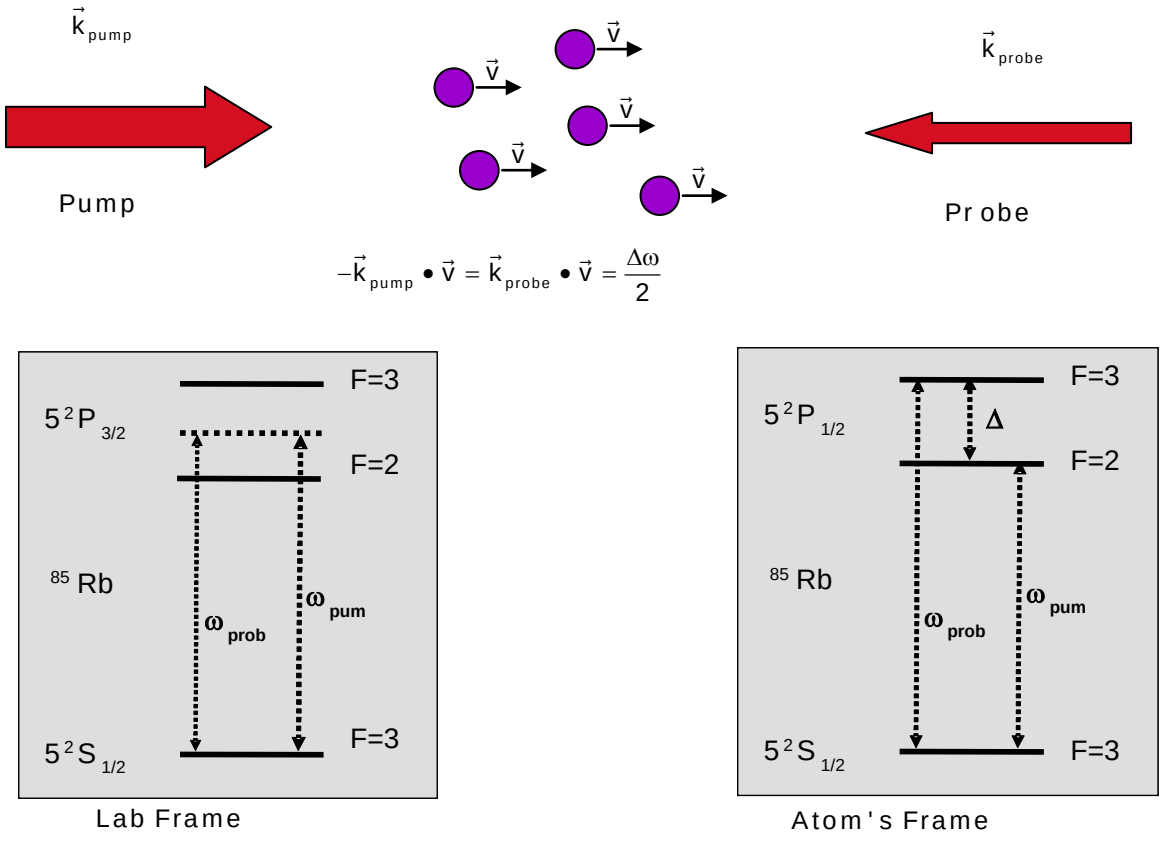

Figure 7.1: This figure describes the idea behind cross over peaks

We see that when the frequency is, in the lab frame, half way between the two atomic transitions, the velocity group located at $v=\pm\frac{\Delta\omega}{2k}$ experiences the pump

and probe beams as resonant on two different transitions. In the frame of the atom, this can be viewed as a three level V-type EIT system [33].

The stronger pump field imparts a light shift on the ground state, causing the system to be transparent to the probe. This behavior can be understood in the frame of the atom by noting that when a strong field is applied to the effective pump leg, the atom-field interaction energy shifts the ground state eigen-energy to that of the dressed state. This results in the beam which was once resonant for the probe leg becoming off resonant by an amount equal to the light shift. If the value of the light shift is larger than Γ, the probe will be transmitted. We find that when a strong pump is applied, a cross-over peak is always present in the saturated absorption profile between two resonance peaks. This light shift induced transparency may be found in any multi-level atom.

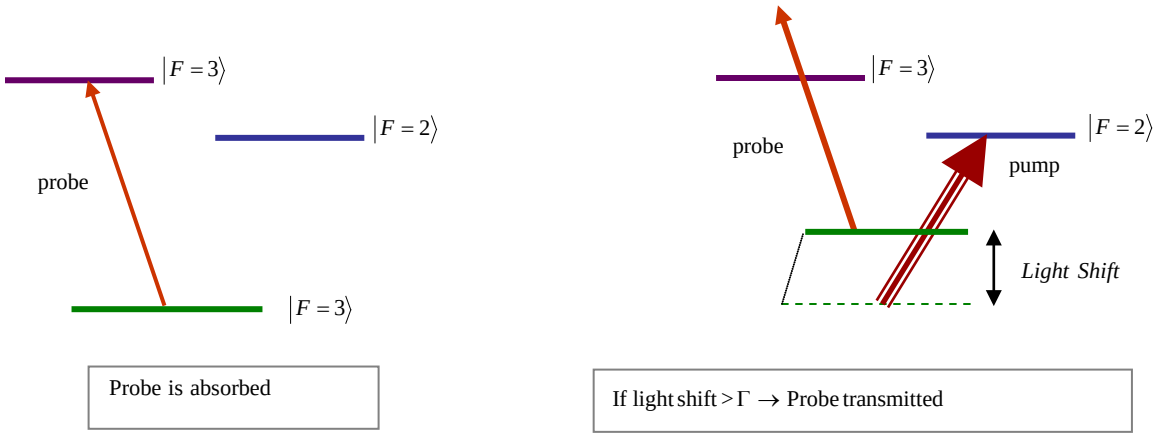

Figure 7.2: Illustration of how light shifts can induce probe transparency

8.) Two Level Linearly Crossed Polarized Co- and Counter-Propagating Pump-Probe System

For both counter-propagating and co-propagating saturated absorption, it may be useful to isolate the probe at the output. Let us first consider the co-propagating case, for sake of simplicity. One simple way to achieve probe isolation is to make the beams cross polarized and use polarization selective optics. We have seen that for matched polarizations, we can model both counter- and co-propagating saturated absorption as processes in a two-level system. We find, however, that linearly cross polarized saturated absorption will not occur effectively in a pure two level system for the following reason. First note that for a pure two level system such as the $m = 0 \rightarrow m = +1$ transition below, we know from selection rules, that transitions will only occur for light of σ^+ helicity.

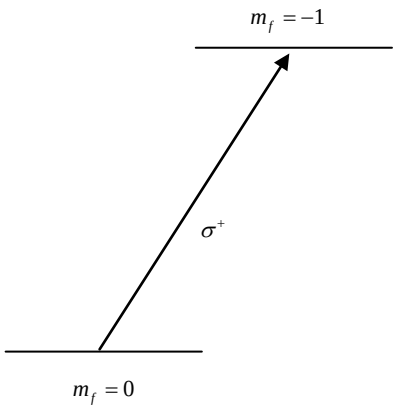

Figure 8.1: Two level system coupled by σ^+ helicity light

Next note that for two linearly crossed-polarized beams which are separated by a PBS, and which then travel different paths before being recombined and sent into

a Rb cell (for instance so that one can be pulsed independently of the other) the field may be written as $E = E_{\perp} + e^{i\phi} E_{\parallel}$ where $\phi = k\Delta L$.

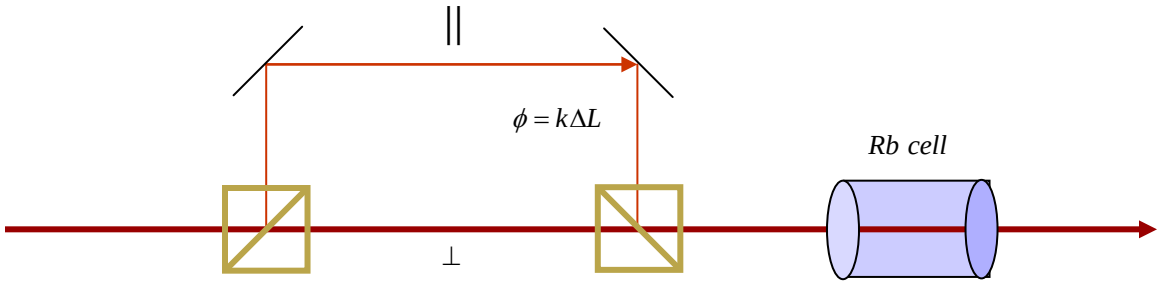

Figure 8.2: Illustration of combining linearly cross polarized light of different phase

Writing the linearly polarized fields as superpositions of circular polarizations, we rewrite the total field as $\vec{E} = \frac{1}{2}(E_{\sigma^+}\hat{\sigma}^+ + E_{\sigma^-}\hat{\sigma}^-) + e^{i\phi}\frac{1}{2}(E_{\sigma^+}\hat{\sigma}^+ - E_{\sigma^-}\hat{\sigma}^-)$.

Depending on the difference in phase between the two beams, various amounts of σ^+ and σ^- light may be present, affecting the rate of transition in the pure two level system. For example if $\phi = 0$, then $E = E_{\sigma^+}$ and the field would be absorbed by the two level system. If, however, $\phi = \pi$, then $E = E_{\sigma^-}$ and the field would be transparent to the two level system. In general the field can be described as $\vec{E} = \alpha E_{\sigma^+}\hat{\sigma}^+ + \beta E_{\sigma^-}\hat{\sigma}^-$ α, β complex. We find that in a two level system, this dependence on phase can lead to ineffective saturation-based induced transparency.

9.) Three Level Linearly Crossed Polarized Co- and Counter-Propagating Pump-Probe System

If we consider the interaction of the linearly cross polarized light with a multilevel system, however, we find that another mechanism for inducing transparency is present. We find that in a multilevel atom the behavior of the density matrix elements is not affected by the relative phases of the fields. This may be seen in the following way. For the three level V-type system below, the $m = 0 \rightarrow m = +1$ transition interacts with σ^+ light, whereas the $m = 0 \rightarrow m = -1$ transition interacts with σ^- light.

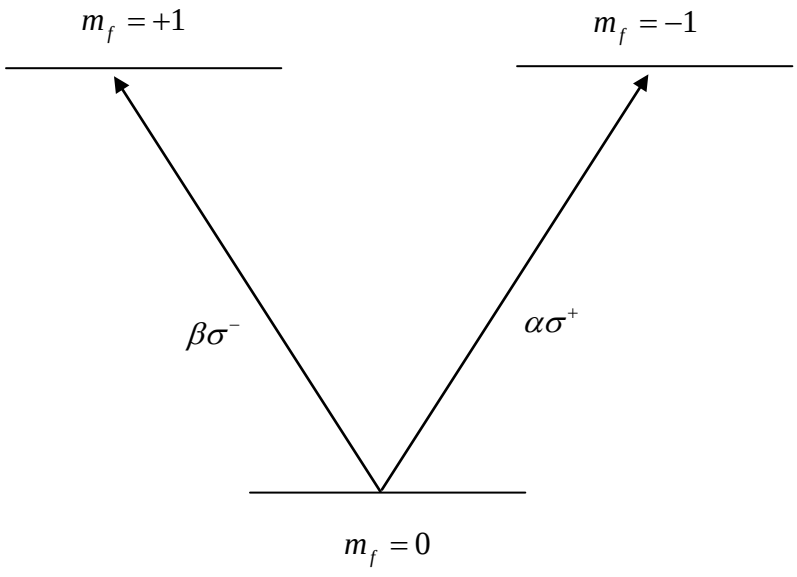

Figure 9.1: Three level system coupled by σ^+ and σ^- light

If we make a transformation to another 3 level basis for which

$|+\rangle = \frac{1}{2}\left(|m_f = +1\rangle + |m_f = -1\rangle\right)$ and $|-\rangle = \frac{e^{i\phi}}{2}\left(|m_f = +1\rangle - |m_f = -1\rangle\right)$, we get the three level system shown below, where now, the states are coupled by linearly polarized light. This is comparable to the V-type EIT situation discussed above, however, in this case the excited states are degenerate in energy.

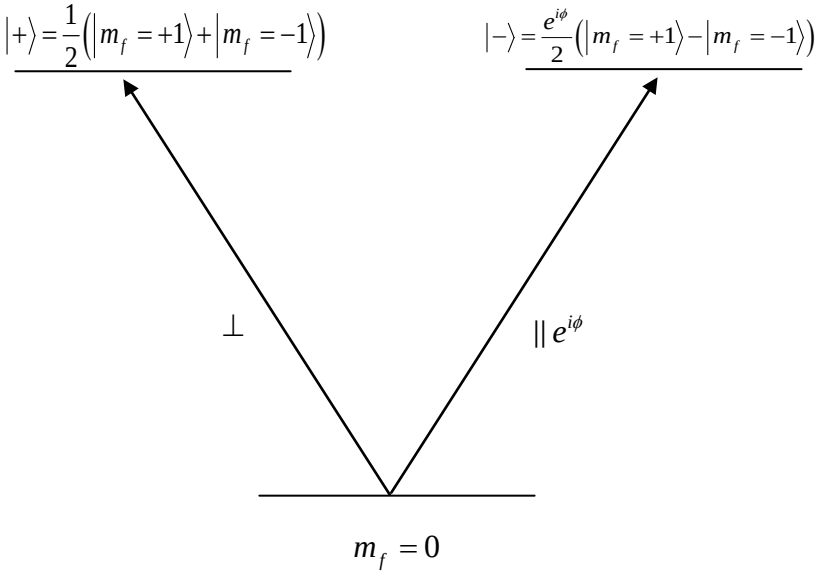

Figure 9.2: Three level system coupled by $\|$ and $\perp$ light

Note that this system is not affected by the relative phase differences between the two beams. If a weak $\perp$- polarized probe is present in this multilevel scheme, it will be absorbed by the $|+\rangle$ state. If a $\|$- polarized pump is also present, regardless of the relative phase between the two, it will induce a light shift on the ground state, as shown below. Similar to the V-type EIT case discussed above, this will cause the medium to be transparent to the probe.

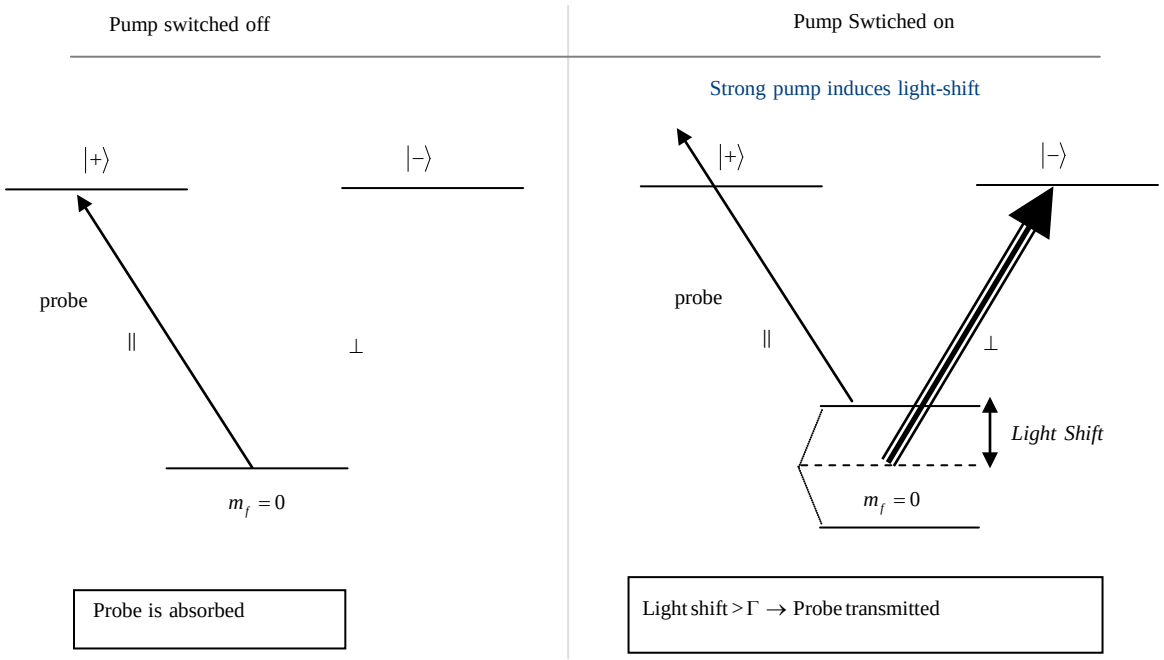

Figure 9.3: This illustration shows probe absorption when the pump field is off, and light shift induced probe transition when the pump field is switched on

Since this process is unaffected by phase differences in the pump and probe it can be the dominant cause for induced probe transparency regardless of such factors such as mirror vibrations, and variations in optical path differences between the two beams.

Note that this is identical to the behavior we would observe for zero velocity group atoms in a counter-propagating saturated absorption experiment where the beams were cross-polarized.

Counter-propagating saturated absorption experiments also have cross-over peaks, as discussed above for the case of matching polarization. For the

velocity group which experiences a cross-polarized pump and probe as resonant for two different non-degenerate levels, we can use a three level model similar to the cross-polarized model above. The energy diagram for this is shown below.

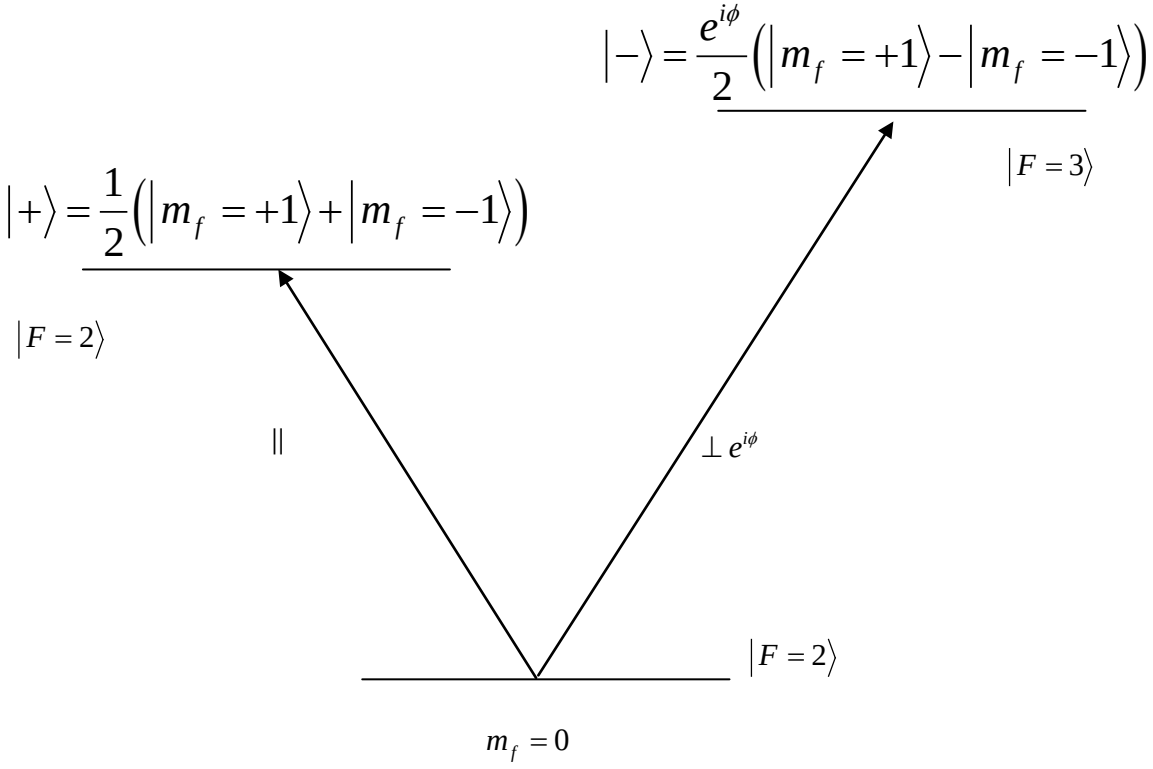

Figure 9.4: Illustration of three level system corresponding to linearly cross polarized V-type system

Again the ground state can be light-shifted by the stronger pump beam, creating the transparency for the weaker probe beam.

Optical Switching

We have seen in the previous sections that different methods can be employed to induce probe transparency. The transparency for the methods described were all based on either saturation, or light shifts. In all of the examples where the probe transparency was induced by a stronger pump, the operation of switching the probe may be implemented by switching the pump. The switching speed and minimum power necessary for switching, however, depend on the details of the system used [34, 35].

For the pump-probe systems discussed, we find that in order to increase switching speeds for the all-optical switch, we would like to use an atomic medium with a large absorptive linewidth. Temporally short probe pulses must contain many Fourier components when expressed in the frequency domain. For an atomic medium with a narrow frequency linewidth, only the frequency components of the pulse contained within the linewidth of the medium may be absorbed. Frequency components outside this range would not be absorbed and most of the pulse would be transmitted. If the atomic medium has a broad linewidth, however, a short probe pulse composed of the frequency components contained within the linewidth of the medium can be mostly absorbed. This is the first step of producing a fast switch. If a Doppler broadened atomic medium is used, the absorption bandwidth can be on the order of a GHz.

The next step in creating a broad-band switch is to produce a method of inducing probe transparency over the entire absorption linewidth. If complete transparency is achieved, the probe pulse may be completely transmitted. As discussed earlier, this transparency may either be based on saturation or light shifts.

10.) Saturation induced transparency

The first method of inducing transparency over the entire Doppler profile is by saturation. We have seen that one method of achieving this was sending in counter-propagating pump and probe beams through an atomic vapor. We have seen that if $\Omega_{pump} > \Gamma$, the medium is transparent to the probe over the hyperfine linewidth of about 10 MHz. As Ω_{pump} is increased power broadening effects begin to cause transparency over a linewidth larger than the natural atomic linewidth. As the pump power is further increased, the pump will begin to saturate transitions over the entire Doppler linewidth.

To find the power of the pump necessary to saturate the entire Doppler profile, we use equation (1.22) for ρ_{22}. Note that to saturate the natural linewidth we set $\delta \approx 0$, and setting $\rho_{22} = \frac{1}{2}$, we find $\Omega = \Gamma$. If we are interested in saturating the Doppler linewidth, however, the detuning from resonance of the pump would be much larger than the natural linewidth. For the condition $\delta >> \Gamma$ we set $\rho_{22} = \frac{1}{2 + \frac{\Gamma^2}{\Omega^2} + 4\frac{\delta^2}{\Omega^2}} = \frac{1}{2}$ and we find $\Omega >> \delta$. The power to saturate the entire Doppler profile written in terms of the power to saturate the natural line width can be expressed as $P_{Doppler} > \frac{\delta^2}{\Gamma^2} P_{natural\ linewidth}$. Since the linewidth of the

Doppler profile is about 100 times larger that the natural linewidth, we find that $P_{Doppler} > 10^4 P_{natural\,linewidth}$.

Below are plots from simulations of saturated absorption for different values of pump intensity. We see that as the pump power is increased, power broadening occurs so that off resonant transitions can broaden the saturated absorption linewidth. As the pump power is increased, power broadening becomes so significant that the entire Doppler profile is saturated by the pump.

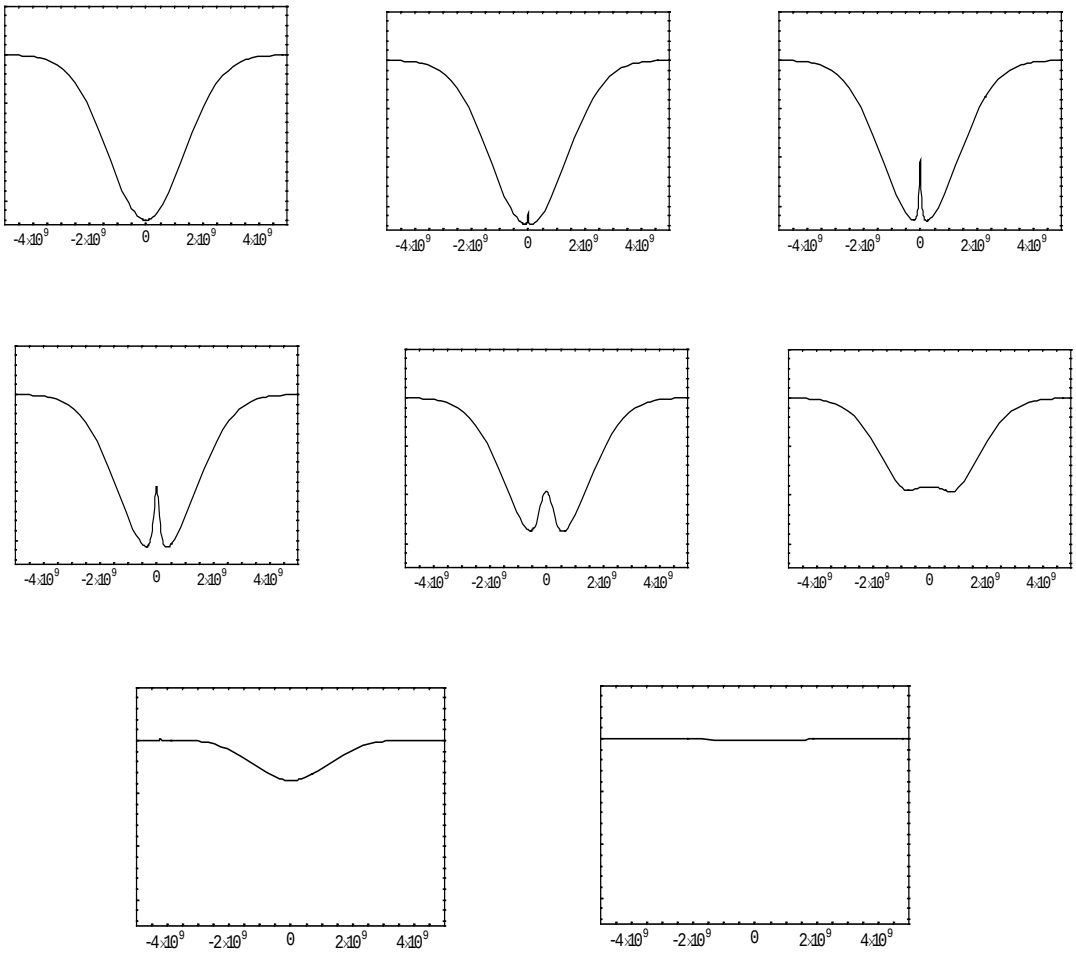

Figure 10.1: Plots showing the effect of power broadening in saturated absorption

In the figures above, saturated absorption is modeled in the following way. We first write the full Hamiltonian for a pump/probe two-level system as

(10.1)

$$\tilde{H} = \begin{bmatrix} \hbar\omega_1 & \frac{1}{2}(\Omega_{pump} Exp[i\omega_{pump} t] + \Omega_{probe} Exp[i\omega_{probe} t]) \\ \frac{1}{2}(\Omega_{pump} Exp[-i\omega_{pump} t] + \Omega_{probe} Exp[-i\omega_{probe} t]) & \hbar\omega_2 \end{bmatrix}$$

Making a rotating wave transformation similar to that of the time dependent two level system in section 1, we use the transformation matrix

(10.2) $$Q = \begin{bmatrix} Exp[i\omega_1 t] & 0 \\ 0 & Exp[i(\omega_2 + \delta)t \end{bmatrix}$$

And find the Hamiltonian evolving with the pump field to be

(10.3) $$\tilde{\tilde{H}} = \begin{bmatrix} 0 & \frac{1}{2}(\Omega_{pump} + \Omega_{probe} Exp[-i\Delta t]) \\ \frac{1}{2}(\Omega_{pump} + \Omega_{probe} Exp[-i\Delta t]) & -\delta \end{bmatrix}$$

where $\Delta = \omega_{pump} - \omega_{probe}$ and $\delta = \omega_{pump} - (\omega_2 - \omega_1)$. We then set up the time dependent density matrix equations, expanding the elements in terms of Fourier

components $Exp[-im\Delta t]$, where Δ is the difference detuning between the pump and probe and m is an integer. Keeping only up to the first order expansion in m (m=-1, 0, 1), we solve for the steady state coefficients of these Fourier components by matching terms in m. Setting Δ to the difference in Doppler shift between the pump and probe for a given velocity group, we perform a weighted sum of the imaginary part of the coefficient corresponding to the off diagonal matrix element, ρ_{12}, at the probe frequency over Δ to average over the Doppler profile. We then plot the intensity as a decaying exponential function of the composite absorption coefficient. The calculation and Mathematica program for the simulation are included in the appendix.

11.) Light-shift Induced Transparency

The other method for inducing transparency is by making use of light shifts. One type of light-shift based switch is based on the kind of V-type EIT system previously discussed. We have seen from the section on saturated absorption that when a counter-propagating probe-pump pair pass through a multi-level, inhomogenously broadened atomic medium, the zero velocity atoms, as well as the velocity group at $v = \pm\frac{\Delta\omega}{2k}$ where $\Delta\omega$ is the frequency spread between neighboring hyperfine energy levels become transparent to the probe. The zero velocity atoms behave as a saturated two level system, whereas for atoms located at the cross-over velocity group, the fact that the fields are resonant for different transitions creates, in effect, a three level system exhibiting

V-type EIT as discussed earlier. This is shown in the figure below for the D1, $F = 2$ transition in RB85.

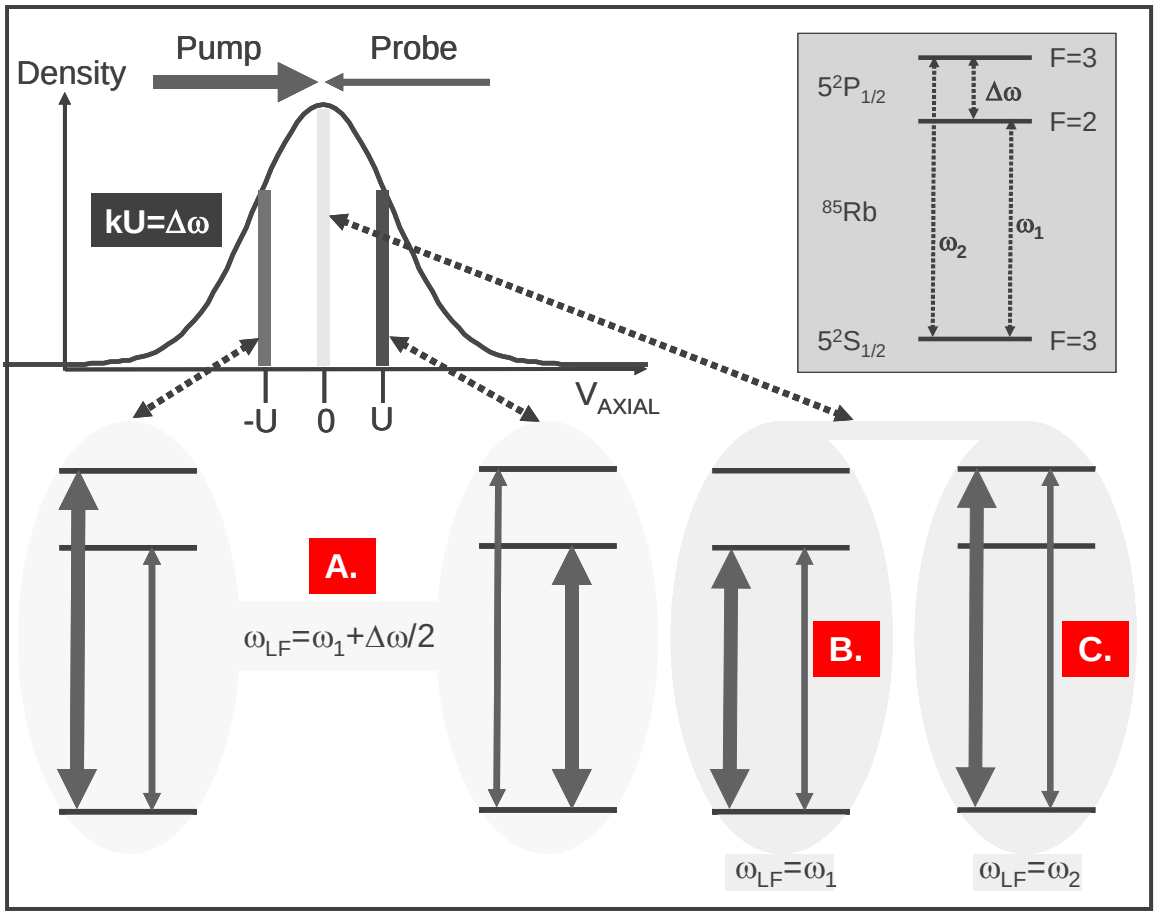

Figure 11.1: The basic mechanism behind V-type EIT

This system may be used as a switch in the following way. We note that when the pump is absent, a probe at the resonant frequency or the cross-over frequency of $\omega_1 + \frac{\Delta\omega}{2}$ will be absorbed. If a pump with intensity near saturation, centered at the same frequency, is present, the probe will be transmitted. Thus as the pump

beam is switched on and off, the output of the probe beam will also be switched. If the cross-over peak is used, this represents a V-type EIT all-optical switch.

We find that by increasing the pump intensity, the resulting light shift can induce a transparency over a broad spectral linewidth. We note that in order to induce transparency for any velocity group, the light shift Δ should be on the order of Γ. For atoms with resonant frequencies far detuned from the pump beam, the power needed to produce the same light shift as that for atoms with frequencies near resonance for the pump will be greater. The diagram below shows the pump Rabi frequency necessary to induce a light shift over a 1 GHz absorption profile in a three level pump-probe system.

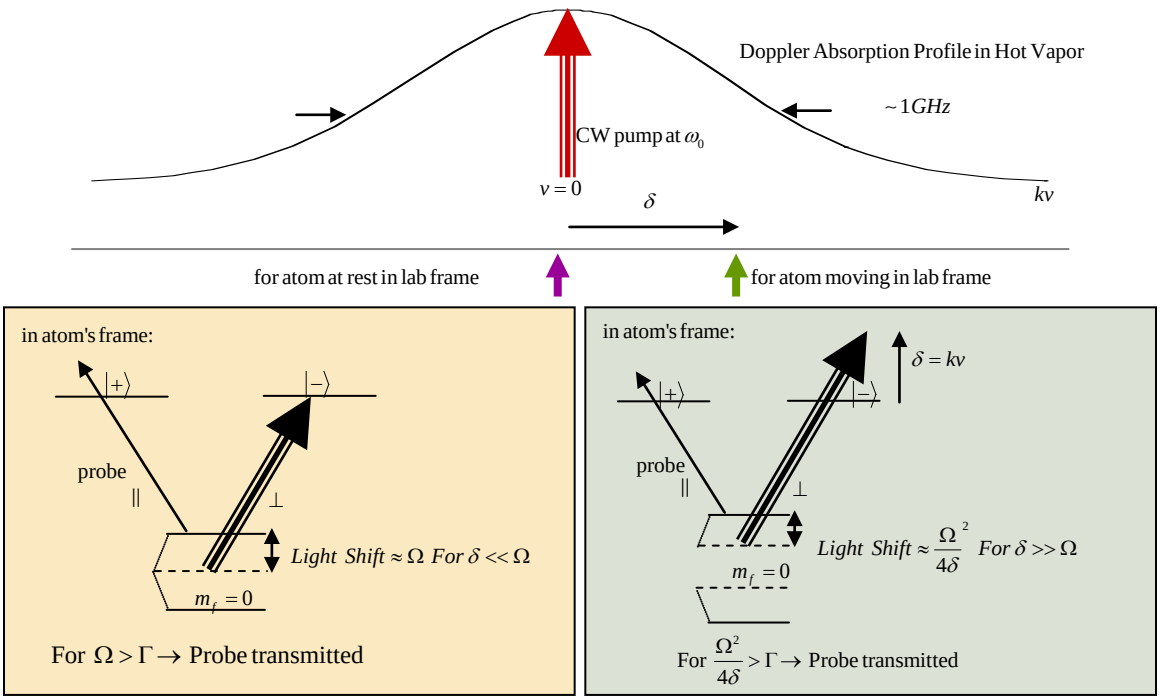

Figure 11.2: Illustration of light shift induced for different velocity groups in the Doppler profile by a CW pump centered at the resonant velocity for the zero-velocity group. When the light shift is on the order of Γ, probe transparency is induced.

For instance, for a CW pump beam centered at the center frequency of the Doppler profile, the light shift for atoms contained within the atomic resonance linewidth ($\delta << \Omega$), is on the order of $\Delta = \Omega$. The Rabi frequency necessary to induce transparency over this atomic velocity group is $\Omega \approx \Gamma$. For the same beam to induce transparency for atoms with resonant frequencies far detuned from the pump, the light shift produced is on the order of $\Delta = \frac{\Omega^2}{4\delta}$. For this atomic velocity group, the pump Rabi frequency would need to be on the order of $\Omega = 2\sqrt{\delta\Gamma}$.

In comparing the efficiency of the saturation switch versus the light shift switch we notice that in order for a pump to saturate the entire Doppler profile, we required that $\Omega_{pump} >> \delta$, where, in this case, δ is on the order of 1 GHz. We found, however, that for the light-shift switch that a smaller Rabi frequency is necessary to induce transparency over the Doppler profile, $\Omega = 2\sqrt{\delta\Gamma}$. We see that the light shift switch is a more efficient means of switching than using absorption techniques.

The light shift switch has one other advantage over the saturation switch. We note that after a transmission event, the absorption of the next probe pulse must be at a time after the decay of the saturated atoms, which is approximately 30 ns. The light-shift, however, is a spontaneous effect and immediately follows

variations in the pump Rabi frequency. If the pump field is switched off, there is no delay before the next probe pulse can be absorbed.

12.) Four Level Switch

Another proposed type of light-shift based all optical switch uses a 4 level scheme which utilizes the effect of electromagnetically induced transparency (EIT) [36,37]. The idea that one switching event of the probe costs one photon under an ideal 4 level system was first proposed by Harris and Yamamoto [38]. In their paper, they formulate the idea for the entanglement of a threefold state using this effect. Since then, Zhu [39] published results of the observation of a 4-level switch in cold Rb87 atoms. The Harris group [40] followed this result up by reporting switching at low light levels (~23 photons per $\lambda^2/2\pi$), and in 2005 the Yu group [41] reported switching at even lower light levels (~1.4 photons per $\lambda^2/2\pi$). Up to this point, however, no researcher has observed single photon switching.

The theory for the next switch follows from the earlier discussion of the three level Λ-type EIT system. Suppose we initially start with the EIT condition in place (difference detuning $\Delta = 0$), but introduce a fourth level to our atomic system as shown below:

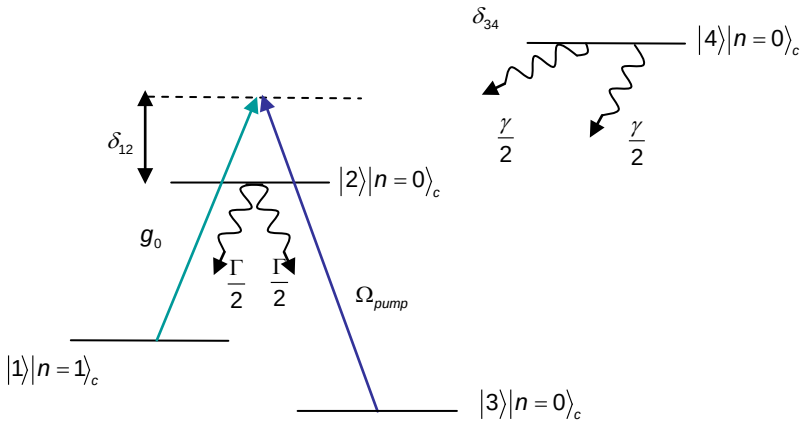

Figure 12.1: 4 Level System

If another field, close in frequency to the resonance between the third atomic state and this new state is applied, the interaction will produce new light shifted states.

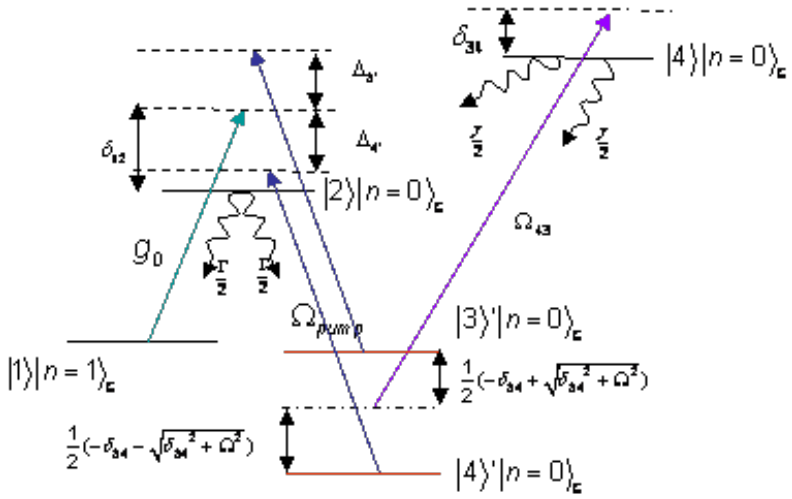

Figure 12.2: 4 Level System Including Light Shifted States

Note that $|3'\rangle$ and $|4'\rangle$ are the new dressed states which can be expressed as superpositions of $|3\rangle$ and $|4\rangle$ (equal superpositions for the case when $\delta_{34} = 0$). These light shifted states are shifted by energies $\frac{\hbar}{2}(-\delta_{34} + \sqrt{\delta_{34}{}^2 + \Omega^2})$ and $\frac{\hbar}{2}(-\delta_{34} - \sqrt{\delta_{34}{}^2 + \Omega^2})$. Since these new difference detunings between the light shifted states and the excited state $\Delta_{3'}$ and $\Delta_{4'}$ are no longer zero, we may expect our absorption curve to shift for each new difference detuning as a function of probe frequency.

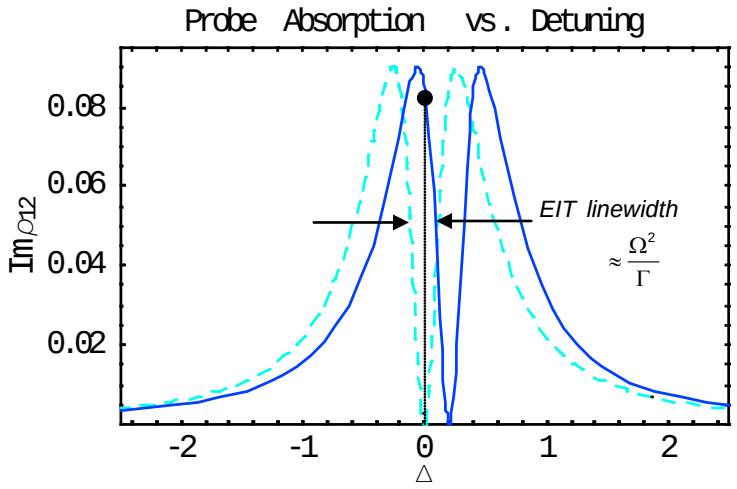

Figure 12.3: Shifting of Absorption Dip Due to Light Shift

We note that at $\Delta = 0$ the EIT condition is now destroyed, preventing full transmission of the probe. This is the basic principle of the switch

I have simulated the steady state behavior of the four level system described above. Starting with the equation (1.38) I use the Hamiltonian and decay matrix for a four level system.

$$(12.1)\quad H = \begin{pmatrix} 0 & \frac{g}{2} & 0 & 0 \\ \frac{g}{2} & -\delta_{12} & \frac{\Omega_{32}}{2} & 0 \\ 0 & \frac{\Omega_{32}}{2} & -\Delta & \frac{\Omega_{34}}{2} \\ 0 & 0 & \frac{\Omega_{34}}{2} & -\Delta-\delta_{34} \end{pmatrix}$$

$$(12.2)\quad \dot{\rho}_{decay} = \begin{pmatrix} \frac{\Gamma\rho_{22}}{2}+\frac{\gamma\rho_{44}}{2} & -\frac{\Gamma\rho_{12}}{2} & 0 & -\frac{\gamma\rho_{14}}{2} \\ -\frac{\Gamma\rho_{21}}{2} & -\Gamma\rho_{22} & -\frac{\Gamma\rho_{23}}{2} & 0 \\ 0 & -\frac{\Gamma\rho_{32}}{2} & \frac{\Gamma\rho_{22}}{2}+\frac{\gamma\rho_{44}}{2} & -\frac{\gamma\rho_{34}}{2} \\ -\frac{\gamma\rho_{41}}{2} & 0 & -\frac{\gamma\rho_{43}}{2} & -\gamma\rho_{44} \end{pmatrix}$$

We find for the case where our switching beam is off and our difference detuning $\Delta = 0$ we get the EIT profile of the three level system.

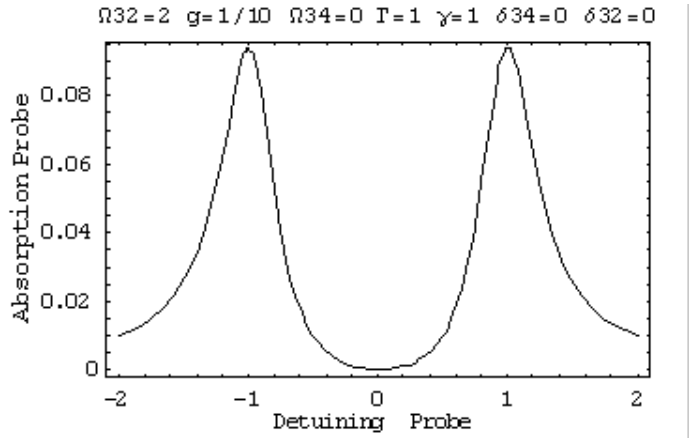

Figure 12.4: EIT Profile without Switching Beam

Note that when we begin to increase the strength of our switching beam we obtain two shifted EIT profiles due to the difference detunings of the two light shifted states.

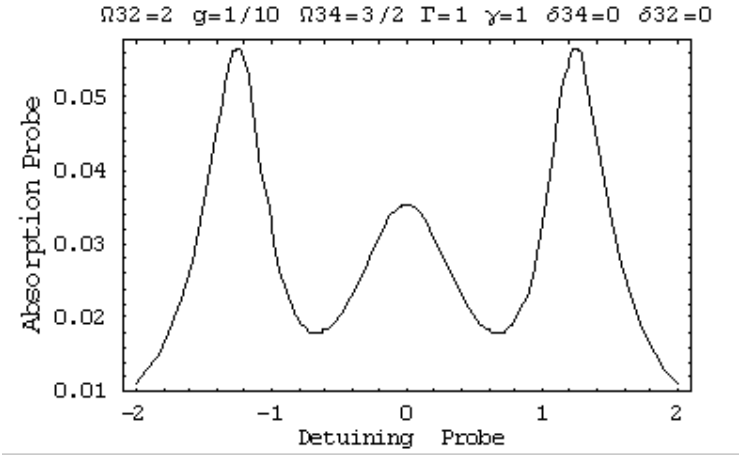

Figure 12.5: EIT Profile with Weak Switching Beam

Eventually, when the switching beam becomes comparable in strength to the pump we find that the EIT condition is completely destroyed and we no longer see evidence of dips in the absorption profile.

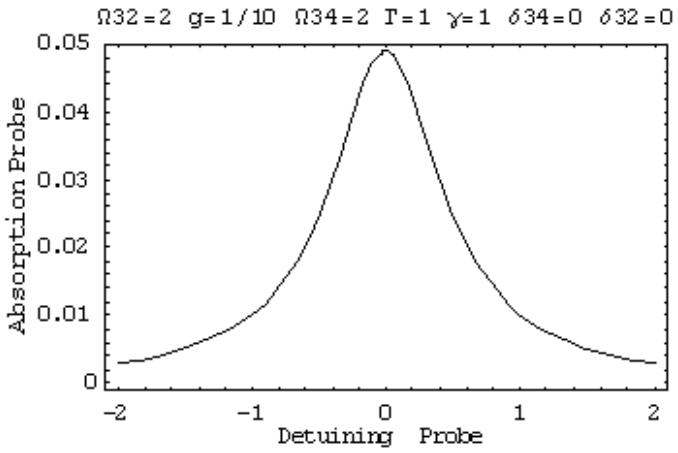

Figure 12.6: EIT Profile with Strong Switching Beam

The benefit of the four level switch is that the EIT linewidth may have a bandwidth as narrow as a few KHz. Thus the light shift necessary to destroy the EIT condition $E_{shift} = \frac{\Omega^2}{4\delta}$, need only be of that order. This is shown in figure [9] where we see that when the switching beam is applied, the center of the EIT peak becomes shifted by an amount equal to the light shift.

DEVELOPMENT OF APPERATUS

Magneto Optical Trap

13.) Theory of Magneto Optical Trap

When we wish to perform experiments with confined neutral atoms we use a Magneto Optical Trap (MOT). The MOT traps atoms using two counter-propagating red detuned beams of opposite polarization in each of the three dimensions to create an optical molasses, and a magnetic field whose magnitude is proportional to the distance from the center of the trap and whose direction flips at the traps center. The beams of the molasses are red detuned in order to apply a force in the direction opposite of the motion of the atoms. Anti-Helmholtz coils are used to apply a linear magnetic field in all three directions to split Zeeman energy levels near the center of the trapping region. This will lead to a detuning which is now position dependent as well as velocity dependent. The counter propagating beams must be oppositely polarized in order to damp the motion of the atom around the center of the trap as will be discussed below.

The main chamber of the MOT is evacuated to approximately 10^{-10} torr to avoid collisions between rubidium atoms and unwanted particles. This UHV pressure is achieved by using an ion pump. The MOT is loaded from an atomic beam achieved by heating a reservoir filled with rubidium to a temperature of about 150 C. The vaporized rubidium is collimated by the use of two small pinholes at the beginning and end of the atomic beam. This atomic beam section is kept at a pressure of approximately 10^{-8} torr by using a diffusion pump and mechanical pump combination.

For a simplified explanation of the MOT see the diagram below for the $J = 0 \rightarrow J' = 1$ configuration.

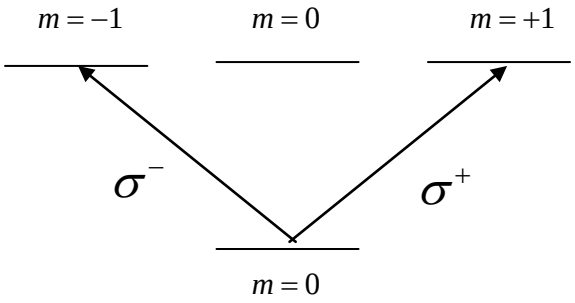

Figure 13.1: Three level system coupled by σ^+ and σ^- light

From selection rules, we know that from the J=0 m=0 state our atom can transition to the J=1 m=-1 with a photon of helicity σ^- and conversely to the J=1 m=+1 with a photon of helicity σ^+. When we apply a magnetic field using Anti-Helmholtz coils positioned symmetrically about the center of the trap, we break the degeneracy of the excited states. The magnetic field due to the coils has the form

$$(13.1)\quad B_z = B_0 \frac{1}{\pi\sqrt{Q}}\left[E(k)\frac{1-\alpha^2-\beta^2}{Q-4\alpha} + K(k) \right]$$

along the axis of the coils and

$$(13.2)\quad B_r = B_0 \frac{1}{\pi\sqrt{Q}}\left[E(k)\frac{1+\alpha^2+\beta^2}{Q-4\alpha} - K(k) \right]$$

in the radial direction, where $\alpha = \frac{r}{a}$, $\beta = \frac{z}{a}$, $Q = (1+\alpha)^2 + \beta^2$, k= $\sqrt{\frac{4\alpha}{Q}}$, $B_0 = \frac{\mu_0 I}{2a}$ is the magnetic field at the center of the coils, K(k) is the elliptic integral of the first kind and E(k) is the elliptic integral of the second kind. When plotted for an anti-Helmholtz pair with coil radius 5 cm, separation 2.5 cm, and with a current of 18 A we find

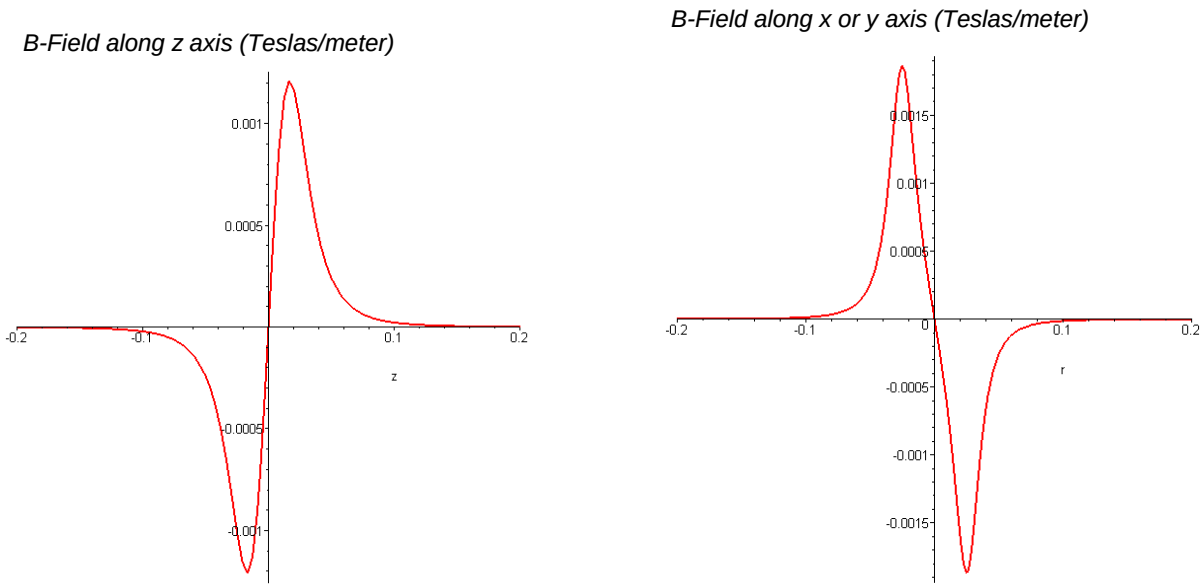

Figure 13.2: Magnetic field of anti-Helmholtz coils plotted for all three dimensions. Note that near the origin, the field is approximately linear

We see that near the center of the trapping region the field is nearly linear in all three dimensions. Ideally, the applied current should yield a magnetic gradient of 10 Gauss/cm [ref]. These magnetic sublevels will also change linearly and will be opposite in sign, since the energy of the Zeeman shift is directly proportional to the strength of the magnetic field. At the origin, the energies of the sublevels

will both be zero, but they will then diverge as we move along the axis. Red shifted light of helicity σ^+ is then applied from right to left, and σ^- light is applied in the opposite direction.

The diagram below shows the basic mechanism of the MOT in 1 dimension.

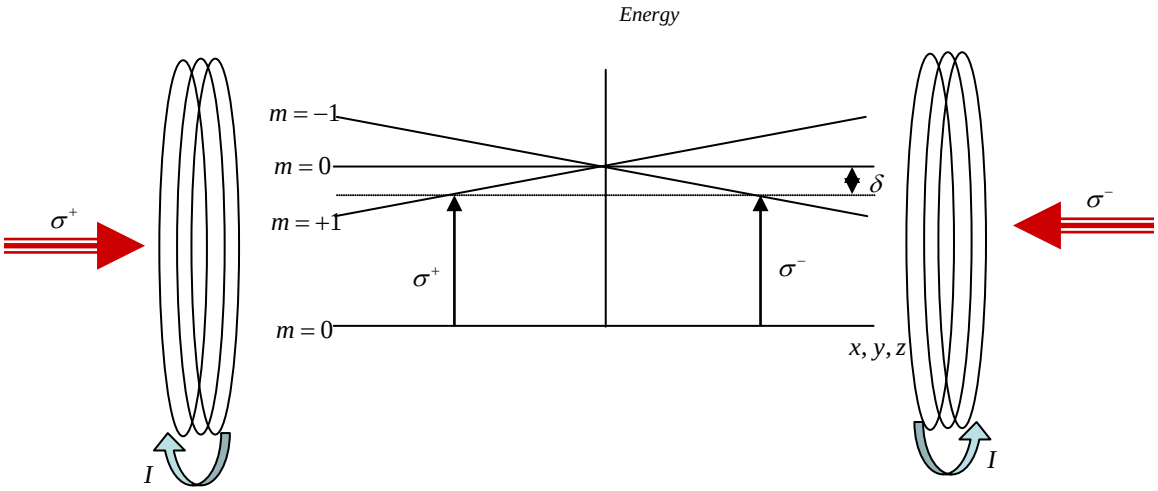

Figure 13.3: Basic concept of Magneto-Optical Trap (MOT). The magnetic field of anti-Helmholtz coils split the degeneracy of the Zeeman sublevels causing a position dependent detuning.

The two beams are detuned below resonance by δ, and serve to force atoms that deviate from the origin, back to the center of the trap. There are three cases for which this can happen. The first case is where an atom is as rest on one side of the center, let us say the right side. In this case, the σ^- light will be closer to resonance, and the atom will be pushed towards the left. Case 2 is when an atom is on one side, let us again say the right side, and moving towards the right from

the center. In this case σ^- light will be blue shifted from resonance and the σ^+ light will be red shifted by the same amount. As the atom moves from the center towards this side, the σ^- light will eventually come to resonance with the atom where as the σ^+ will not. This again forces the atom towards the center of the trap. Case 3 is when an atom is again on the right side, however this time it is moving to the left, towards the center of the trap. In this case the σ^+ light will be blue shifted and the σ^- will be red shifted from atomic resonance. In this case the σ^+ will come to resonance, damping the motion of the atom as it approaches the center. A diagram of these three cases is shown below.

Case 1: *The atom is at rest to the right of the origin*

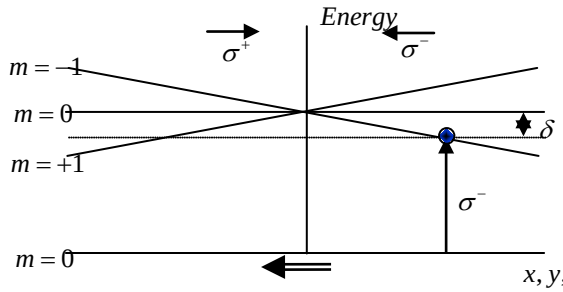

Case 2: *The atom is moving to the right on the right side*

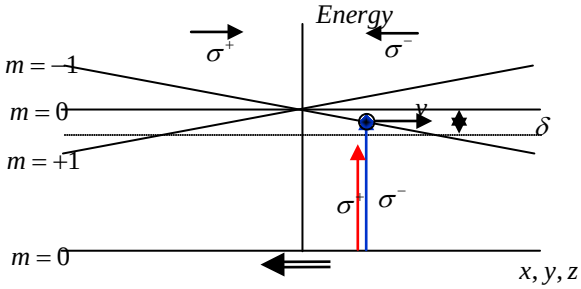

The atom will be resonant for σ^+ light which will force it back to the center

Case 3: *The atom is moving to the left on the right side*

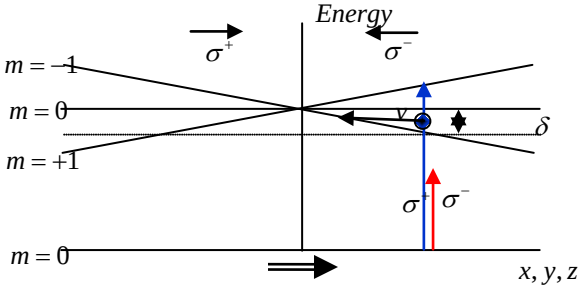

The atom will be resonant with the σ^- beam which will push away from the center in order to damp the atom's motion

Figure 13.4: Basic trapping mechanisms of the MOT

The forcing behavior of the MOT can be calculated in the following way. For the conditions $I/I_0 << 1$, $kv << 1$, $\mu B/\hbar << \Gamma$ where $|\mu B/\hbar|$ is the amount of Zeeman shift, we can find the total force on the atoms by adding the forces from the individual beams. Since the detuning is now position dependent as well as velocity dependent we find:

$$(13.3)\quad F = F_{\sigma^+} + F_{\sigma^-} = \hbar k \frac{\Gamma}{2}\left(\frac{I/I_{sat}}{1+4\left(\frac{\delta - kv - \beta z}{\Gamma}\right)^2} - \frac{I/I_{sat}}{1+4\left(\frac{\delta + kv + \beta z}{\Gamma}\right)^2} \right)$$

Note that we can write the frequency shift due to Zeeman splitting as $\omega_Z = \beta z$ since the energy of the shift varies linearly with the magnetic field. For the small velocity, small Zeeman shift limit ($kv \pm \beta z << 1$), we find:

$$(13.4)\quad F(v,z) = \frac{2\hbar k(2I/I_{sat})(2\delta/\Gamma)[kv + \beta z]}{[1+(2\delta/\Gamma^2)]^2}$$

This equation very closely resembles the o.d.e. of a damped harmonic oscillator with $\ddot{z} + \gamma \dot{z} + \omega^2 z = 0$. From this comparison we find that the damping term is:

(13.5) $$\gamma = \frac{4\hbar k^2 (I / I_{sat})(2\delta / \Gamma)}{M[1+(2\delta/\Gamma^2)]^2}$$

and natural frequency:

(13.6) $$\omega^2 = \frac{4\hbar k \beta (I / I_{sat})(2\delta / \Gamma)}{M[1+(2\delta/\Gamma^2)]^2}.$$

14.) Opto- and electro- mechanical configuration of the MOT

The use of $J = 0 \rightarrow J' = 1$ transitions is a simplified description of the MOT. In reality for the Rubidium 85 MOT, the cycling transition is between the ground hyperfine state $5S_{1/2}, F = 3$ and the excited stated $5P_{3/2}, F' = 4$, and between the magnetic sublevels $m_f = 3 \rightarrow m_f = 4$ for the σ^+ light, and $m_f = -3 \rightarrow m_f = -4$ for the σ^- light, due to optical pumping. The cooling beams, which are derived from an Argon pumped Ti: sapphire laser, are shifted 13 MHz below atomic resonance to create the molasses. This is achieved by first splitting the laser output into two parts, one to serve as the cooling beams, and one to serve as the locking beams. The locking beam is upshifted 93 MHz from the original laser frequency, by double passing through an AOM, and sent into a saturated absorption setup. Using the saturated absorption we lock the beam to the $F = 3 \rightarrow F' = 4$ absorption peak. The cooling beams are then upshifted 80 MHz from the original laser frequency by also double passing them through AOMs, This forces the cooling beams to be locked 13 MHz above resonance. These beams are then separated

into six separate beams which cool the atoms in three dimensions. This is illustrated in the diagram below.

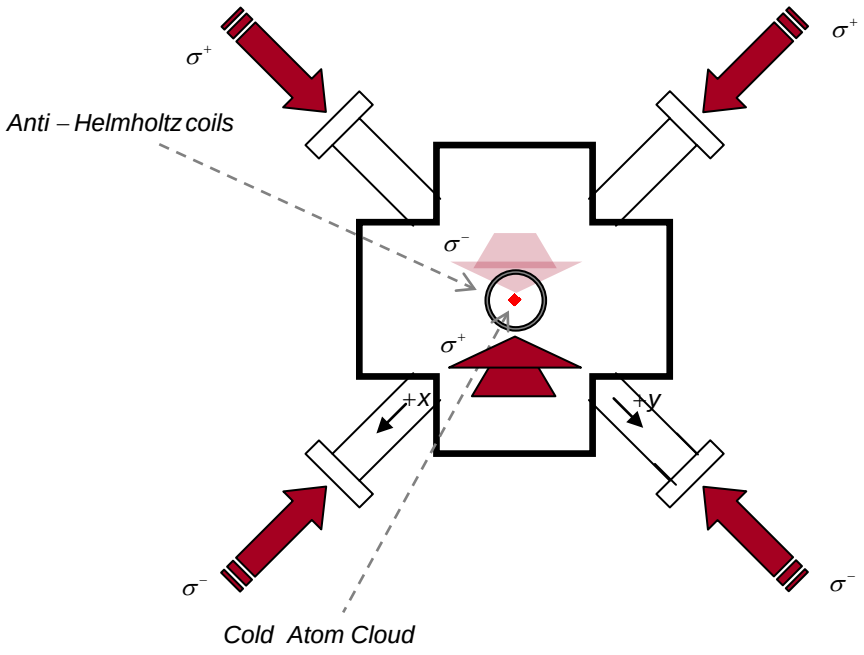

Figure 14.1: Schematic depicting MOT beams and anti-Helmholtz coils in trapping chamber

The MOT has been designed to take on two different configurations. The first configuration is for experiments in which atoms need to be launched vertically upwards out of the trapping region, such as the cavity experiments described in later sections. This configuration splits the cooling beams into three separate beams which will travel upwards, downwards and along the z-axis (perpendicular to the upwards and downwards beams). This is to set up the moving molasses technique which is discussed later in detail. A pair of anti-Helmholtz coils has been made as small as possible to accommodate short

launches. The limiting factor on the size of these coils is the size of the cooling beams themselves, since each of the six beams needs to be able to travel through the trapping region without clipping on the coils. These coils have also been built with a shelf in order to hold optical cavities approximately 3 cm above the trapping region.

The second configuration is for experiments for which the atoms do not leave the trapping region, such as the tapered nano-fiber experiments described in later sections. For these experiments a pair of anti-Helmholtz coils has been designed to be as large as possible so that more space is available for experimental beams and the fiber mount. In this case, the upwards and downwards beams are not derived from separate beams, but are rather retro-reflections of one another.

The cooling beams work on the transition $F = 3 \rightarrow F' = 4$ because this is the strongest transition in Rb 85. The hyperfine state F'=4, however, is very close to the F'=3 state, and sometimes off resonant transitions from $F = 3 \rightarrow F' = 3$ may occur. When this happens, atoms can spontaneously decay into the F=3 and F=2 states. Since the transition $F = 2 \rightarrow F' = 4$ is not allowed, these atoms will be not be able to be trapped. The solution is to supply a repump beam tuned to the $F = 2 \rightarrow F' = 3$ transition. Again, the atoms pumped into the the F'=3 state can decay into either the F=2 or F=3 state, but the atoms that fall into the F=2 state will be optically pumped out, while the atoms that fall into the F=3 state will end up back in the cycling transition. The final result is that all the atoms will get optically pumped back into the cycling transition.

Our repump beam is supplied by a Toptica TA100 tapered amplifier diode laser. Using saturated absorption we are able to lock it to the $F = 2 \rightarrow F' = 3$ transition. We have one repump entering the MOT horizontally, and one repump beam entering the MOT vertically. The vertical beam was designed to repump launched atoms that are above the trapping region while probing them with a resonant beam so their fluorescence could be imaged. A final repump beam is used in the atomic beam chirp cooling scheme as described below.

15.) Chirp Cooling of an Atomic Beam

As discussed earlier, our MOT is loaded by an atomic beam. Atoms in an atomic beam can be continuously slowed as they travel towards the trapping region. Slowing with a resonant beam however faces the same inefficiencies as mentioned earlier, since the Doppler shifted beam, as seen by the slowing atom, quickly becomes non resonant. There are two standard methods to achieve slowing of an atomic beam. One is called Zeeman slowing. The atomic beam is surrounded by a coil which has a linearly varying diameter as a function of length. When current is applied the Zeeman levels of the atoms will split by an amount linearly proportional to their location. As the atoms travel down the length of the atomic beam, the Zeeman energy splitting continuously decreases at a rate such that the cooling beam has a constant detuning in the frame of the moving atom.

The other method of slowing the atomic beam is by chirp cooling, as mentioned earlier. I will now discuss the exact details of chirp cooling pertaining

to an atomic beam. When chirp cooling an atomic beam, it is important to know such parameters as the atomic beam length, the scan rate, and the scan width. The basic problem is illustrated in the diagram below.

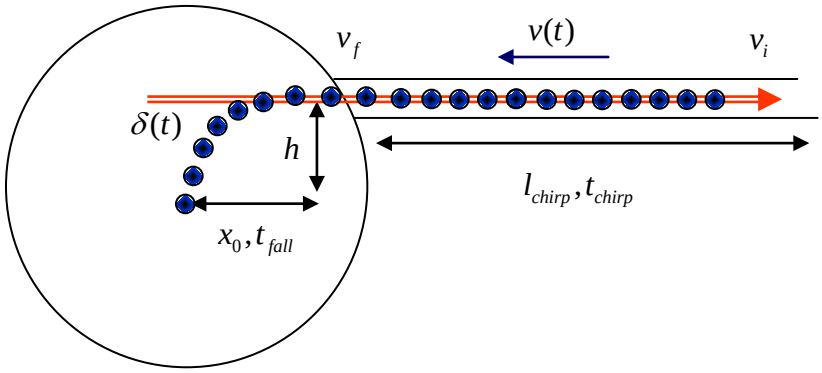

Figure 15.1: Chirp cooling an atomic beam

We wish to slow an atomic beam with initial velocity v_i located a length l_{chirp} away and a height h above the trapping region to a velocity v_f such that it falls directly into the trapping region located at the center of the main chamber. This will be achieved by slowing a group of atoms, as they travel down the length of the atomic beam section with velocity $v(t)$ in a time t_{chirp}, with a sweeping laser field. We see that if we scan our so that in the rest frame our detuning changes as $\delta_{rest} = \delta' - kv(t)$, in the frame of the atom the laser appears to stay at the detuning δ'. The acceleration of the beam on the group of atoms traveling with velocity $v(t)$ is

(15.1) $$a_{chirp} = \hbar k \frac{\Gamma}{2M} \frac{I/I_{sat}}{I/I_{sat} + 1 + \left(\frac{2\delta'}{\Gamma}\right)^2}$$

and the rate at which the laser is swept is

(15.2) $$\dot{\delta}_{rest} = -\hbar k \frac{\Gamma}{2M} \frac{I/I_{sat}}{I/I_{sat} + 1 + \left(\frac{2\delta'}{\Gamma}\right)^2} = \frac{\Delta\omega}{\Delta t} = \frac{k\Delta v}{\Delta t}.$$

Using basic kinematics we find that the time for the atoms to fall a distance h from the height of the atomic beam to the trapping region is

(15.3) $$t_{fall} = \sqrt{\frac{2h}{g}}.$$

From this time, we can work backwards to find the velocity v_f to which the atoms should be slowed to in order to fall directly into the center of the main chamber. This is simply

(15.4) $$v_f = x_0 \sqrt{\frac{g}{2h}}.$$

Now we solve for the length of the chirping section, again using basic kinematics to find the length needed to chirp cool

(15.5) $l_{chirp} = \frac{v_f^2 - v_i^2}{-2a_{chirp}}$.

We also see that the time needed for chirp cooling is simply

(15.6) $t_{chirp} = \frac{v_f - v_i}{a_{chirp}}$

and that the scan width should be

(15.7) $\Delta\omega = k\Delta v = k(v_f - v_i)$.

Our atomic beam consists of a rubidium oven at one end, and a length of 30 inches connecting the atomic beam to the chamber at the other end. The height difference between the atomic beam and trapping region is ½". We use a TUIoptics DL100 diode laser, with the edge of its scan approximately 10 MHz below the $F = 3 \rightarrow F' = 4$ transition. In practice, the way to find the center frequency of the laser sweep is to manually scan the laser and watch the fluorescence of the MOT grow brighter. A repump beam is also needed for efficient cooling, and overlaps the chirp beam down the entire length of the atomic beam.

16.) Density Measurements of the MOT

We can measure the density either by looking at the amount of absorption in a probe beam sent through the trap, or by measuring the amount of fluorescence given off by the trap itself. For the first method, we may use a low power vertical probe beam to measure the amount of absorption. We send this probe beam directly through the center of the trap, and out through the chamber onto a Hammamtsu APD. We can use a SRS DG535 pulse generator to switch AOMs, simultaneously flashing the MOT beams off and the probe beam on. (We switch the MOT beams off because the atoms we wish to probe would already be saturated.) We go through this process first with the coils on, and then again with the coils turned off in advance so that trap cannot form. In this way we can measure the amount of probe light that hits the APD when the MOT is either on or off. This difference in the probe light measured shows, directly, the amount of probe absorption. The plot below shows such a measurement taken at a power of $2\ \mu W$.

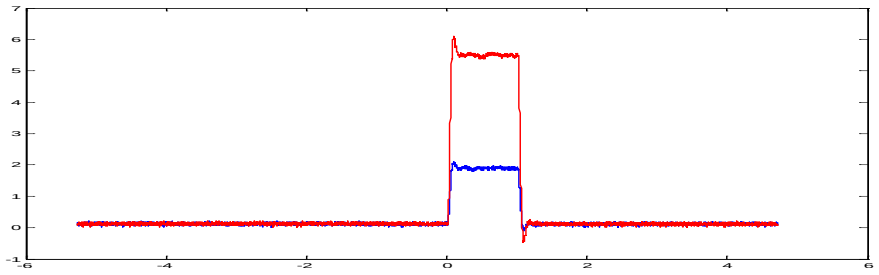

Figure 16.1 : Absorption measurements with coils on (blue) coils off (red)

In order for us to quantify the exact density of the trap, we recall the expression for the absorption coefficient derived in equation (), and note that it is a density. Using this expression we proceed in determining the density of the trap from the data shown above. If we assume our 2 μW beam is approximately 1 mm in diameter, and given that at this power we see from the plot that $\frac{I}{I_0} = e^{-\alpha L} = \frac{1.5}{6.5}$, and we assume the size of the trap is approximately 3 mm, then we find that the density is $N \approx 4 \times 10^9 \ \frac{atoms}{cm^3}$.

The second method uses direct measurement of MOT fluorescence described in http://jilawww.colorado.edu/bec/Publications/JLTP_Lewandowski2003.pdf . Here we use

(16.1)

$$Total\ \ Number\ of\ \ Atoms = \frac{4\pi(photodiode\ current)}{(solid\ \ angle)(responsivitity)(energy\ of\ \ a\ \ photon)(R)(.96)k}$$

where R the photon scattering rate in photons/sec/atom is

(16.2) $$R = \frac{\frac{I_0}{I_s}\pi\Gamma}{1 + \frac{I_0}{I_s} + 4\left(\frac{\Delta}{\Gamma}\right)^2}$$

I_0 is the total intensity of the MOT beams, I_s is saturation intensity, and k is the number of glass surfaces between the MOT and the detector. From this we estimated $N = 5 \times 10^9 \frac{atoms}{cm^3}$.

17.) Moving Molasses

To launch atoms into a cavity suspended above the trapping region of a MOT, a moving molasses technique is employed [42]. Using this method, one can move atoms upward while continuously cooling them. The basic mechanism of moving molasses is to upshift the frequency of the upward MOT beams while downshifting the frequency of the downward MOT beams while the coils are turned off. Analyzing the Doppler shift of these beams in the atoms' frame, we will derive the frequency shifts to achieve the desired height for our experiment.

The first step of the moving molasses technique is to turn off the coils in the MOT so the position dependent force along the launch axis of the MOT is gone. With the coils off there is only velocity dependent optical molasses with frequency $\omega_{molasses}$ red-shifted from resonance by an amount δ. The next step is to simultaneously up-shift the upwards beams (by an amount $\Delta\omega$ smaller than δ) while down-shifting the downwards beams by the same frequency $\Delta\omega$. Since both beams are still red shifted from resonance, but by different amounts, there will be a net force on the atoms upwards causing an initial upwards velocity. If the upwards and downwards MOT beams in the lab frame, are at frequencies

(17.1) $\omega_{up}^{Lab} = \omega_{molasses} + \Delta\omega$ and

(17.2) $\omega_{down}^{Lab} = \omega_{molasses} - \Delta\omega$,

in the frame of the moving atoms the frequencies of the beams are:

(17.3) $\omega_{up}^{Atom} = \omega_{up}^{Lab} + \frac{\sqrt{2}}{2} v k_{up}$ and

(17.4) $\omega_{down}^{Atom} = \omega_{down}^{Lab} - \frac{\sqrt{2}}{2} v k_{down}$.

At equilibrium $\omega_{up}^{Atom} = \omega_{down}^{Atom} = \omega_{molasses}$, and by plugging (17.2) into (17.4) with this condition in place we find:

(17.5) $\Delta\omega = -\omega_{mollasses}\left(\frac{v_0/\sqrt{2}c}{1+v_0/\sqrt{2}c}\right)$

With a given launch height this shift in frequency can be rewritten, using basic kinematics, as:

(17.6) $|\Delta\omega| = \left(\frac{\omega_{mollasses}}{1+c/\sqrt{gh}}\right)$.

In our experiment, our cavity was at a height of 3 cm above the trapping region of the MOT. This resulted in a frequency shift of $|\Delta\nu| = .695\ MHz$. To achieve the simultaneous upward and downward shifts in the MOT beams, we split the upwards, downwards, and longitudinal MOT beams and sent them

through three different AOMs which could all be turned on and off simultaneously by one pulse from an SRS DG535. With the laser locked using saturated absorption, 93 MHz below resonance, 1/3 of the beam is used as the longitudinal MOT beam and was upshifted 80 MHz, to allow for a detuning of δ =13 MHz, through a single pass AOM. After setting this beam passes through a waveplate to set the correct polarization, it is sent in and retroreflected back through the MOT. Nothing further was needed for this beam because it did not need to be shifted for the moving molasses.

The other 2/3 of the beam is split in half, and sent through two different double pass 40 MHz AOMs both also up-shifting the beams to 13 MHz below resonance. Double passing through the AOMs was required since these AOMs will be responsible for producing the frequency shift, and by double passing, we can ensure that the angle of the beams will not change. The two AOMs will be known as AOM 1 and AOM 2. After each beam passes through its AOM, it is again split in two. The beams shifted by AOM 1 are set to the correct polarization and are used as the upward beams, whereas the beams shifted by AOM 2 are passed through the appropriate waveplate and used as the downwards beams.

To achieve moving molasses, the upwards and downwards beams need to be shifted in frequency by equal and opposite amounts $\Delta\omega$. This is achieved by adding (and subtracting) a set voltage to the VCO controlling the upward (and downward) AOM at the exact moment the coils are turned off. A TTL pulse from the same SRS DG535 which controls the timing of the MOT beams and MOT coils is split, and after being sent through two different voltage dividers is sent to an adder and into the VCO controlling AOM 1 and through a subtractor and sent

into the VCO controlling AOM 2. The voltage dividers allow us to take the 5 V TTL pulse and set it to the correct voltage to add or subtract the appropriate $\Delta\omega$ from the upward and downward MOT beams. The result is upshifting the upwards MOT beams by $\Delta\omega$ and downshifting the downwards MOT beams by $\Delta\omega$. This produces the moving molasses.

To image the atom cloud at various launch heights, a probe beam up-shifted to be resonant with the $F = 3 \rightarrow F' = 4$ transition, and was aligned vertically upwards along the launch direction. This beam was then retro-reflected back down to ensure zero net force was exerted on the atoms. At various times during subsequent launches, the probe beam could be flashed on and the fluorescence of the atom cloud could be imaged by our Princeton Instruments PI-Max Camera. This pulsing and image-capture were both also controlled by the SRS DG535.

A schematic of the apparatus is shown below.

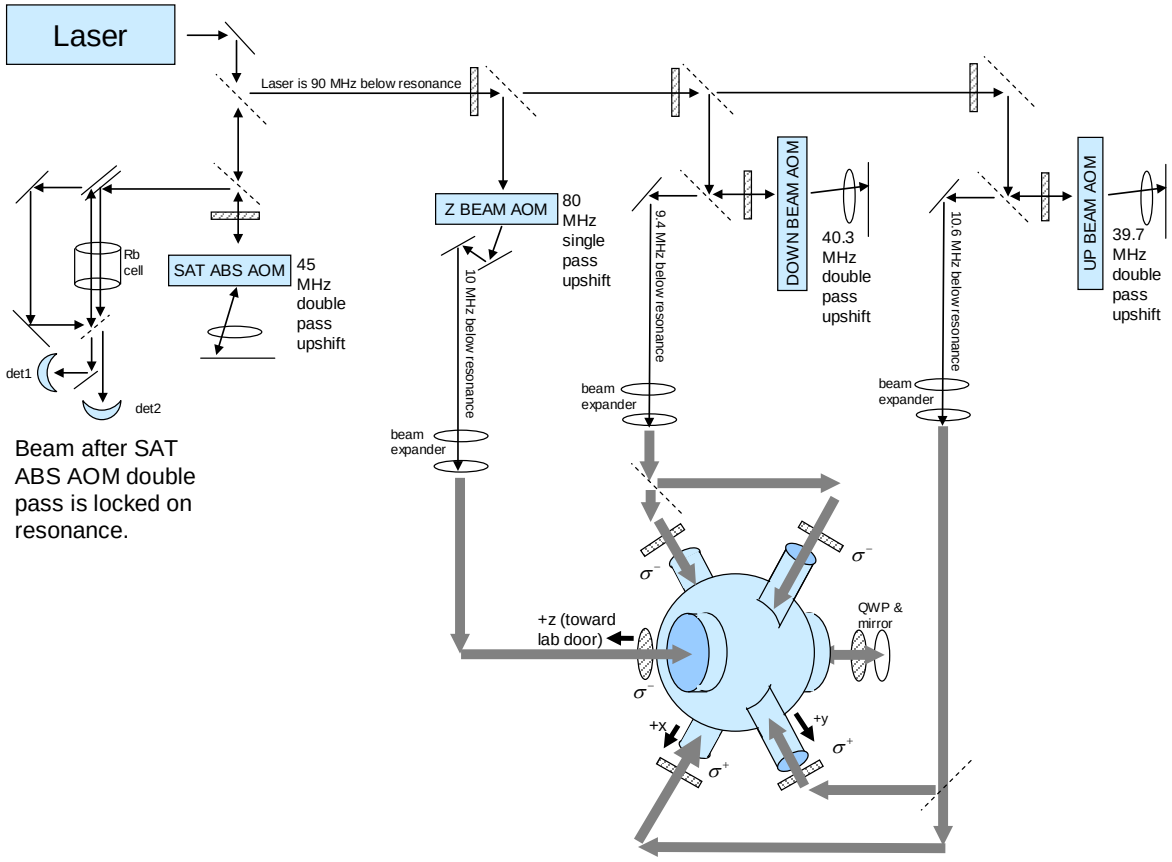

Figure 17.1: *Apparatus for Moving molasses atomic launch*

And a schematic of the component and timing diagrams are also shown:

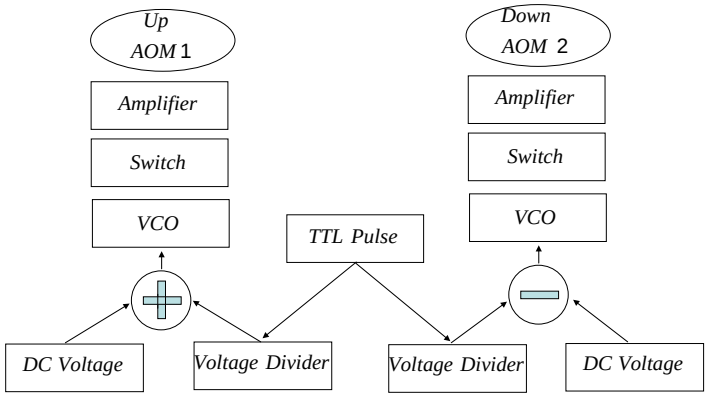

Figure 17.2: Control scheme for molasses beams

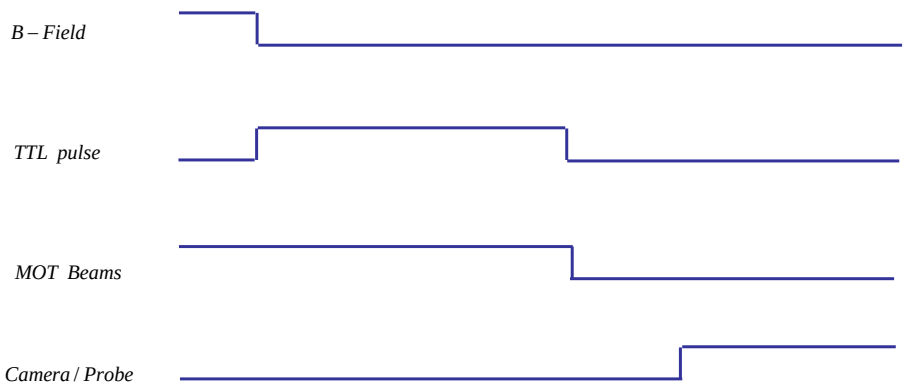

Figure 17.3: Timing diagram for moving molasses atomic launch

The pulse sequence of the MOT beams in the timing diagram shows one other detail about the moving molasses technique that we used. We see that the

MOT beams shut off before the final launch height is achieved. We found that slight misalignments and power differences in the up and down beams have large effects on the direction of the launch as the atom cloud gets higher and can actually push the atoms out of the molasses.

We were able to achieve a launch to the height of 3 cm, corresponding to the height above the trapping region that our cavity was positioned. Below are some pictures of the launch taken at times between 0 ms and 24 ms.

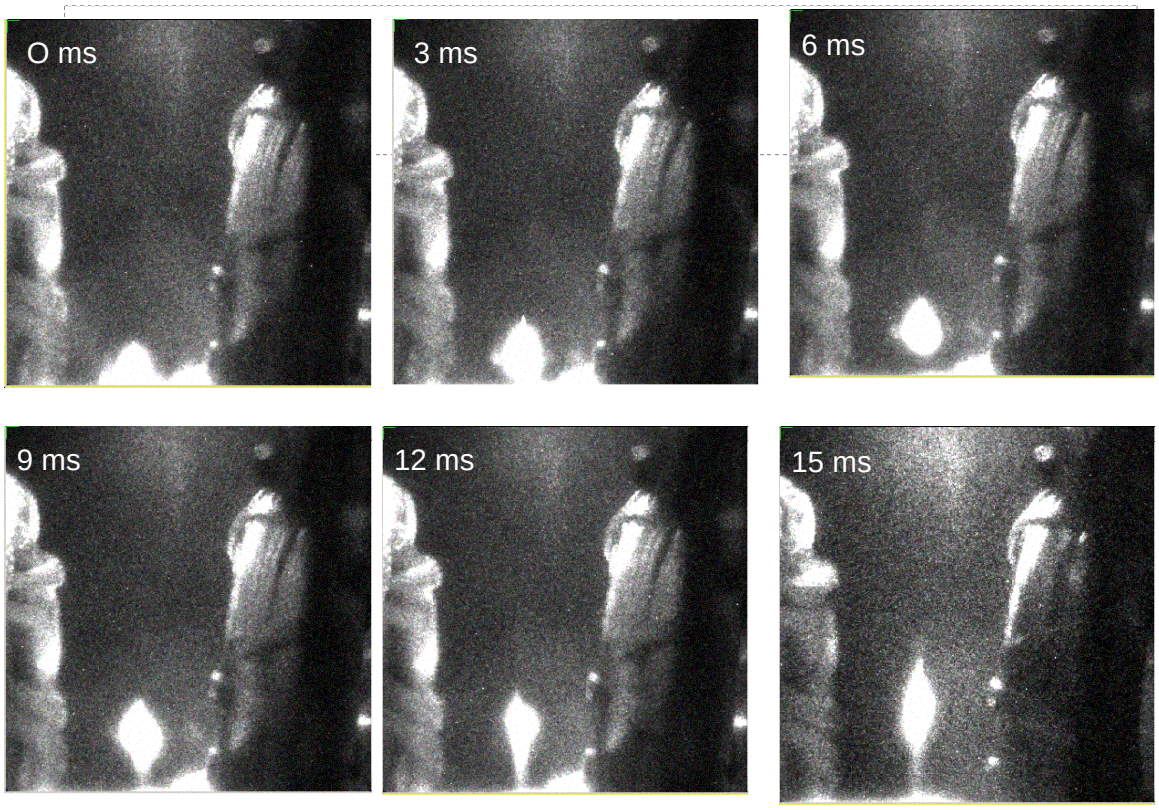

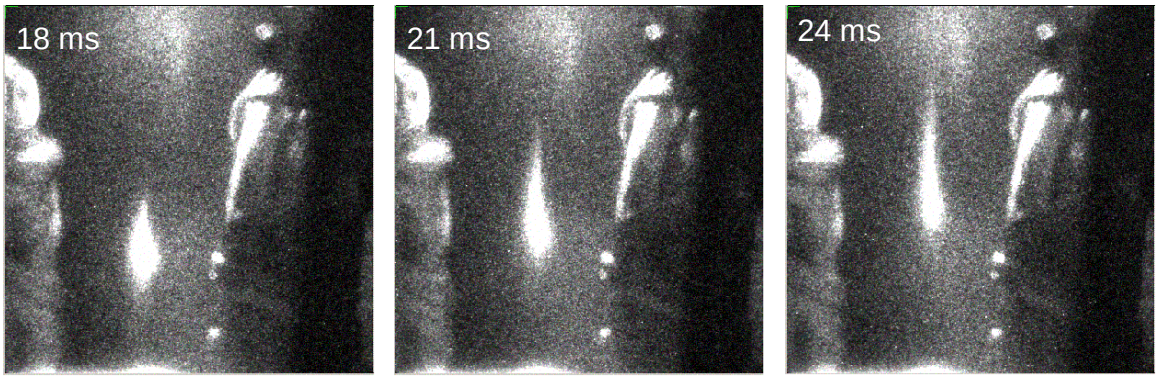

Figure 17.4: Atomic cloud fluorescence taken at various times during launch. The final launching height was 3 cm. The objects on the sides are the anti-Helmholtz coils

18.) Dipole traps

Another kind of optical force, distinct from the radiation pressure discussed earlier, is that associated with stimulated emission, and may be referred to as the dipole force. Using this one can create a conservative force which acts in all directions, to create a "dipole trap" with large trapping depth, dependent on the intensity of the beam. In order to understand the mechanism of the dipole force, we must refer to our previous discussion of the dressed states.

In the time independent basis our Hamiltonian is given by

(18.1) $$H_I = \frac{\hbar}{2}\begin{bmatrix} 0 & \Omega \\ \Omega & -\delta \end{bmatrix}$$

First note that the energies of the atomic state are separated by δ. Remember however, these are not the eigenstates of the system since they do not include the energy of interaction between the atoms and field. The eigenstates of this Hamiltonian are

(18.2) $$|\alpha\rangle = \begin{bmatrix} \frac{\delta - \sqrt{g^2 + \delta^2}}{g} \\ 1 \end{bmatrix} \text{ and } |\beta\rangle = \begin{bmatrix} \frac{\delta + \sqrt{g^2 + \delta^2}}{g} \\ 1 \end{bmatrix}$$

and the eigen-energies are $E_\alpha = \frac{\hbar}{2}\left(-\delta - \sqrt{g^2 + \delta^2}\right)$ and $E_\beta = \frac{\hbar}{2}\left(-\delta + \sqrt{g^2 + \delta^2}\right)$ which includes the energy of the atom, the electric field, and the interaction energy between them. For $\delta >> \Omega$, we recall that the energy difference between the light shifted states is approximately $\frac{\Omega^2}{4\delta}$. The diagram below depicts the energy of the system with the field both on and off for $\delta < 0$.

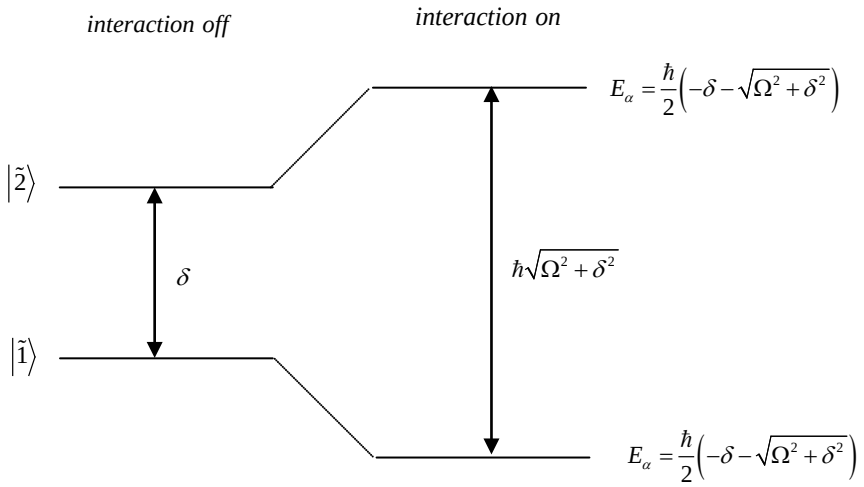

Figure 18.1: Dressed states

Note that for $\delta >> \Omega$, the amount of the light shift is approximately $\frac{\hbar\Omega^2}{4\delta}$. Now suppose the field, and therefore the Rabi frequency, has a Gaussian spatial dependence. Then the energy of the system as a function of z will appear as

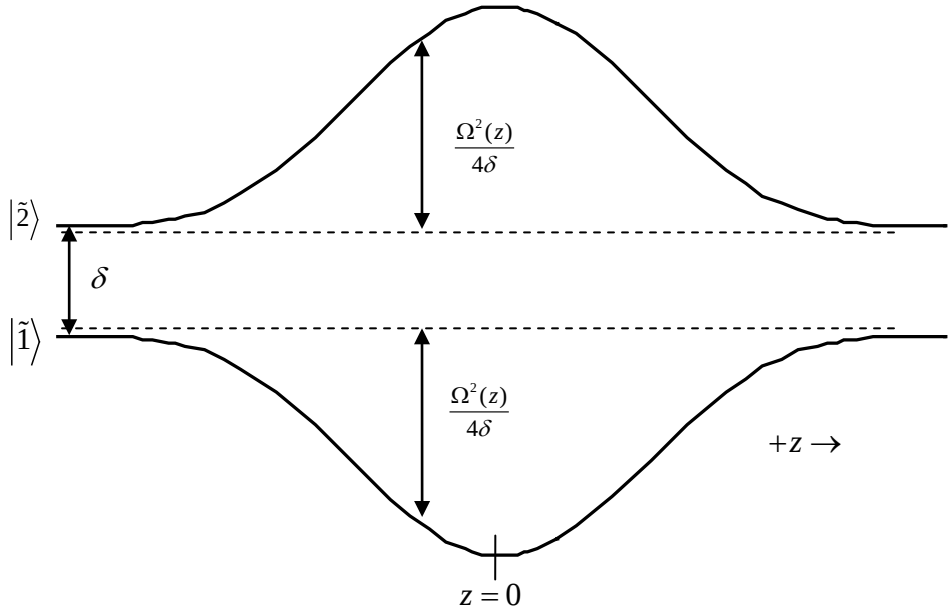

Figure 18.2: This illustrates the intensity dependent light shift used for dipole trapping, where $\Omega(z)$ *was chosen to be Gaussian.*

From this diagram we find that when $\delta < 0$ the energy of the ground state is negative. Atoms in the ground state will experience a force towards z=0, where the intensity of the beam is strongest, while atoms in the excited state will feel a force repelling them from the place of most intensity. This intensity dependent conservative force is the mechanism of the dipole trap.

If the beam is close to resonance, however, the energy gained due to scattering can minimize the efficiency of the dipole trap. We find that, since the radiation pressure force is proportional to $\frac{1}{\delta^2}$ and the dipole force is proportional to $\frac{1}{\delta}$, for large $|\delta|$ the energy gained due to scattering is minimized. Consequently trapping in a dipole trap is more efficient when the detuning is large. For this reason, this type of trap is also known as a far off resonant trap (FORT).

Since the FORT potential is intensity dependent, when aligning a fort it is important that the beam has a good profile. If there are nodes or unusual intensity fluctuations in the spatial distribution of the FORT beam, the atoms may experience many different potential wells, and not form one single trap. Below are plots of the beam intensity of a 23 micron FORT taken from both transverse planes to obtain a two dimensional beam profile. These data points were taken with a PDA55 pinhole detector on a two axis translation stage.

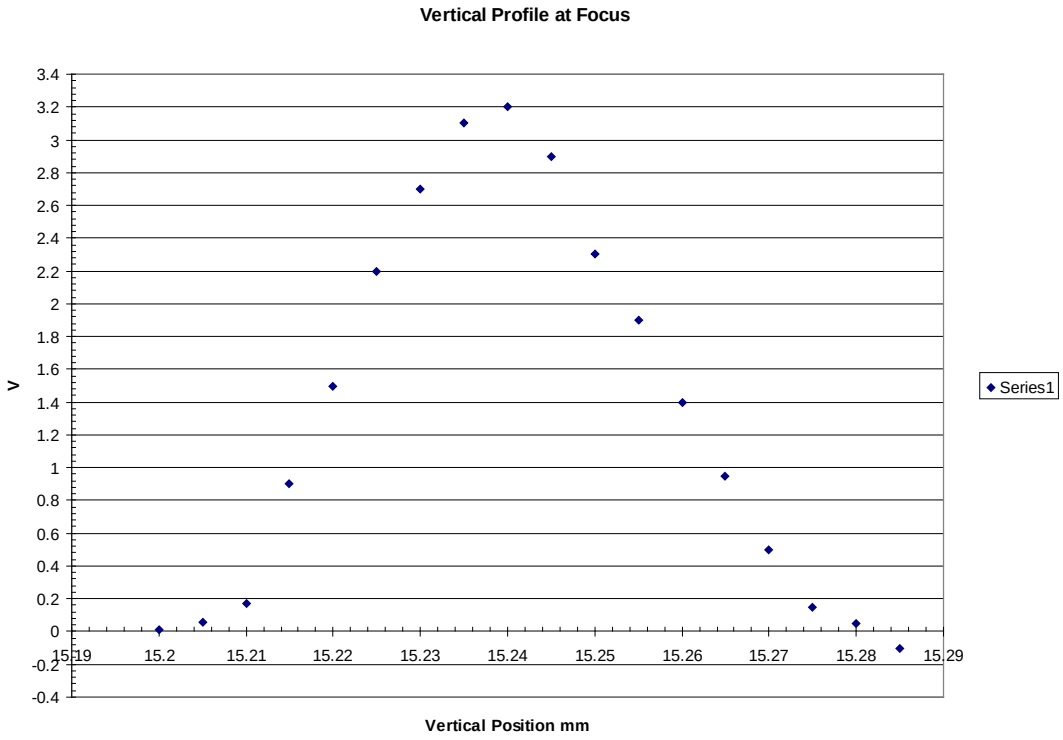

1/e width is ~25 micron

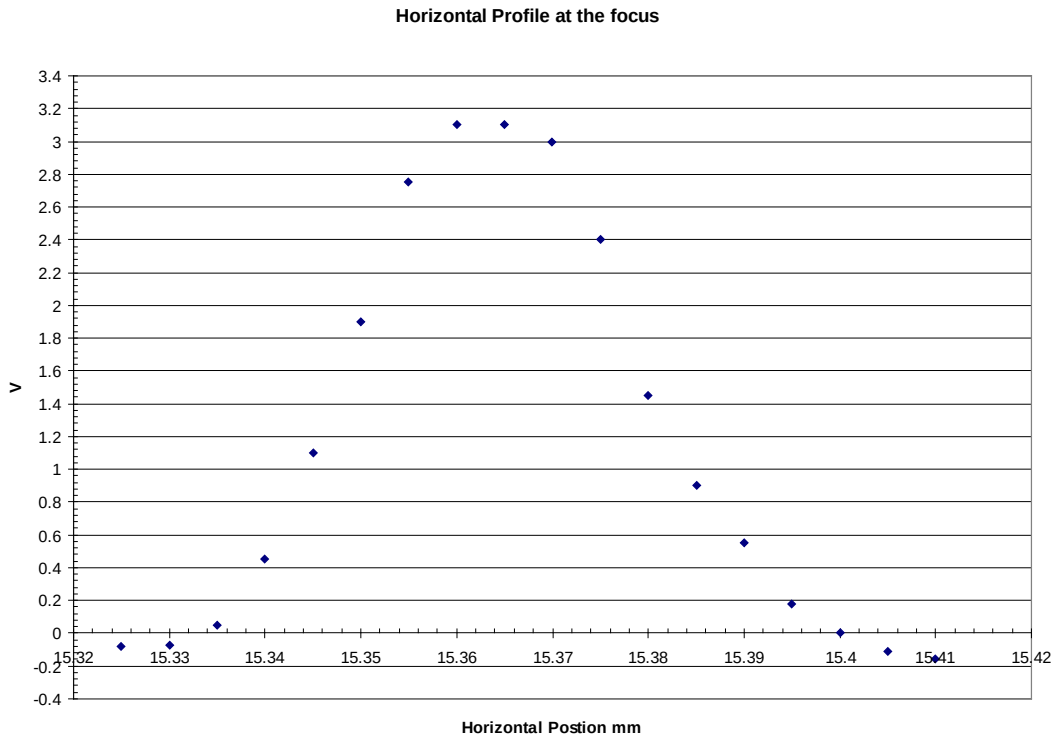

1/e width is ~23 micron

Figure 18.3) Vertical and horizontal mode profiles for FORT beam. The waist of the beam is approximately 25 microns

Below is a surface plot of the energy of a FORT along the longitudinal and transverse directions. The wavelength is 810nm (due to the need to be far detuned from both the D1 and D2 transitions) the waist is 25 microns and the intensity is .5 W.

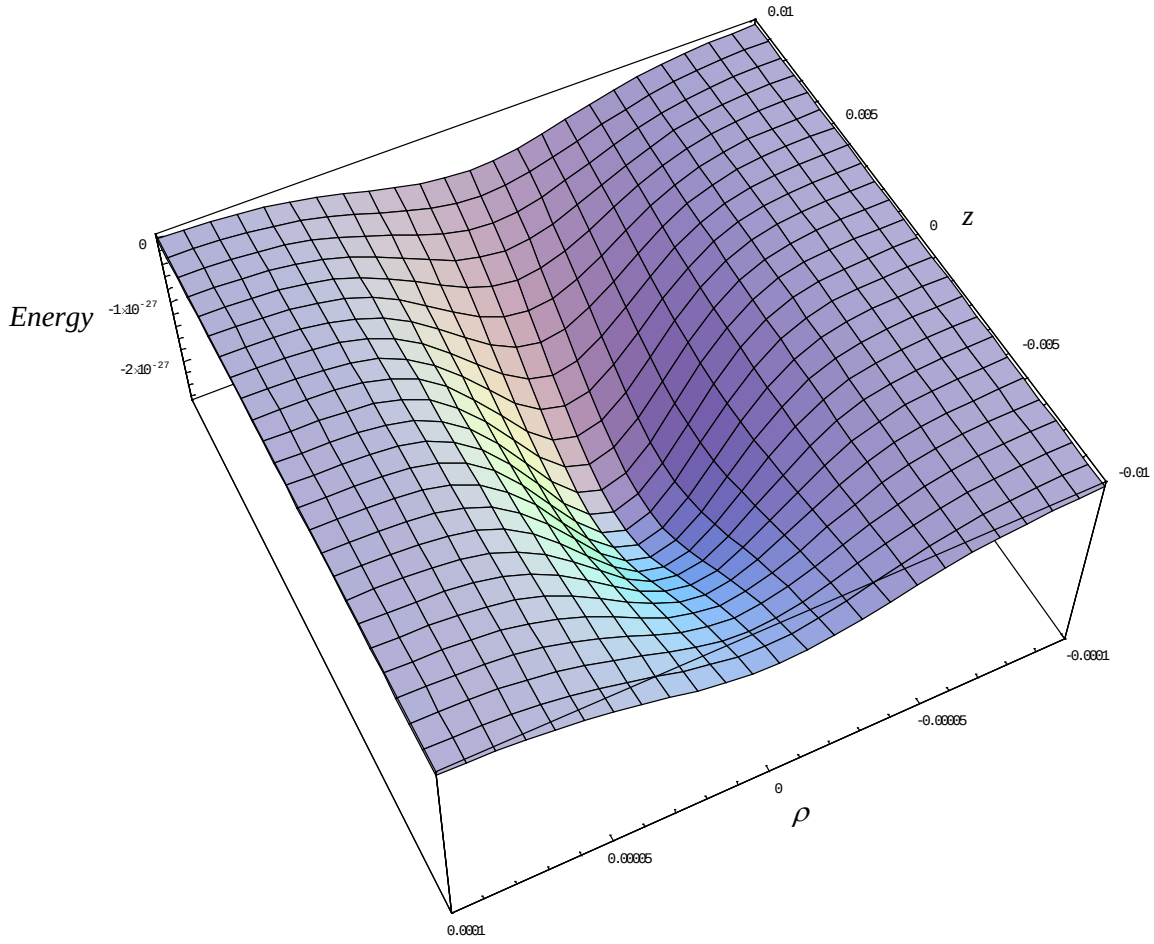

Figure 18.4: Surface plot showing trapping potential in three dimensions of FORT.

The energy minimum located at the focal point is $E_{fort} = 2.6 \times 10^{-27}\ J$. If we assume the trap to have a temperature of approximately $100\,\mu K$, we find the kinetic energy due to the velocity of the atoms is $E_{vel} = 1.38 \times 10^{-27}\ J$. The energy gained per atom per millisecond can be written as

(18.3) $$E_{scatter} = \rho_{22} \Gamma \frac{\hbar^2 k^2}{2000M}$$

and is found to be $1.55\times10^{-30}\ J/s$. The lifetime of the fort can be calculated by setting

(18.4) $E_{scatter}t_{fort} + E_{vel} = -E_{fort}$

and solving for t_{fort}. For this case the FORT lifetime is 788 ms.

Enhancing Atom-Field Interactions

To minimize the energy cost per switching event we would like the switching beam and probe to be efficient at low optical powers. To improve switching efficiency we must increase the interaction strength between the atoms and our beams. One way to accomplish this is to increase the number of atoms that interact with our beams. The other way to increase interaction strength is to increase the electric field strength per photon.

19.) Collective Enhancement

The first method of increasing the total number of atoms allowed to interact with the field, also known as collective enhancement [43], follows from the idea that our collective total ground state of our system comprises N atoms all in their individual ground states, and the total excited state comprises 1 atom in

its excited state and N-1 atoms in their individual ground states. We can write the wave function for the ground state of this N atom system as:

(19.1) $$|G\rangle = |g_1, g_2, g_3, ..., g_j ..., g_{N-1}, g_N\rangle$$

and the wave function for the total excited state as:

(19.2) $$|E\rangle = \sum_{j=1}^{N} \frac{1}{\sqrt{N}} |g_1, g_2, g_3, ...e_j, ...g_{N-1}, g_N\rangle$$

We find that the coupling rate between these ground and excited states can be calculated simply as:

(19.3) $$\langle G|H|E\rangle = \sqrt{N}\Omega .$$

We find that our interaction strength has increased by the square root of the total number of atoms allowed to interact with the field. It is for this reason that a large MOT density is desirable.

Cavity

20.) Cavity Theory

The other method of increasing interaction strength is to increase the effective electric field of each photon. One way of doing this is to allow the atoms to interact with photons in a cavity. First we note that if we restrict ourselves to a tightly focusing cavity mode, equation (2.17) tells us that our vacuum Rabi frequency g increases inversely proportional to the square root of the mode volume of our field. Next, note that if we solve for the field strength for a field trapped in a cavity with mirrors of reflectivity r_1, r_2, r_3 as in the figure below:

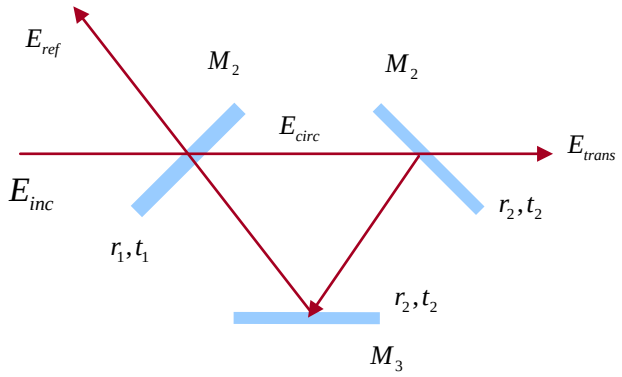

Figure 20.1: Three Mirror Ring Cavity

we find that the electric field inside that cavity adds as a geometric sum in the following way:

(20.1) $$E_{circ} = t_1 E_{inc} + t_1 E_{inc} (r_1 r_2 r_3) e^{-ikL} + t_1 E_{inc} (r_1 r_2 r_3)^2 e^{-i2kL} + \ldots$$

which simplifies to:

$$(20.2)\quad E_{circ} = t_1 E_{inc} \sum_{n=0}^{\infty} (r_1 r_2 r_3)^n e^{-inkL} = \frac{t_1 E_{inc}}{1-(r_1 r_2 r_3)e^{-ikL}} = \frac{t_1 E_{inc}}{1-\sqrt{R_1 R_2 R_3}\, e^{-i(\phi_0 + kL)}}.$$

When we solve for the increase in intensity inside the cavity we find:

$$(20.3)\quad \frac{I_{circ}}{I_{inc}} = \frac{T}{(1-\sqrt{R_1 R_2 R_3})^2},$$

For a set of given reflectivities, the circulating intensity contained within the resonator can be many times larger than the incident intensity, resulting in a higher rate of intra-cavity atom-field interactions [44].

21.) Design of cavity

To increase the effective field strength of both the switching beam and the probe, I have designed a pair of interlocking three mirror ring cavities having overlapping, tightly focused beam waists. A hole in the base plate of the cavity located at the point where the two foci overlap allows for a three beam overlap of the pump with the probe and switching beam. For this reason, the polarization of the pump beam must be orthogonal to that of the probe and switching beams, which will be s-polarized due to mirror reflectivity constraints. This allows us to choose to make the pump beam circularly polarized. This will be important when determining which transitions are allowable from selection rules between the energy levels of the four level system and will be discussed later.

A schematic of the cavity along with the mirror mount designs are shown below, as well as a sketch of the geometric constraints on a three mirror design. Four of the six mirror mounts were built with a hinge-like mechanism which provides the two degrees of tilt freedom needed to align the cavity. The other two mirrors have piezos positioned under their mounts so they can be used to scan and lock the cavity. The voltages to the piezos were supplied by vacuum compatible Kaptan insulting wire connected to a medium capacity UHV compatible current feedthrough. The perimeter of each of the two ring cavities is 4 cm, and the radius of curvature of the input couplers is 2 cm. The input angle is 10 degrees relative to the normal to minimize astigmatism, and the waist is approximately 10 micrometers in radius. The reflectivities of the mirrors (all for s-type polarization) are 98% for the input coupler, 99% for one of the optical flats, and 98.6% for the transmitting mirror. Due to size constraints, one side face of the output coupler had to be polished so that light could be transmitted out the back surface of the mirror after being totally internally reflected off this side face.

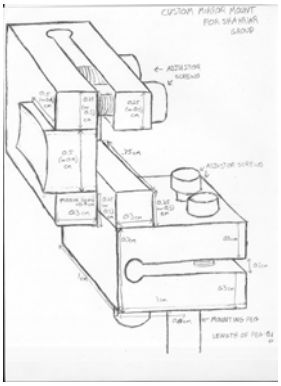

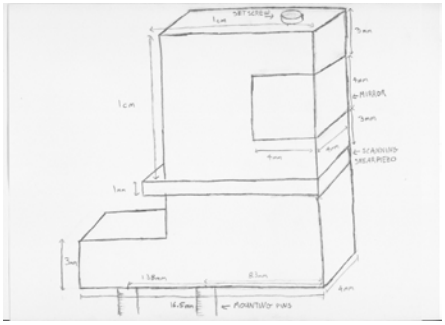

Figure 21.1: Input Coupler Mount *Figure 21.2: Scanning Mirror Mount*

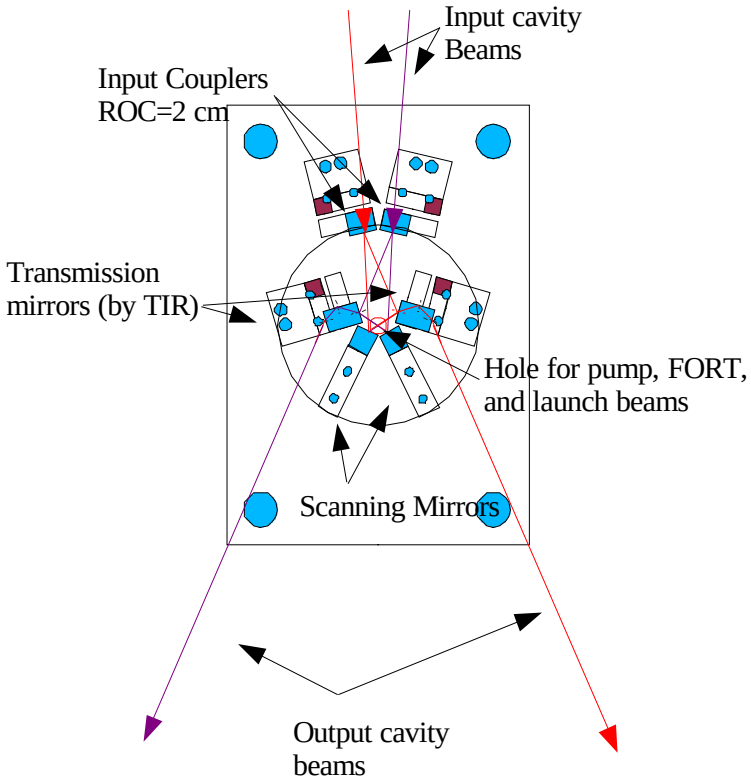

Figure 21.3: Cavity Schematic

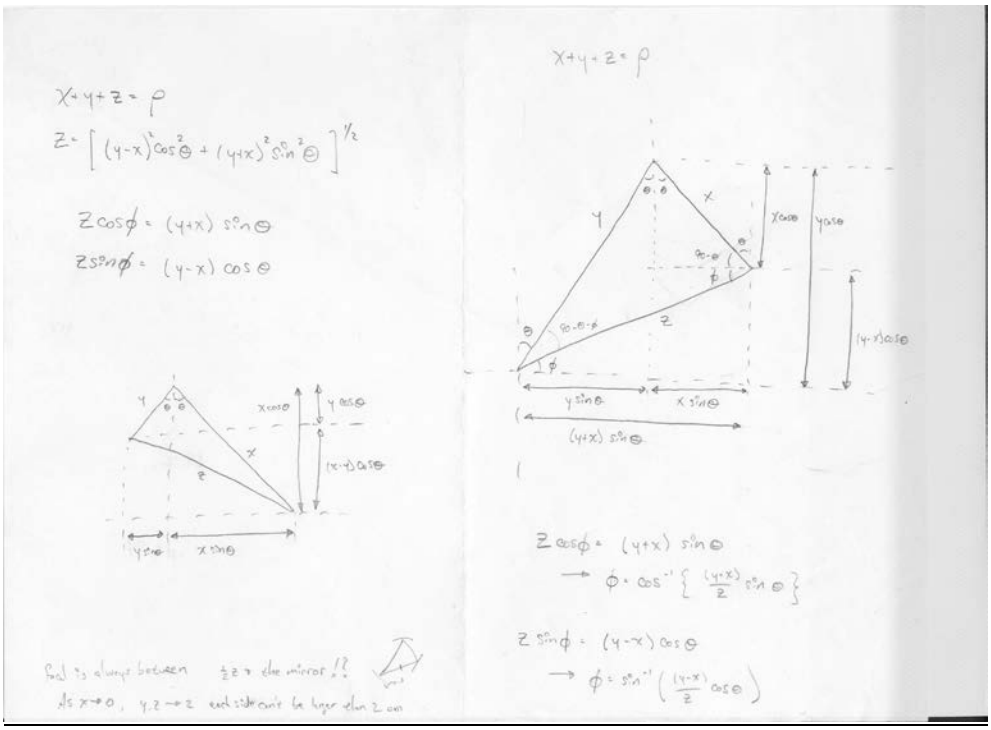

Figure 21.4: Original cavity model for calculating mirror angles

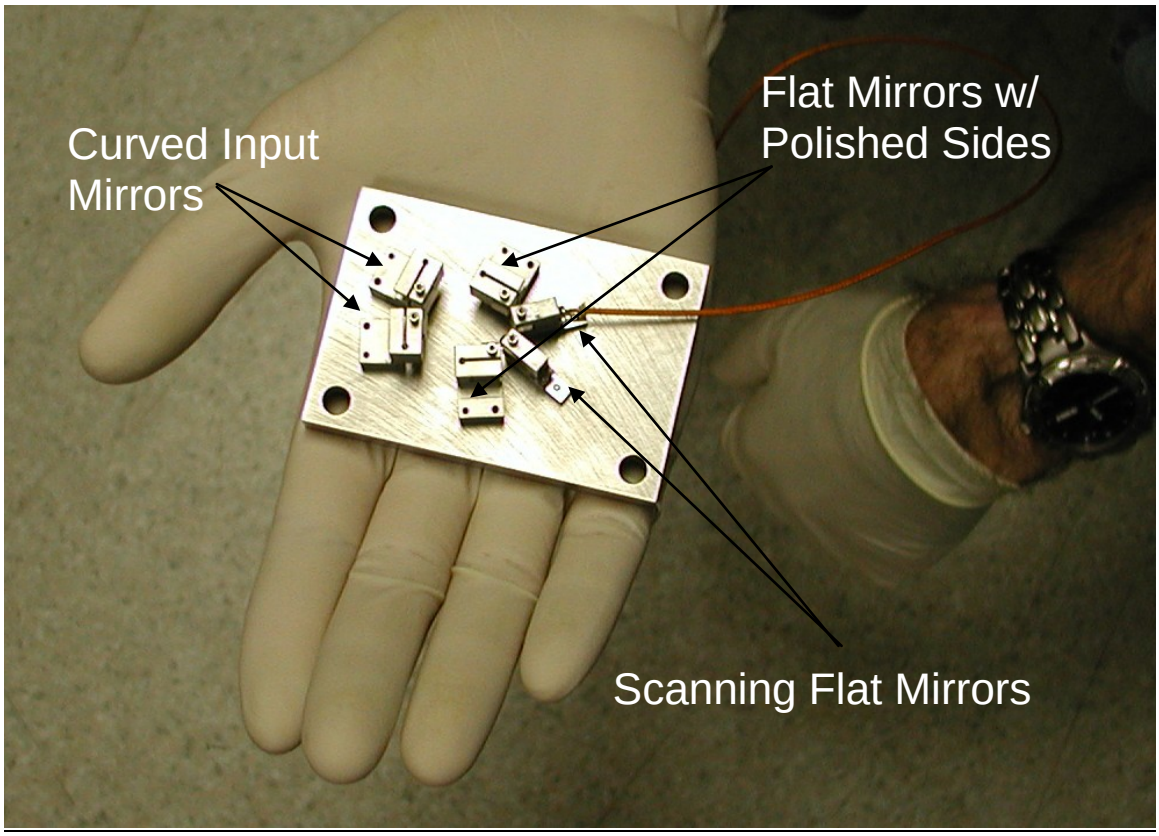

Figure 21.5: Photographic of cavity

22.) Mode Matching

Unlike the case of a two mirror cavity for which input beams may enter normal to the mirror surface, the input beam of a three mirror traveling wave cavity must enter at an angle. The input beam traveling at an angle through the curved input coupler, will experience astigmatic aberrations. As a consequence, the beam spot at the cavities effective focal point will have different diameters in the sagital and tangential planes. If this astigmatism is not taken into account, the beam which is coupled into the resonator may not have the correct cavity

mode, resulting in large beam distortions after only a small number of passes around the cavity. Proper mode matching had to be taken into account to maximize the effective intensity build up inside the resonator [45]. Cavity parameters were chosen to minimize these astigmatic effects such as the mirror ROC, and the entrance angle of the cavity.

Due to symmetry, the focal point of a three mirror cavity having one curved mirror should be located a distance one half the perimeter from the curved mirror. Beginning from this focal point, ray tracing matrix methods were used to propagate the beam once around the cavity. The propagation was done for the sagital and tangential plains separately. To solve for the waist in each plane at the focal point, we set the initial beam waist before propagation equal to the expression describing the waist after propagation. We can solve this equation for the beam waist in each plane. We define the waist at the focus in the tangential plane as w_{fT}, and the waist in the sagital plane as w_{fS}.

The next step is to determine what type of optics outside the cavity are needed for mode matching. This again is achieved by using matrix ray tracing methods for both the sagital and tangential planes. We propagate the beam from the focus of the cavity through the input coupler and to a distance equal to where mode matching optics may be set up. This distance, defined as d, is selected base upon the constraints of the system. Since the cavity will be placed in the center of the spherical MOT chamber, the mode matching optics need to be positioned a distance away larger than the radius of the chamber. At the distance d from the cavity focus we find the waist and radius of curvature of the beam in

both planes. We define these as R_{dT}, and w_{dT} for the radius and waist in the tangential plane, and R_{dS} and w_{dS}. We then solve to find what type of lens would collimate a beam having these parameters. This is equivalent to finding what type of focal length lens is needed to focus a collimated beam with sagital and tangential radii and beam wasits R_{dS}, w_{dS}, R_{dT}, w_{dT} a distance d to a final sagital and tangential focused beam with waists w_{fS} and w_{fT}. Note that the focal length in each plane required will be different, and generally a composite cylindrical lens system may be needed. In the case of this cavity however, the difference in focal lengths needed for the two planes was negligible as will be seen.

For a curved input mirror of 2 cm ROC and a perimeter of 4 cm, the first set of calculations yield a tangential beam waist $w_{fT} = 20\mu m$ and sagital beam waist $w_{fS} = 30\mu m$ at the focus of the cavity. Choosing a distance $d = 18\,cm$, we found the beam waists and radii at the mode matching optics as $R_{dS} = -20cm$, $w_{dS} = 20mm$, $R_{dT} = -20cm$, $w_{dT} = 30mm$. The focal length of the lens needed was calculated in one plane as $f_T = 19.62cm$ and $f_s = 19.64cm$. The standard lens closest to this focal length that we had on hand, however, was one with a focal length of $f = 20cm$. Using this focal length lens, one could work backwards, and recalculate a working distance d that would match the cavity beam parameters. For the sagital plane this working distance worked out to be 18.35 cm which was very similar to the working distance in the tangential plane which was calculated as 18.37. Lastly, note that due to astigmatic effects, the beam entering the mode

matching optics had a waist size in the sagital plane $\frac{3}{2}$ times larger than that of the tangential plane. This was corrected for by using two ananmorphic prism pairs, one that expanded a beam 3 times in the tangential plane, and one that expanded the beam 2 times in the sagital plane. All calculations for mode matching are included in the appendix in the form of MAPLE and Mathematica worksheets. The resonance of the cavity was measured in the reflection from the input coupler. On resonance, this reflection is minimum, as shown in the figure below.

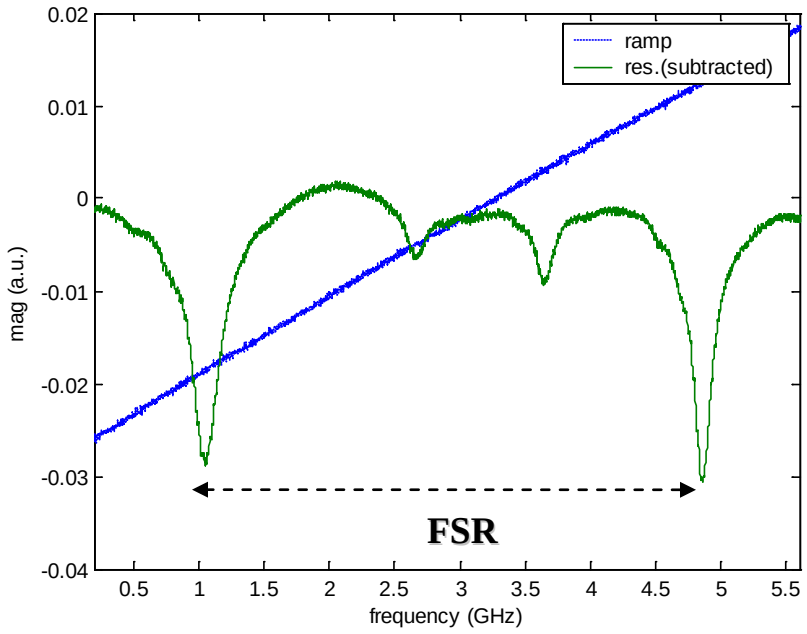

-- Observed finesse ~ 30, FSR ~ 4 GHz

Figure 22.1: Observed cavity resonance data

23.) Cavity – MOT Experiment

The cavity was designed to be mounted with the mirrors suspended from the base plate, 3 cm above the trapping region, as shown in the photograph below.

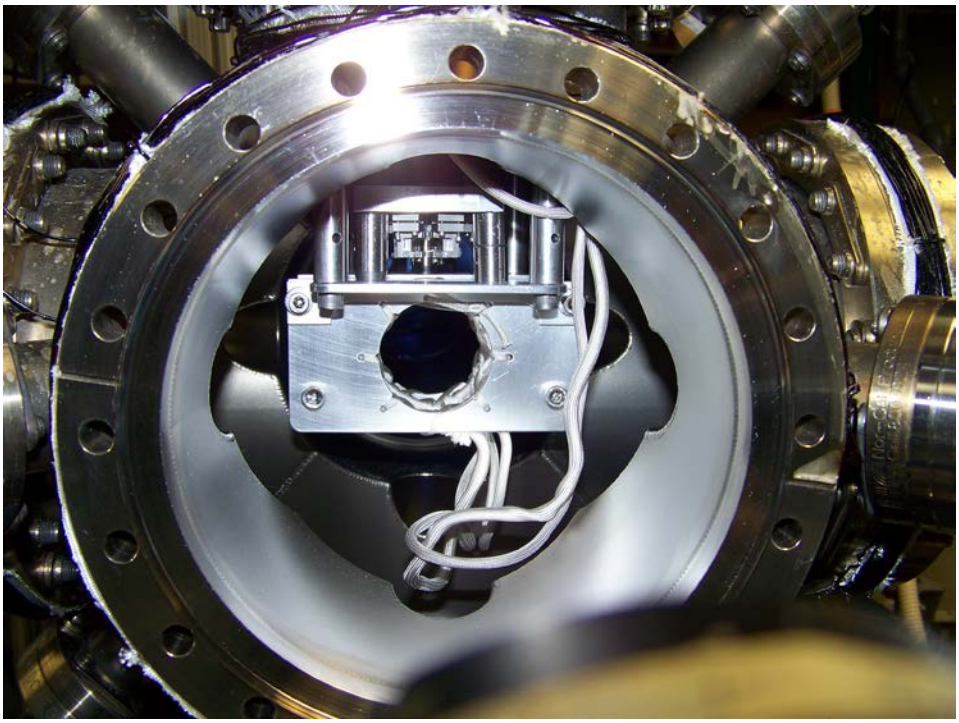

Figure 23.1: suspended by base plate over trapping region

Using the moving molasses techniques, atoms are launched toward the point where the two cavity foci overlap. During the experiment described below, the atoms are held in place by a vertical FORT beam, which focuses tightly at the

location of the overlapping cavity foci. The 4-level EIT switching experiment must then be performed within the lifetime of the FORT.

The four level switching scheme will use energy levels forming the N-system shown in the diagram below. The probe will couple the Zeeman levels of the $5s_{1/2}\ F=2 \rightarrow 5p_{3/2}\ F'=2$ while the pump will couple the Zeeman levels of the $5s_{1/2}\ F=3 \rightarrow 5p_{3/2}\ F'=2$ transitions. When the difference detuning between these beams is zero we achieve our two photon resonance condition.

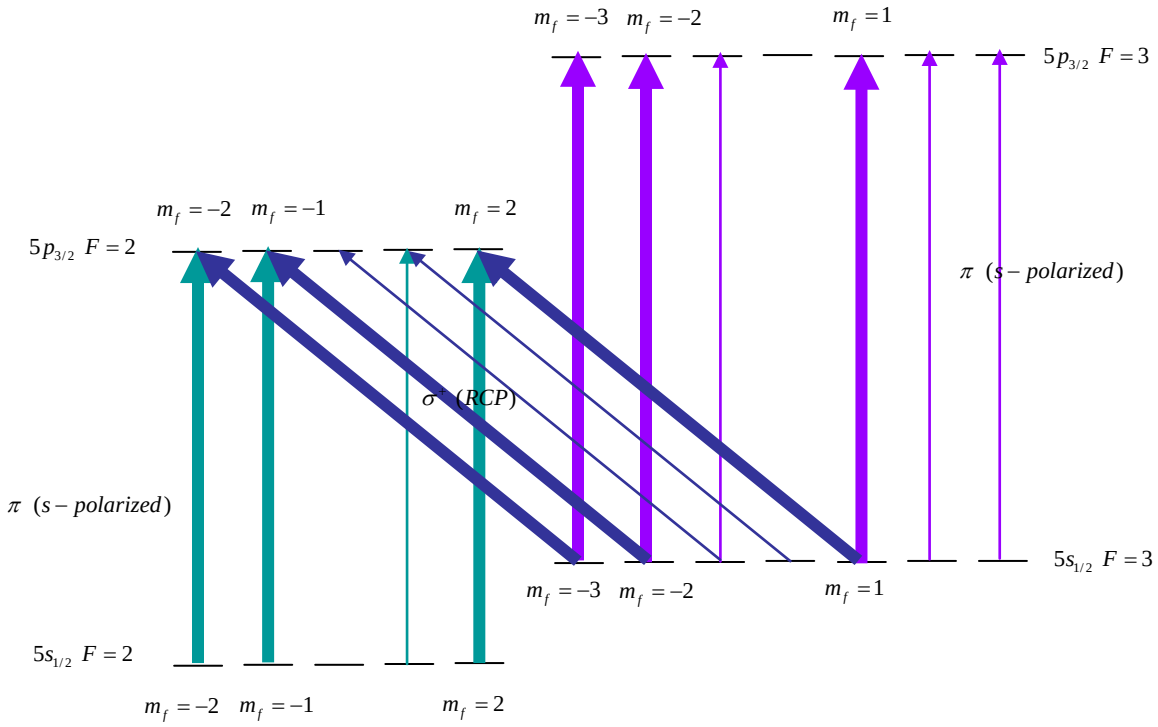

Figure 23.2: Energy Diagram for 4-Level System. Arrows in Bold Indicate Transitions Used for Switch

Since the reflectivities of the cavity mirrors depend on the angle of incidence (AOI) and polarization type, s-polarized light was chosen for the cavity beams to achieve proper reflectivities for the relevant incidence angles. Since the pump beam travels in the direction orthogonal to the s-polarized cavity beams, the polarization of the pump must also be orthogonal. If we choose the pump beam to be circularly polarized, and if we pick the quantization axis of our hyperfine levels to be in the direction of travel of the pump beam, the pump will allow σ^+ transitions ($\Delta m_f = +1$), while the cavity beams will cause π transitions ($\Delta m_f = 0$). This creates a three channel N-system, where each channel independently adds to the total switching effect.

An experimental schematic diagram is shown below. Along with the MOT beams, the repump beams and the chirp cooling beams, it shows the FORT beam overlapping the pump beam. The weak cavity beams will likely enter the cavity through UHV compatible fiber optic couplers.

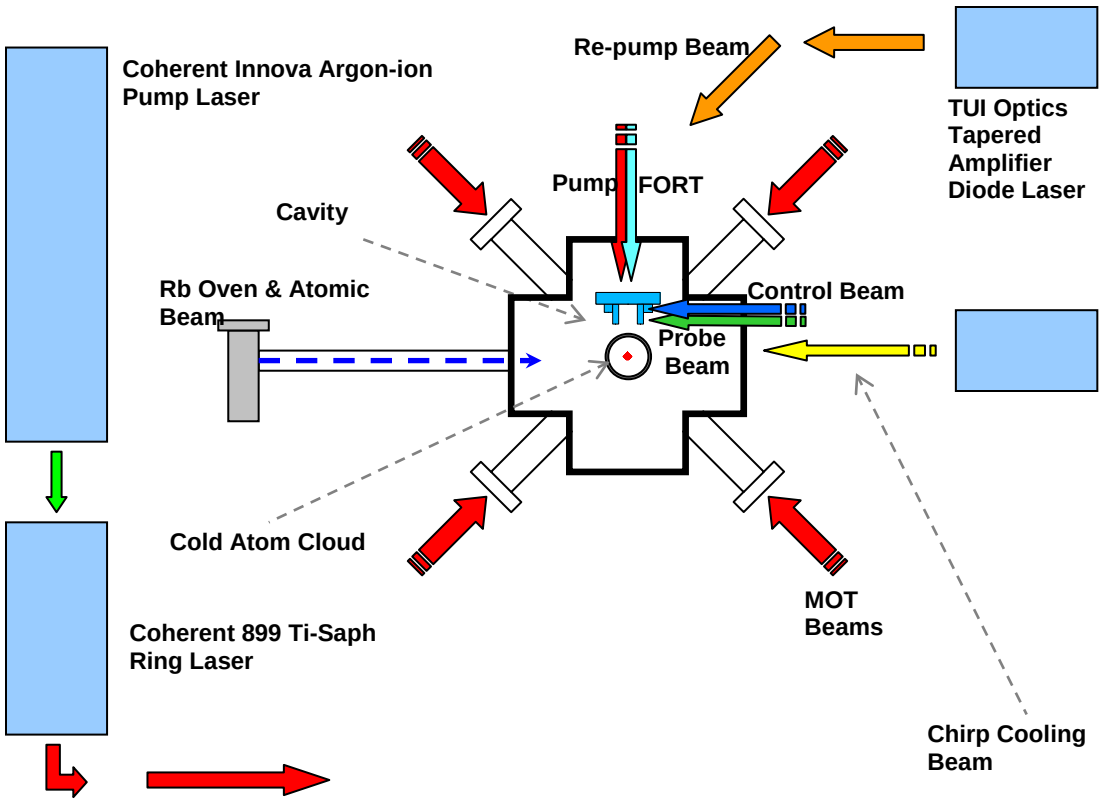

Figure23.3: Schematic of Experimental Setup

The experiment can be summarized in the timing sequence shown below. The first step of the experiment will be loading the MOT for which the MOT beams, the atomic beam chirp and repump, and the MOT repump will all be on. The probe and switching cavity beams will simultaneously remain on as cavity locking beams. After the MOT is fully loaded, which could take up to 10 seconds, the MOT beams are frequency shifted to produce the moving molasses. Once the atoms are at rest, at the top of their trajectory, in the cavity, the FORT will turn on and remain on for the duration of the experiment. We then pulse the probe on 100 μs. At this time if the switching beam remains on, we would expect very

little transmission of the probe from the cavity. If the switching beam is turned off during this 100 μs window, we would expect to measure cavity transmission of the probe.

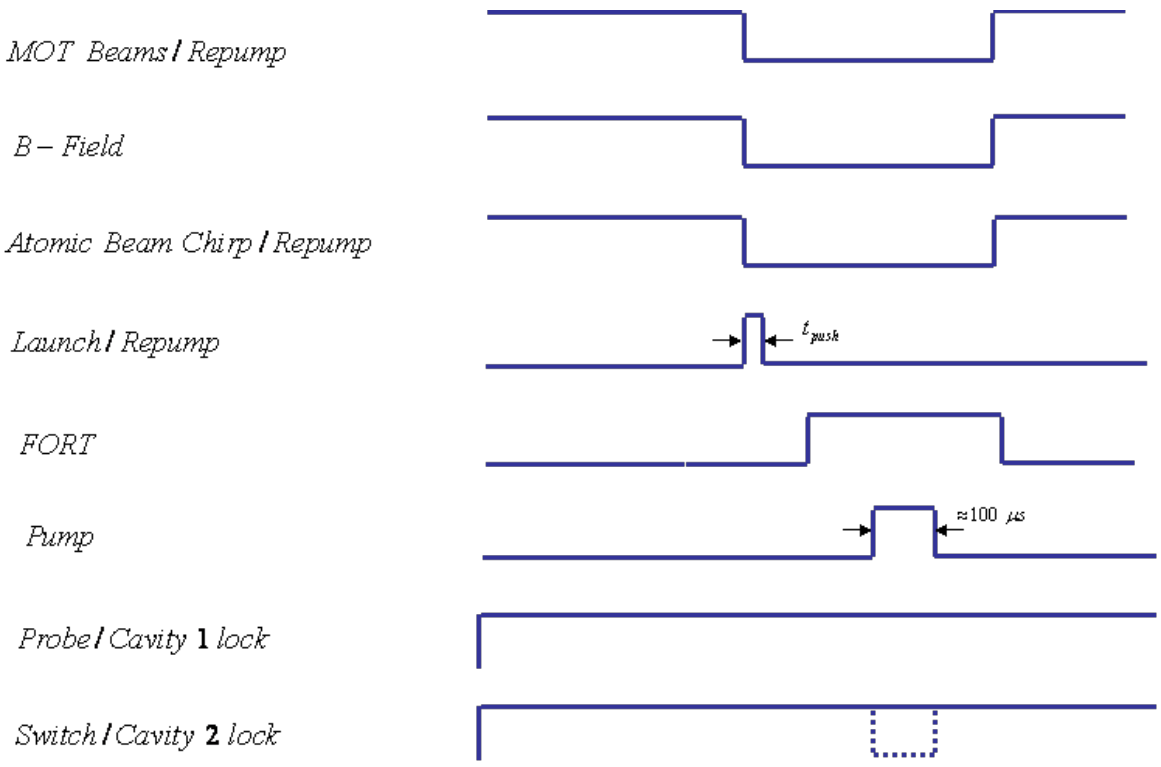

Figure 23.4: Experimental timing diagram for cavity-MOT experiment

Tapered Nano Fiber

Another method for increasing field intensities involves the use of tapered nano- fibers (TNF) [46, 47, 48,]. An advantage of using TNF over optical resonators is that switching may be implemented directly in optical fiber.

24.) TNF Theory

The TNF consists of standard single mode silica optical fiber for which a small section, approximately 3 cm, is heated and pulled so that the diameter in this region is reduced to approximately 500 nm. The mode guided by the fiber will adiabatically decrease in mode area as it travels down the tapered region, increasing in intensity to as much as 60,000 times the original intensity. (With this type of enhancement, saturation of a stationary Rb atom can be achieved at approximately 20 pW.) The fiber will also convert the original mode from one which is guided by the core/cladding interface to one which is guided by the cladding/environment interface [49]. This results in an evanescent mode which leaks into the environment. When inserted into either atomic vapor or cold atoms, this evanescent field can interact directly with the atoms. This is illustrated below

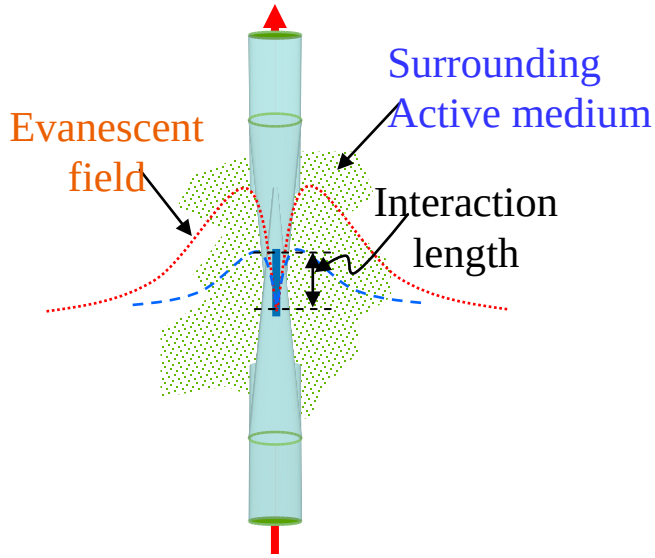

Figure 24.1: This figure illustrates a tapered nano-fiber (TNF).

Numerical simulations of the TNF yield the data shown below [] and are also reported in [50,51,52]. The first plot shows the fraction of energy located in the evanescent field and mode volume as a function of fiber diameter. We find that the minimum mode area, .2 μm^2, is obtained for a fiber diameter of approximately .45 μm. As the diameter is reduced further, the mode quickly delocalizes causing a rise in mode area. At this diameter, we find that that fraction of energy outside the fiber corresponds to approximately 10%.

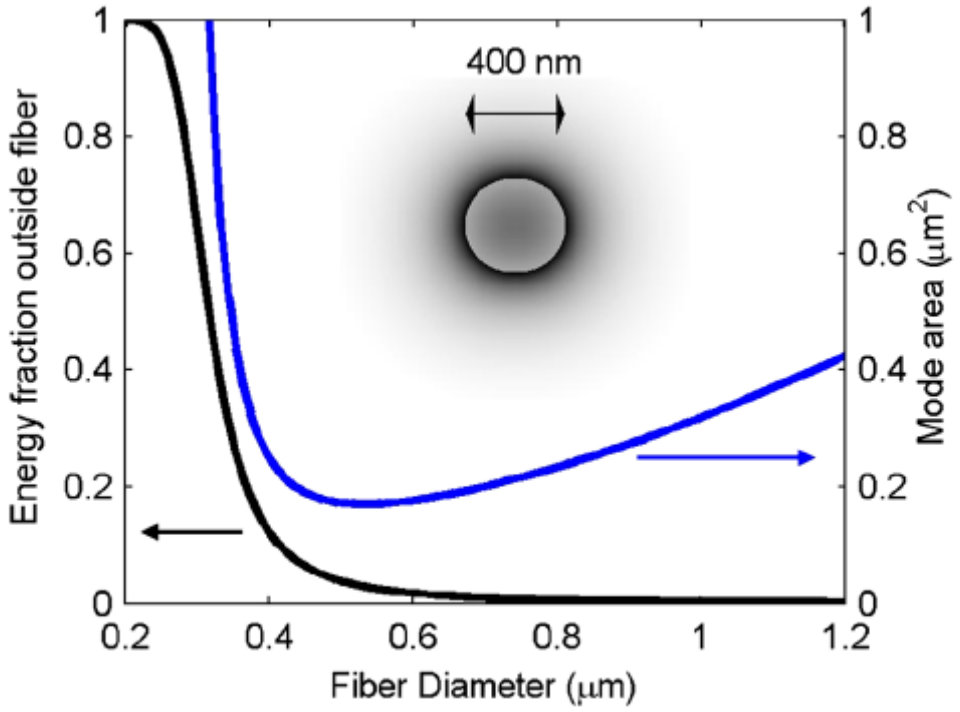

Figure 24.2: Fraction of mode energy outside fiber (black) and Mode are (blue) versus the fiber diameter

Atoms with velocities typically found in hot vapor can pass through the small mode area of the TNF in a few nanoseconds. This is much shorter than the natural decay time of the atom (approximately 25 ns) and leads to an effect known as transit time broadening. We can understand transit time broadening by picturing the field from the reference frame of the moving atom. As the atom moves through the field, it experiences a temporally varying field with a shape dependent on the transverse optical mode field. This pulse has a spread of frequency components determined by its Fourier transform. To observe the broadening of atomic linewidth, one may scan the laser supplying the TNF field. As the laser scans through frequencies which are nonresonant in the lab frame,

the pulse seen by the atom may still have a component at the resonant frequency and consequently still be partially absorbed . Furthermore, due to energy conservation, the total power of the pulse must be distributed among the frequency components dictated by its Fourier transform. For this reason, when the laser is tuned to resonance, the power contained in the component of the field at the resonant frequency will be less for an atom moving through the field than for a stationary atom. This results in higher saturation powers for atomic vapor. Note that effects due to transit time broadening are negligible in cold atoms. The figure below shows calculated transit time linewidth and saturation powers as a function of taper diameter.

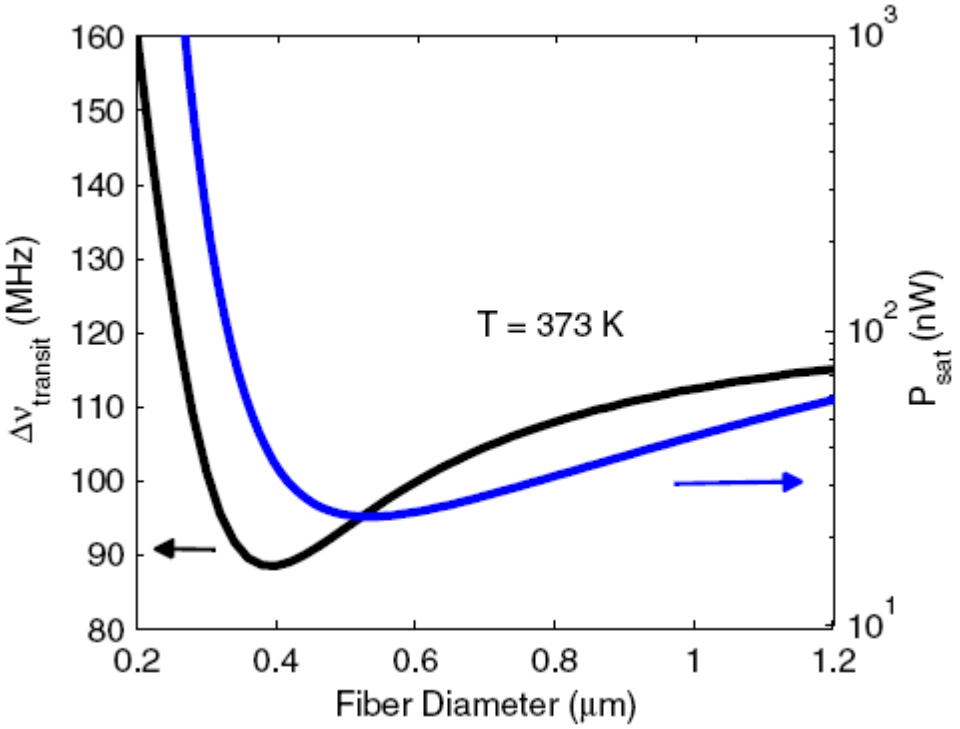

Figure 24.3: Transit time linewidth (black) and Saturation power (blue) versus fiber diameter

25.) Taper Fabrication

The tapered fibers are fabricated from Thorlabs 780HP single mode (at 780 nm) fiber. The first step is to strip a small section of acrylic coating off of the center of a fiber. The fiber is then place into two Newport magnetic fiber clips, which are firmly attached to two motor driven pulling stages. The stripped section is centered between the two pulling stages, directly over a hydrogen oxygen torch which is also fixed to a motion control stage. Using a program in MATLAB, the motion of the torch and pulling stages can be controlled directly by the computer. Once the torch is lit and the program is initiated, the two pulling stages move apart from one another as the torch moves back and forth under the stripped section. As the pulling stages move further apart from one another, the glass of the heated fiber melts and the fiber adiabatically reduces in diameter. This pulling continues until the diameter at the center of the fiber is approximately 500 nm.

During the tapering process, laser light may be coupled into the fiber, and a photo detector can be used to measure the transmission efficiency as the fiber is pulled. Several factors can influence the optical transmission such as flame size, pulling speed, and torch speed. Also, since the evanescent mode is guided in air outside the fiber, any dust that falls on the tapered section will dramatically reduce transmission. A high magnification camera is also used to watch the pulling process. When the fiber diameter is comparable to the wavelength of light, bands of color may be seen on the fiber due to interference effects, similar

to those seen on oil droplets. The variation of color over the length of the tapered section corresponds to variation in fiber diameter.

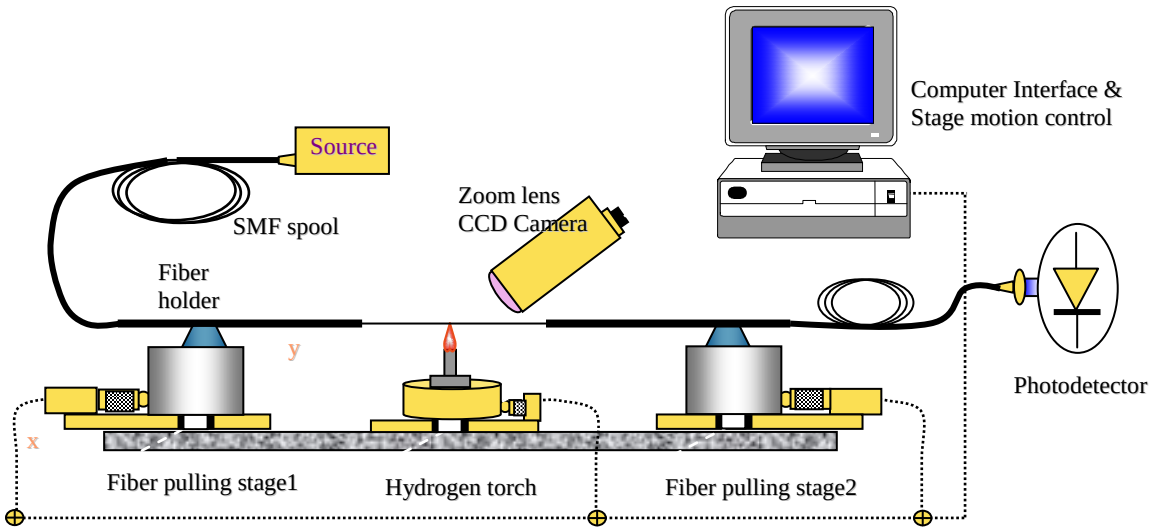

Figure 25.1: TNF fabrication apparatus

Below is a picture from a Scanning Electron Microscope of the tapered section of a TNF. Since there was no vibration isolation, the picture shows oscillations in the suspended fiber due to the mechanical pump used to evacuate the SEM. Nevertheless, we see that the diameter is approximately 400 nm.

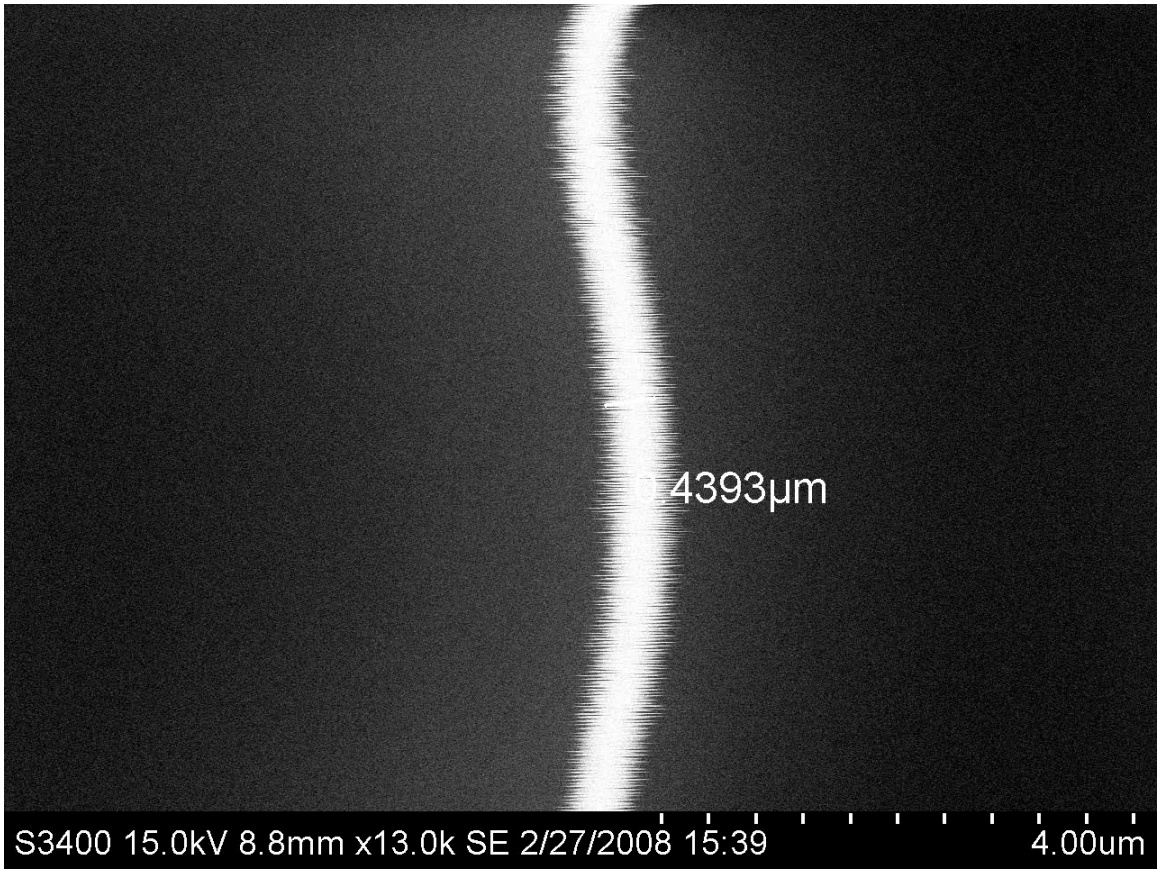

Figure 25.2: Image of tapered fiber taken from an SEM

26.) Installation in Vapor Cell

Switching in TNF has been proposed in atomic vapor as well as cold atoms. A separate apparatus was necessary for each method. The system for switching in vapor is illustrated below.

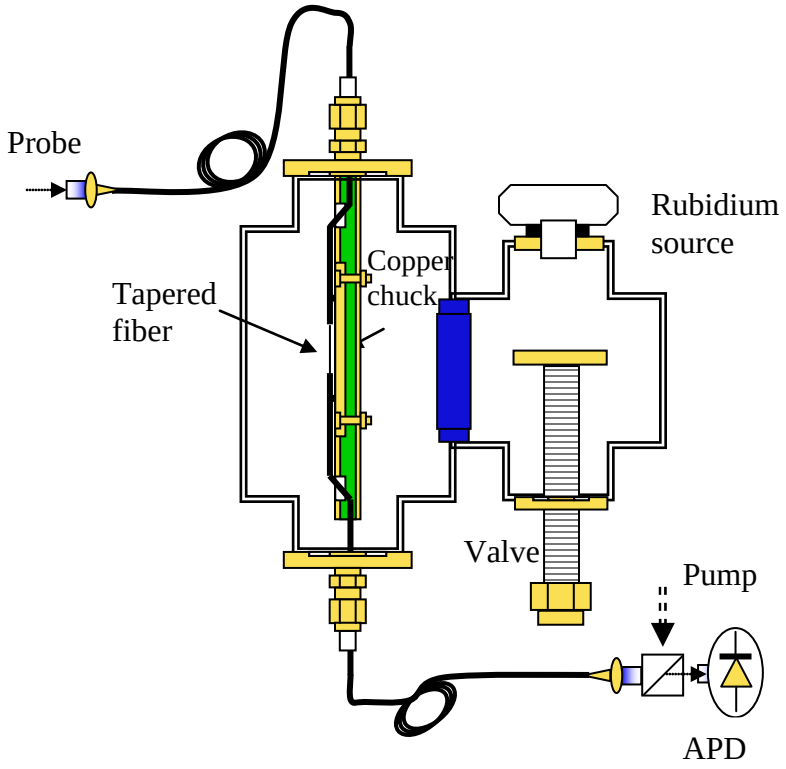

Figure 26.1: Rubidium vapor cell for TNF experiment

The vapor cell consists of two sections, one that houses the fiber and one that contains a Rb source. These sections are separated by a valve, and are continuously pumped by a mechanical pump to a pressure of 10 mT. The fiber is first attached to a custom made copper chuck using UV curable epoxy. The chuck is then inserted into the vapor cell from the top. Custom made Teflon ferrules [53] mounted into Swagelok connectors are drilled through the center with a number 80 drill bit so that the fiber slips through. When the Swagelok connector is tightened, the ferrules are forced down and compressed to form a tight seal around the input and output of the fiber in order to keep air out of the system.

To vaporize the Rb, the reservoir holding the Rb is heated to a temperature of $150^{o}\,C$. In order to minimize the amount of Rb condensing on the cell and the fiber both are heated to about $100^{o}\,C$. If Rb condenses on the fiber, transmission through the fiber will decrease.

Light may be coupled into the fiber, and monitored at the output with an APD. One experiment, discussed later, employs cross-polarized counter-propagating beams in the fiber achieved by coupling a probe into one end of the fiber, and a pump into the other end. A polarizing beam splitter is used to separate the beams, and send the probe beam to the APD.

27.) Installation in MOT

The second system was designed and built to allow for interaction between the TNF field and cold atoms. As stated earlier, cold atoms will not be affected by transit time broadening, and narrow EIT linewidths can be achieved even for small mode areas. For this reason cold atoms can be used for low light optical switching using the 4 level EIT scheme discussed earlier. For such a 4 level experiment to be implemented, the probe and switching beams would be sent through the TNF, while the pump would intersect the taper orthogonally, traveling in free space.

In order to insert a TNF into a MOT, two tools had to be designed and built. A custom made fiber chuck was necessary to hold the fiber, as well as a motion manipulation system needed for movement of the fiber in the UHV MOT chamber. The fiber chuck was designed to fit in between the MOT coils, and

holds the tapered section vertically in the trapping region so that it intersects the atom cloud. The chuck had to be carefully designed to fit around the atom cloud without clipping and scattering the MOT beams, the chirp cooling beams, the repump beams, or any of the experimental beams. The chuck is shown below.

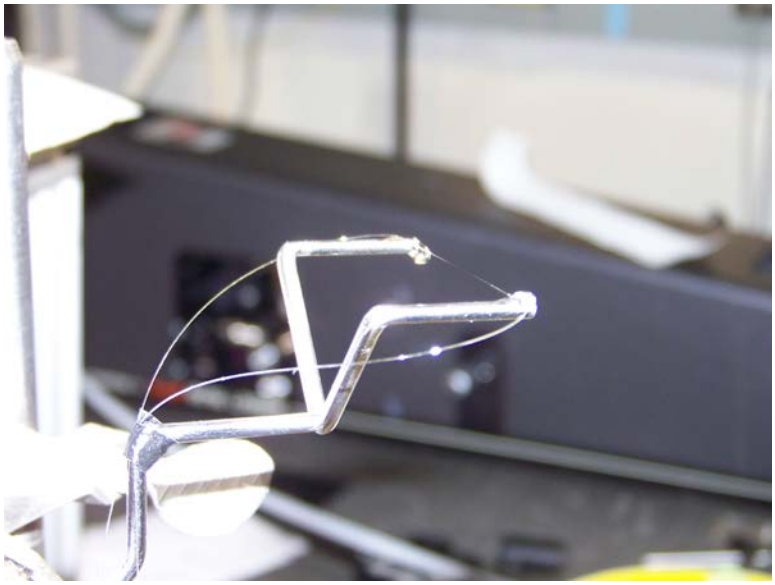

Figure 27.1: Photograph of fiber chuck and tapered section of TNF

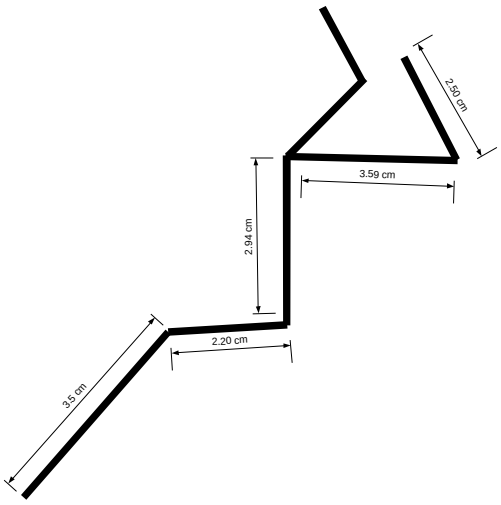

Figure 27.2: Schematic of fiber chuck

The conceptual design for the UHV fiber motion manipulation system is shown below.

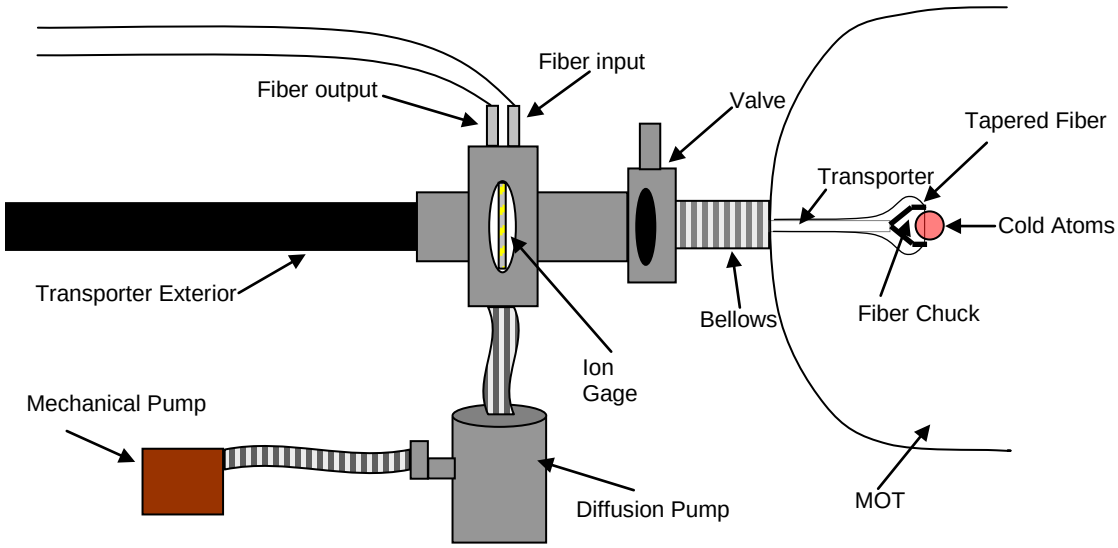

Figure 27.3: TNF linear transporting section

For linear translation, a magnetically coupled transporter from MDC was attached to a port on the MOT chamber with a line of sight to the trapping region. A custom made adapter was used to attach the fiber chuck to the end of the linear transporter with a set screw. A bellows was connected in between the linear transporter and chamber port to allow for angular manipulation. The fiber, held onto the chuck with UV curable epoxy, was run along the transporter rod and exited the system through a vacuum feedthrough, using the Swagelok Teflon ferrule as discussed earlier. To minimize fiber slack in the chamber, the fiber was taped to the transporter rod using vacuum compatible double sided tape. The section with the fiber feedthrough was also pumped with a mechanical pump/diffusion pump combination, and a small hole drilled into a double sided flange situated between the transporter and bellows, just large enough to fit around the rod and let the fiber through, allowed for differential pumping. A

glass envelope ionization gauge was used in this section to monitor the pressure, which was recorded to be 10^{-8} torr. A valve was used to separate the two sections so that each section could be isolated from the other. Using this system, the fiber could be moved and guided directly into the main MOT chamber, and directed into the center of the trapping region. Below is a photograph showing the TNF mounted in the trapping region.

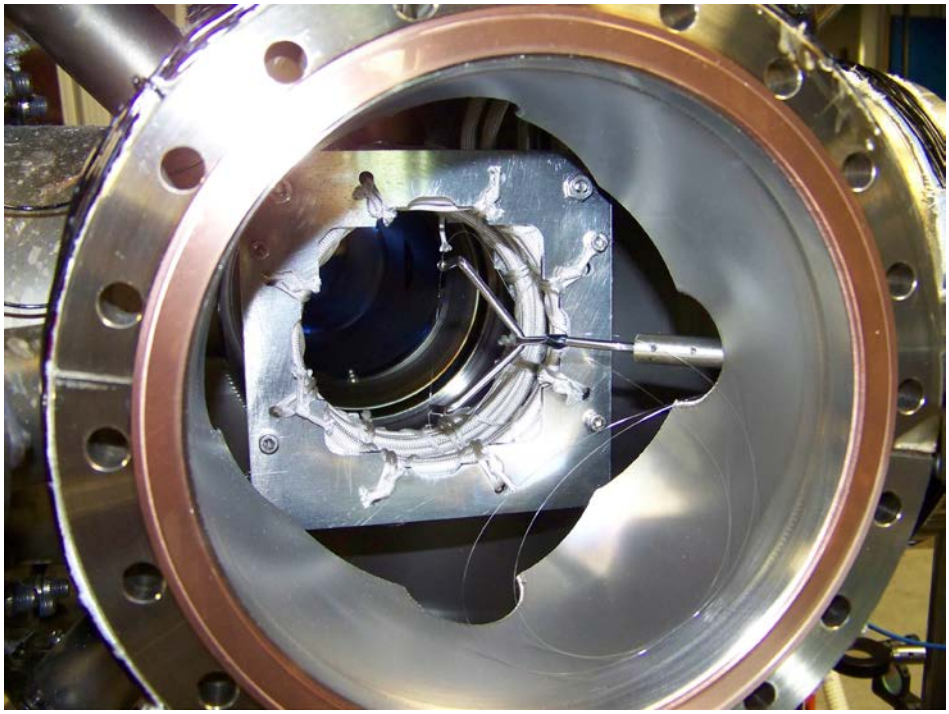

Figure 27.4: TNF inserted into MOT chamber

To align the TNF directly through the center of the atom cloud we use two cameras positioned orthogonally to one another to image the tapered fiber and MOT fluorescence. When the image of the fiber intersects the atom cloud on

both cameras, we know for sure that the fiber is passing through the MOT. For fine motion, current controlled shim coils on the MOT chamber can be tuned to displace the atom cloud by small amounts in all three dimensions. When the fiber enters the atom cloud, the density of the MOT is also decreased (evident by a decrease in MOT fluorescence) , however, absorption by a free space probe is still detectable as will be discussed later.

EXPERIMENTAL RESULTS

28.) Four Level Switch in a Rb Vapor Cell

We demonstrated the four-level all optical switching scheme in a vapor cell. The goal of this experiment was to show that we experience a shift of our EIT peak proportional to the power of the switching beam. As we have seen, this should be due to the fact that the light shift of the state coupling the second ground state and the excited state is of the order of $\frac{\Omega_{switch}^2}{4\delta_{34}}$ after the switching beam is applied. Assuming the frequency of the pump remains unchanged, our EIT condition is then only satisfied if the probe is shifted up in frequency by the amount of the light shift.

Since the excited hyperfine states of Rb 85 are not resolvable in a vapor cell, the three transitions used for our four level system were the two D2 transtions from $5S_{1/2}\ F=2 \rightarrow 5P_{3/2}$ and $5S_{1/2}\ F=3 \rightarrow 5P_{3/2}$ and the D1 transition from $5S_{1/2}\ F=3 \rightarrow 5P_{1/2}$. The energy diagram is shown below.

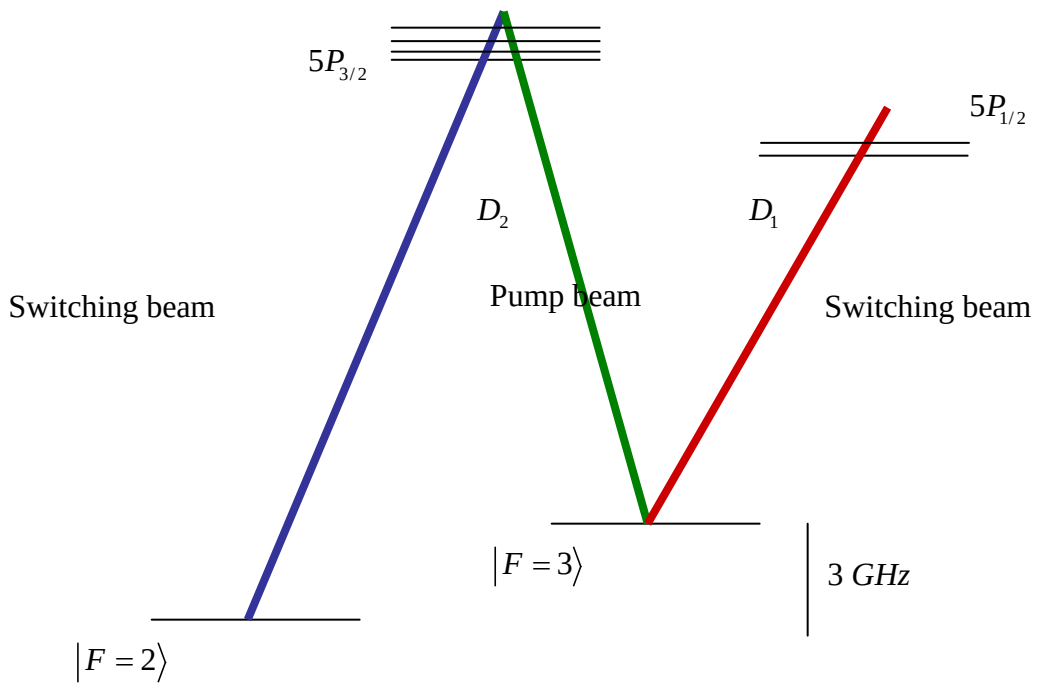

Figure 28.1: Energy level diagram for four level switching in vapor cell

Two different Argon pumped Ti: Sapphire lasers were used to produce the three beams necessary for the four level switching scheme.

First, the two beams which produce the EIT condition were derived from a Ti: Sapphire tuned to 780.24 nm. This produces a pump which is resonant for the $5S_{1/2}\ F=3 \rightarrow 5P_{3/2}$ transition. The exact frequency of the pump could be monitored by sending part of the beam into a saturated absorption setup. Another small part of the beam was split off to produce the EIT probe beam. This was achieved by sending part of the beam into a double pass AOM set for 1.51785 GHz to achieve the ground state splitting of 3.3057 GHz. Using a double pass AOM allowed us to eventually scan the probe without changing the exit angle of

the beam. Scanning was achieved by applying a DC voltage to the VCO added to a ramp produced by a function generator. Due to the polarization sensitivity of the high frequency AOM, a non-polarizing beam cube had to be used in the double pass instead of the conventional quarterwave plate and polarizing beam cube set up. This made diffraction very inefficient.

The pump and probe were then combined by a PBC and sent into a vapor cell, with density 10^{12} atoms per cm^3, heated to 88° C by bifilarly wound insulated nichrome wire. The measured powers of the probe and pump respectively were 610 μW and 3.15 mW. The vapor cell was surrounded by a mu-metal box to insulate the cell against stray magnetic fields which would cause Zeeman shifts and consequently reduce the efficiency of EIT. Another polarizing beam cube was positioned directly at the exit of the vapor cell to separate the pump from the probe beam, and a Thorlabs PDA-55 detector was set in the path of the probe. With the high frequency AOM, we could then scan the probe to see the EIT profile. This is shown below.

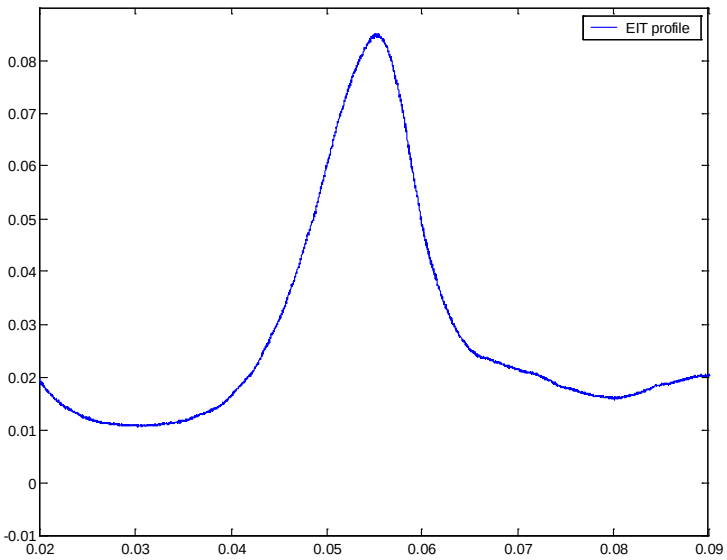

Figure 28.2: Free space EIT in observed in vapor cell

We found the EIT was most efficient when the pump beam and center frequency of the probe scan were upshifted 121 MHz from the $5S_{1/2}\ F=3 \rightarrow 5P_{3/2}\ F'=4$ transition as seen on the saturated absorption. We believe this is due to less absorption of our probe when detuned slightly away from atomic resonance.

The next step was to apply a switch beam and observe the shift in the EIT profile. This beam was derived from the second Ti: sapphire laser tuned to the D1 transition $5S_{1/2}\ F=3 \rightarrow 5P_{1/2}$ at 795 nm. This beam was sent in from another room via a Thorlabs single mode fiber, passed through a halfwave plate, and was combined with the pump by a NPBC. These beams could then combine with the probe at the PBC, and a halfwave plate was used to vary the amount of switching beam power. The complete apparatus is shown below.

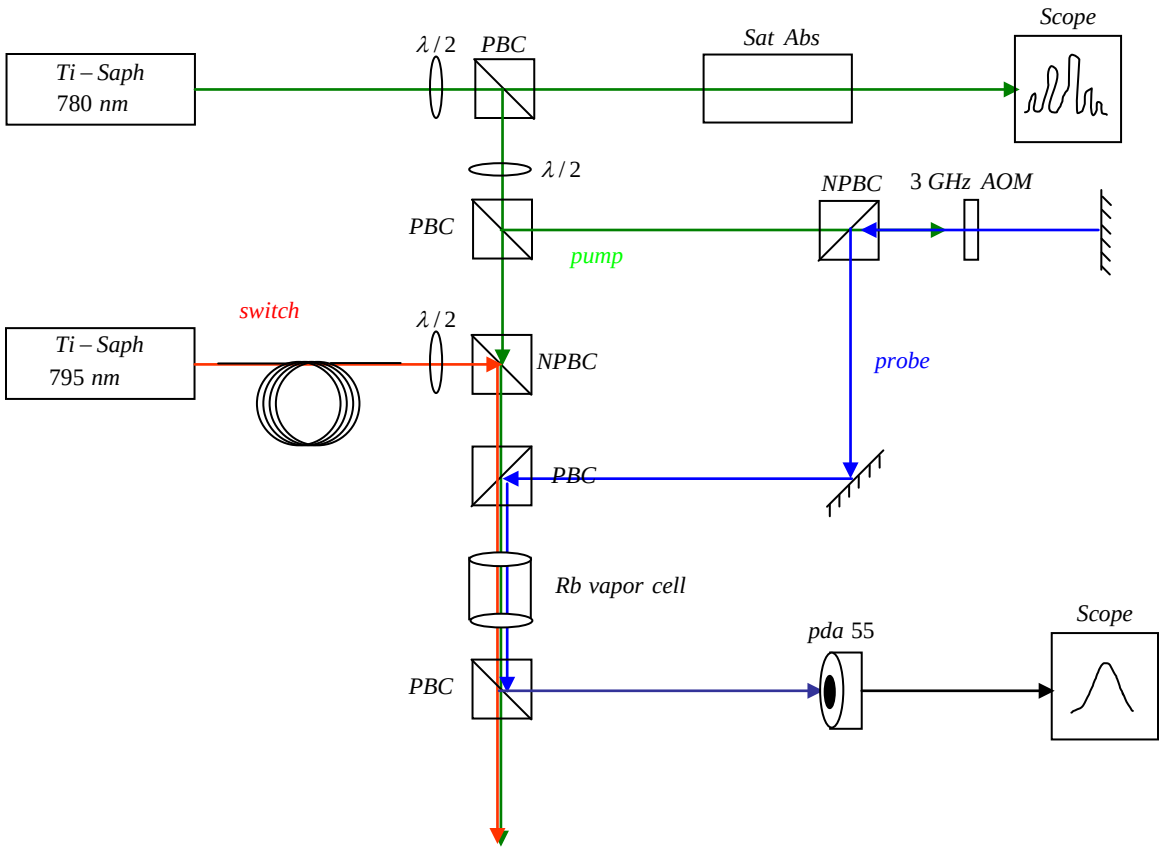

Figure 28.3: Apparatus for four level switching in vapor cell

When the power of the switch beam is varied, we expect to observe shifts of the EIT profile in our probe scan by an amount proportional to the light shift of the $5S_{1/2}$ $F = 3$ state. We measured the shifts induced by switch beam powers of 0 mW 3 mW, 6 mW, 12.6 mW and 18.6 mW. These individually scaled plots are all included on a single set of axes below and show the relative shifts associated with these powers.

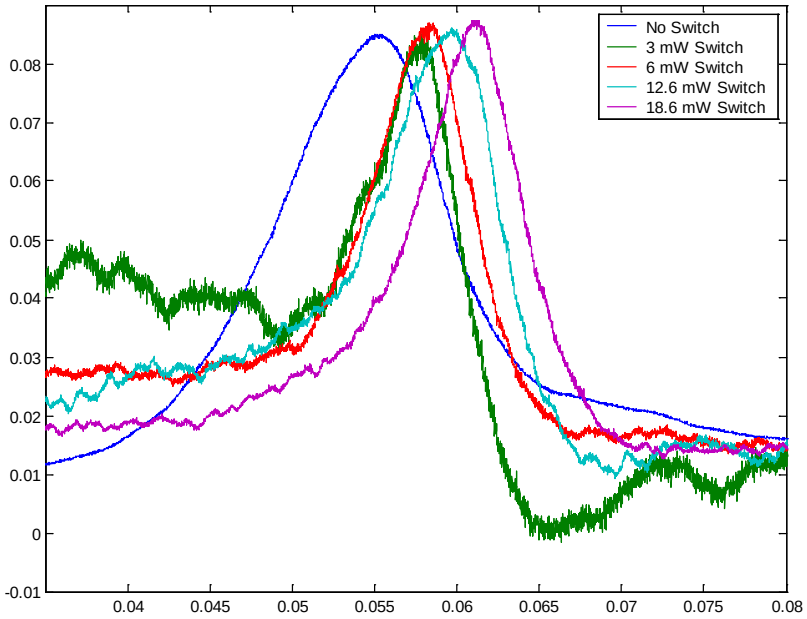

Figure 28.4: Four level light shift switching in vapor cell. Each trace shows a different value for switching intensity

We find that the EIT profile does shift in an amount proportional to the power in the switch beam, confirming the previously discussed 4 level system theory.

29.) V-type EIT switch in a Vapor Cell

This section discusses an experiment we performed in a vapor cell with free space beams. It uses the theory already developed in the V-type EIT switching section. The experimental apparatus is shown below.

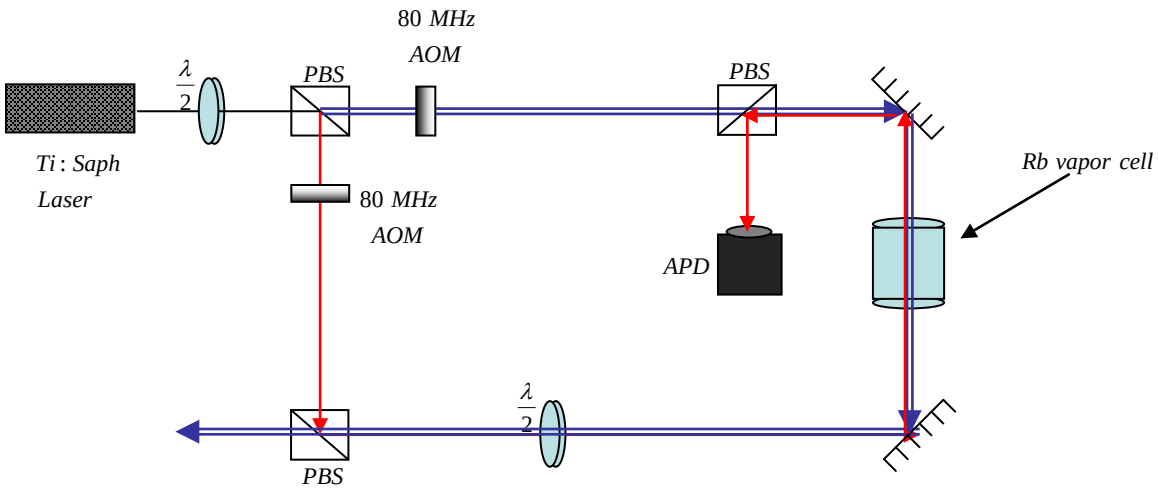

Figure 29.1 Apparatus for V-type EIT switching in vapor cell

We sent two linearly cross polarized counter-propagating beams in free space through a vapor cell. In the diagram above, the single red line represents a weak probe beam which is detected by an APD, whereas the double blue line represents the stronger pump beam. As the laser is scanned, we see the saturated absorption trace shown below.

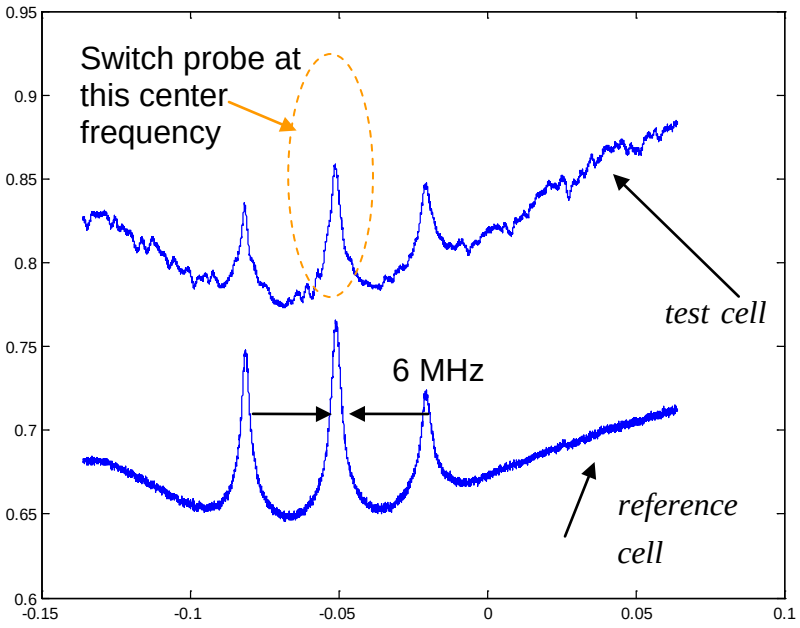

Figure 29.2: Saturated absorption using linearly cross polarized counter-propagating pump and probe in vapor cell (upper plot) and saturated absorption in reference cell (lower plot)

The laser was then locked to the frequency corresponding to the V-Type EIT peak, and the pump was pulsed. This caused an intensity modulation on the probe beam, shown below.

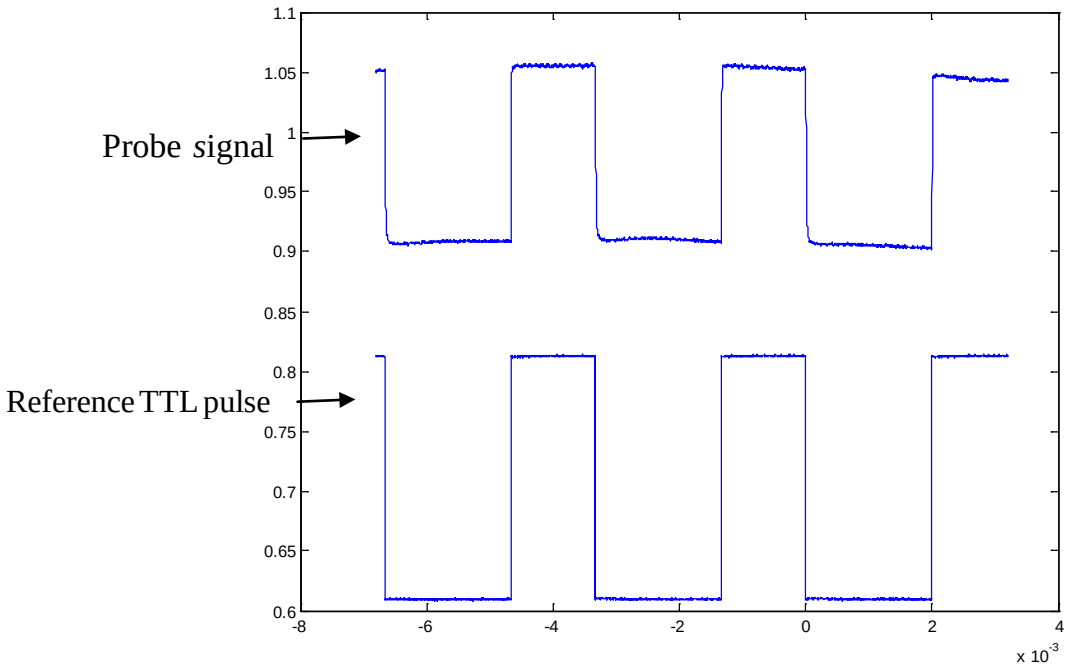

Figure 29.3: V-type EIT switching of probe in vapor cell (upper plot) and refernce TTL pulse for producing pump pulses (lower plot)

Due to the 6 MHz linewidth of the V-type EIT peak, the speed of this switch is limited. However, it illustrates the basic principle of light-shift switching.

30.) EIT Observed in a MOT

The following section describes experimental observations of Λ-type EIT in the MOT. In this experiment, a cross-polarized counter-propagating probe and pump are allowed to interact with the cold atoms. As discussed earlier, when the difference detuning between the pump and probe is zero, EIT condition is

established, and the atomic medium is transparent to the probe beam. This will result in transmission of the probe, and may be seen by directly measuring the probe output. Another way to detect EIT, however, is to measure the fluorescence of the MOT. If the difference detuning between the counter propagating pump and probe is nonzero, we know that the near-resonant pump and probe should be absorbed by the atoms, resulting in fluorescence. If the pump and probe difference detuning is zero, we would expect transmission of both beams, resulting in an a decrease in fluorescence.

The experimental apparatus is shown below.

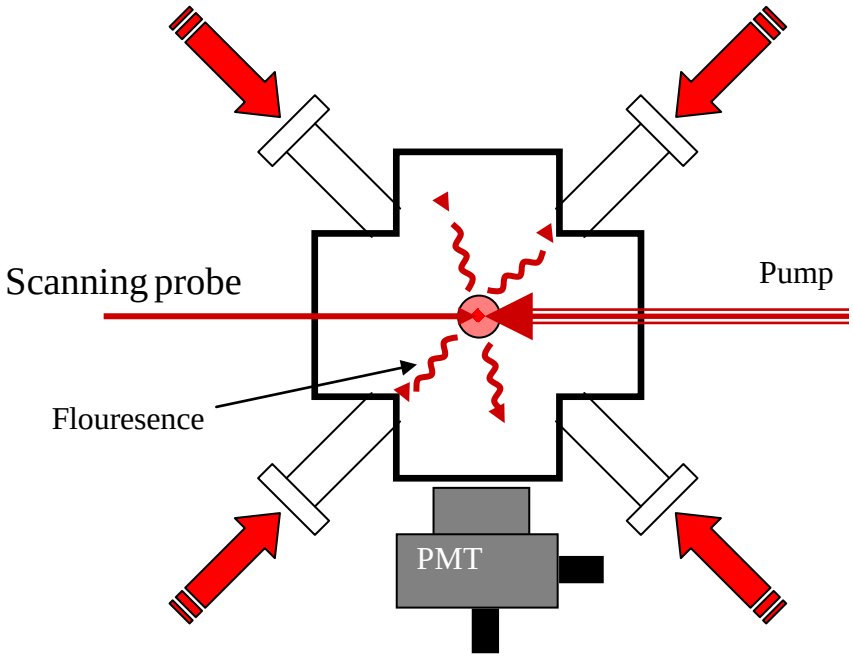

Figure 30.1: Apparatus for observing EIT in MOT by fluorescence

Two counter-propagating cross polarized beams are sent into the center of the MOT through opposite ports of the main chamber. A weaker probe is first sent through a nonpolarizing beam cube, and through a double pass AOM configuration. A 1.5 GHz Brimrose AOM was used, resulting in a double pass frequency of ~3 GHz, equal to the ground state splitting of Rb85. Typically for a double pass setup, a quarterwave plate is set between an AOM and a polarizing beam cube to allow all the light which is initially transmitted through the PBS to then be reflected by the PBS after the second pass through the AOM. The high frequency AOM, however, is polarization sensitive, diffracting more efficiently for horizontally polarized light. For this reason the nonpolarizing cube was used, resulting in a loss of 75% of the light. The beam is then sent through a halfwave plate and polarizing beam cube and into the MOT.

The probe beam was then aligned through the center of the trapping region while the trap was on. Using a ccd camera we could observe the fluorescence of the trap while aligning the beam. When a hole is seen to be knocked through the center of the trap fluorescence we know that the probe is aligned. The probe then passed through the other port, exiting the chamber. A stronger counter propagating pump beam was aligned in a similar way in order to overlap the probe. A water cooled PMT was positioned in a port having line of sight perpendicular to the beam paths in order to monitor weak fluorescence by the probe beam.

The frequencies of the probe and pump were chosen to create a λ system in Rb85. This was achieved by locking the pump beam on the $F = 2 \rightarrow F' = 3$

transition. Since the probe beam was up-shifted by the amount of the ground state splitting (3GHz), the probe was automatically locked to the $F = 3 \rightarrow F' = 3$ transition. For this experiment, however, it was necessary for the probe frequency to scan through this resonant frequency. This was achieved by adding a scanning signal from a function generator to the DC voltage supplied to the VCO controlling the AOM. A negative bias was added to the generator's ramp so that the resonant condition was centered in the frequency sweep.

The experiment proceeded in the following way. First the MOT beams and coils were switched on to allow the loading of the trap. The MOT beams and coils were then switched off for one millisecond while the pump and probe were simultaneously switched on. The function generator was also triggered at this point to scan the probe over a few EIT linewidths. All triggering and switching was controlled by a SRS DG535 pulse generator. The fluorescence of the probed atoms was collected by the PMT and is shown below.

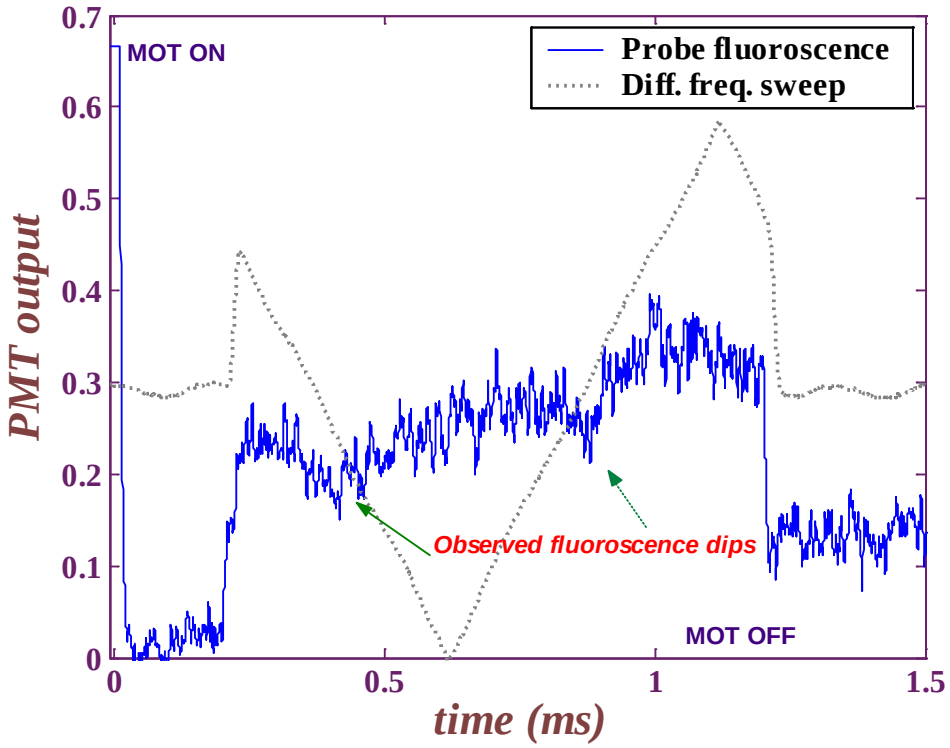

Figure 30.2: Observed EIT fluorescence dips in MOT

An averaged plot of the probe fluorescence is also shown below. The data was processed using a running average of 256 points.

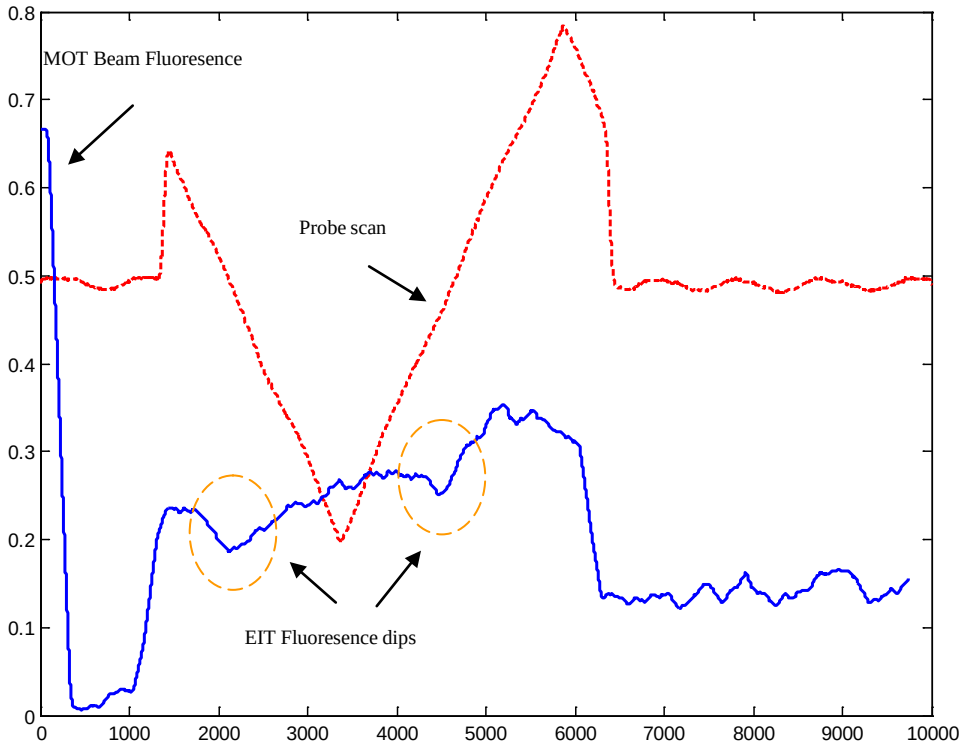

Figure 30.3: Observed EIT Fluorescence dips in MOT (running average over 256 points)

We find that at the center of the scan, when the probe is tuned to the $F = 3 \rightarrow F' = 3$ transition, and consequently when the difference detuning is zero, dips in the fluorescence spectrum are observed. This is the condition for EIT. As discussed earlier, these dips are the result of a decrease in fluorescence which accompanies pump/probe absorption. This result shows that our detection scheme, trap density, and scanning methods are sufficient to detect EIT in cold atoms. This is an extremely important step in implementing the four level

switching scheme in the MOT. Ongoing experiments will attempt to observe EIT in tapered nanofiber embedded in cold atoms.

31.) Free Space Absorption in MOT near Tapered Nano-fiber

For the four level switching experiment we wish to perform in the MOT, a tapered nano-fiber must be inserted into the middle of the trapping region. Putting a TNF into a cloud of cold atoms, however, raises a few concerns. For instance, the fiber will scatter the MOT beams and physically disrupt the trapping region. Also, the epoxy and fiber coating may outgas raising the pressure near the trapping region. These problems will in turn decrease the overall density of the atom cloud.

The following experiment was performed to measure the density of the trapped atoms using the fluorescence measurements discussed earlier. This time, however, the TNF was directly inserted into the center of the trap. To insert the fiber into the center of the MOT we used the previously discussed method of using two cameras orthogonally positioned pointing towards the center of the chamber. A vertical probe was aligned to run along the direction of the fiber through the atom cloud. A schematic of the experiment is shown below as well as the images from the two orthogonal cameras ensuring the TNF was centered through the atom cloud.

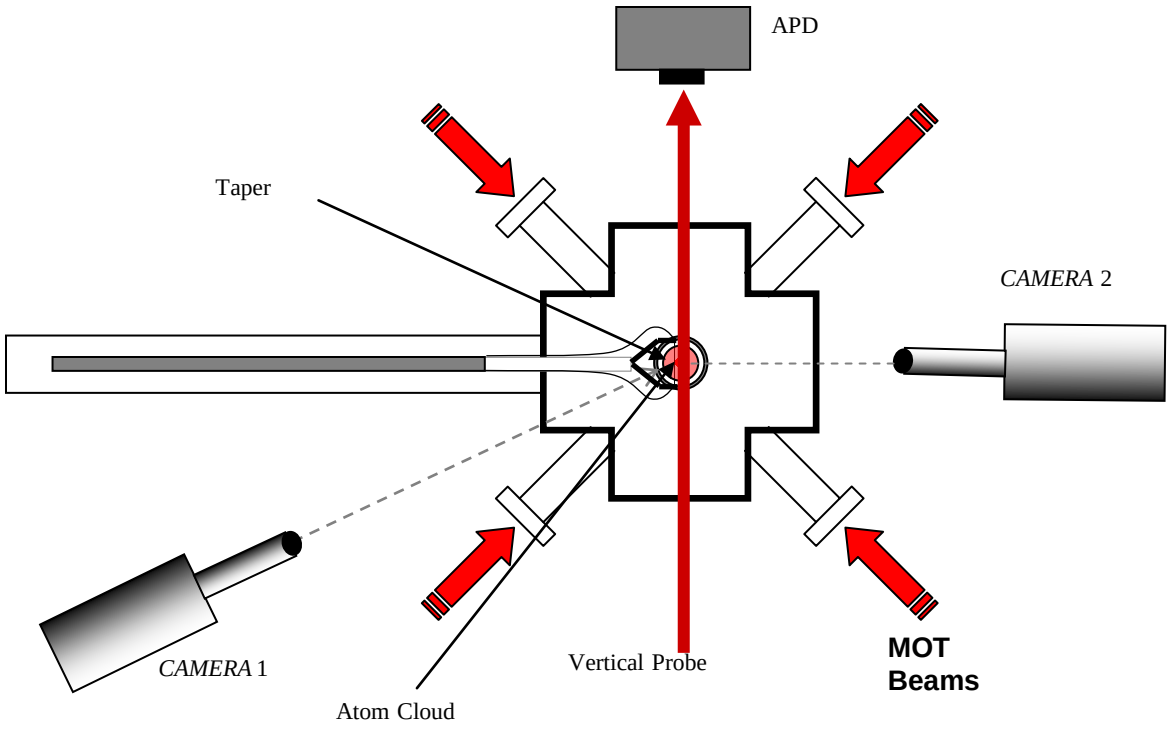

Figure 31.1: This illustrates how to image TNF in a MOT

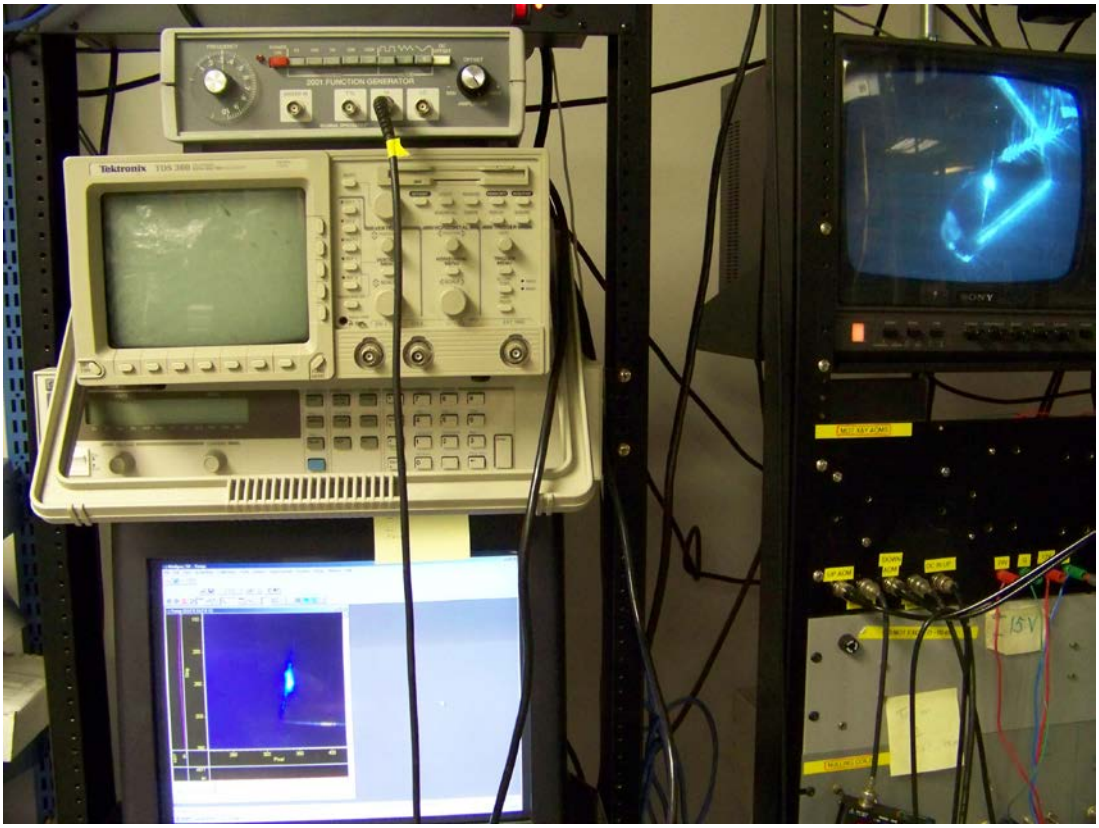

Figure 31.2: Images of the TNF in the MOT on two orthogonally placed cameras

As described earlier, the probe was pulsed on while the MOT beams were flashed off in order to detect the atoms . The probe intensity was detected by an APD with the MOT coils first switched on in order to detect the absorption by the atoms, and then switched off to compare the probe intensity with no atoms present. These results are shown below.

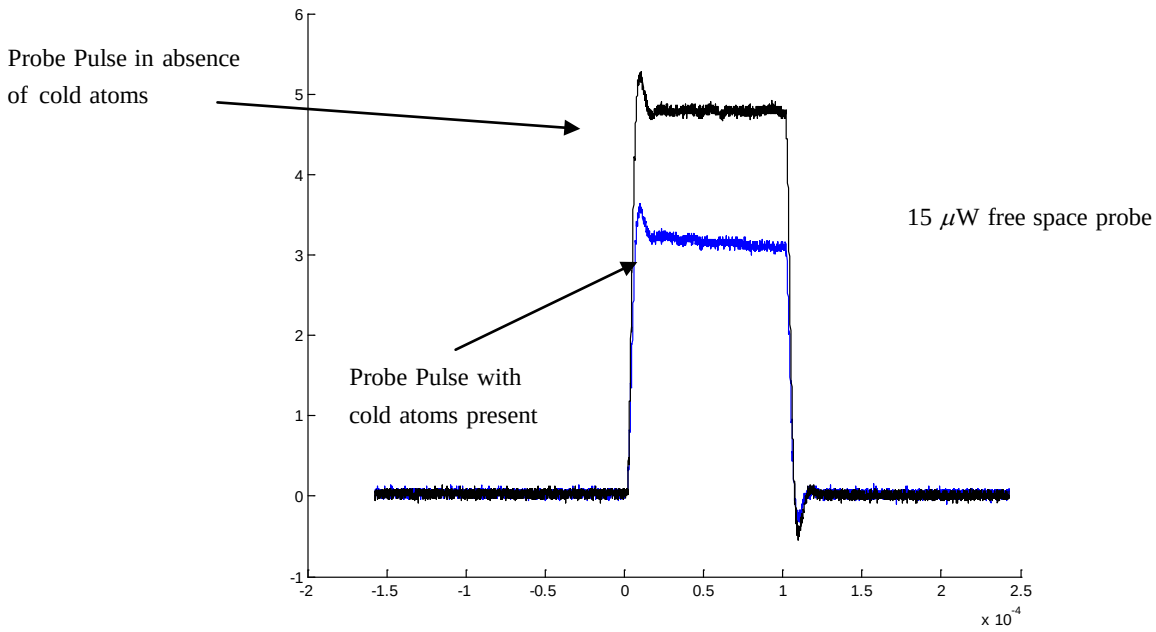

Figure 31.3: Probe absorption measurements in the MOT with the MOT coils off (black), and the MOT coils on (Blue)

We found that the density of the MOT was decreased by a factor of about two and a half compared to the density without the fiber, however a clear absorption signal is present. This provides signs of encouragement for observing absorption of the TNF guided mode.

32.) Saturated Absorption in a Tapered Nanofiber

The following section shows results of V-type EIT in a TNF and was published in PRL [ref]. A diagram of the experiment is shown below.

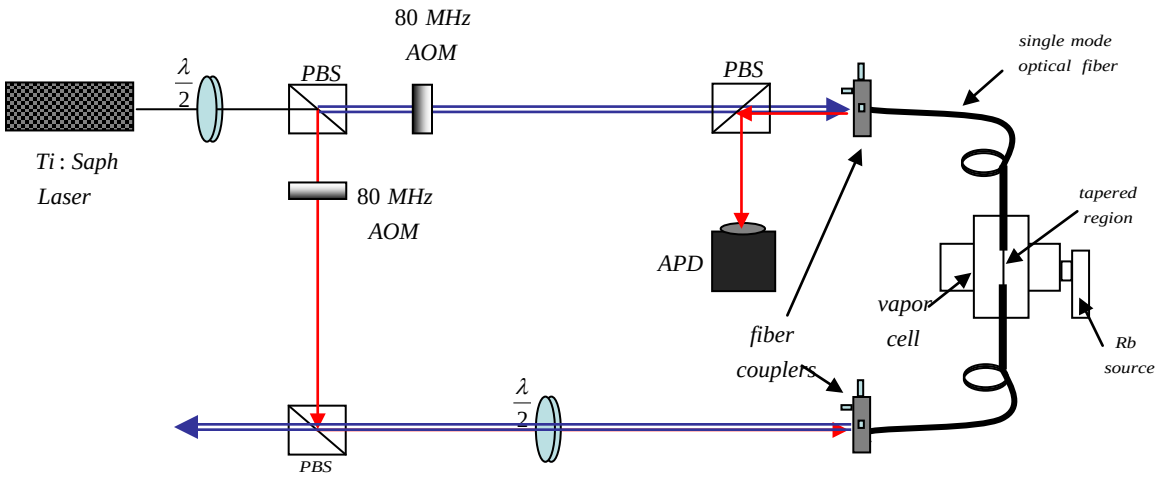

Figure 32.1: Apparatus for observing V-type EIT in a TNF embedded in an Rb vapor cell

In our experimental setup [illustrated above], a TNF was inserted into a chamber containing hot rubidium vapor, which contained a natural mixture of Rb85 and Rb87 isotopes. A Newport single-mode fiber at 780 nm was drawn adiabatically into a TNF with a waist diameter of approximately 400 nm using the "flame-brush" technique [54] with a hydrogen-air torch. The resulting taper profile

is nearly exponential with a 1=*e* length of ~3 mm. During the adiabatic tapering process, monitoring of fiber transmission showed negligible loss (ranging from 1%–10%) for final taper waist diameters of approximately 400 nm.

The TNF is mounted to a copper chuck using UV-curable epoxy and inserted into the vacuum chamber using a set of Teflon fiber feedthroughs [cornell ref.], which maintain fiber continuity into and out of the vacuum chamber. A gate valve isolates the optical fiber during loading or unloading from a rubidium metal source. During experiments, the vacuum chamber was heated to 100 C (to minimize Rb condensation), and Rb vapor was created by heating the source region to 200 C, with the chamber pressure maintained at 5 mTorr by a roughing pump. For these measurements, we made no attempt to prevent dephasing for atoms which struck the TNF. Assuming the vapor inside the chamber is at an average temperature of 100 C, the atomic density is estimated to be $6*10^{12}$ atoms /cm^3.

For the first set of experiments, a weak probe beam (approximately 10 nW) obtained from a Ti: sapphire laser was transmitted through the TNF, and the optical transmission was monitored with an avalanche photodiode. The frequency of the probe was scanned over the Doppler broadened spectrum of the *D*2 manifold. The graph below shows the transmission spectrum through the TNF (lower spectrum), and a reference Rb vapor cell kept at 100 C (upper spectrum).

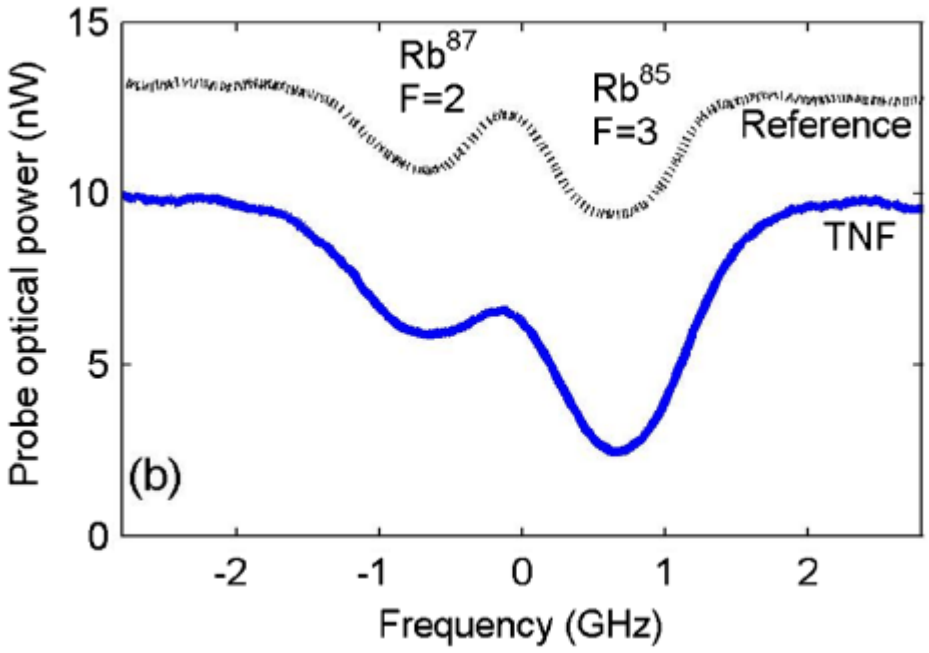

Figure 32.2: Linear absorption measured in a vapor embedded TNF (blue) and reference cell (black)

The dip on the left corresponds to the *F* =2 transitions in the *D*2 manifold of Rb87, while the dip on the right corresponds to the *F* =3 transitions in the same manifold of Rb85. Far away from resonance, the probe was found to be attenuated by about 20% due to a combination of losses at the input couplers and by TNF absorption. The data clearly show transmission dips representative of rubidium vapor absorption, with peak locations similar to that of the reference cell. However, the shape of the transmission dips for the Rb-TNF system is slightly different than that for the reference cell, which is due to both differences in Doppler broadening and transit time dephasing present in this experimental measurement.

...

A pump-probe measurement was performed, with the strong counter-propagating pump beam cross-polarized with respect to the probe. This measurement was performed on the *D*1 manifold in order to delineate more clearly the spectral features in the presence

of large transit-time broadening. The figure below illustrates the probe transmission spectrum (power ~1 nW) for counter-propagating pump powers of 10 nW (middle, green) and 30 nW (lower, red), for a TNF with a waist diameter of approximately 400 nm. For comparison, a reference trace is also shown for a conventional vapor cell (upper, blue).

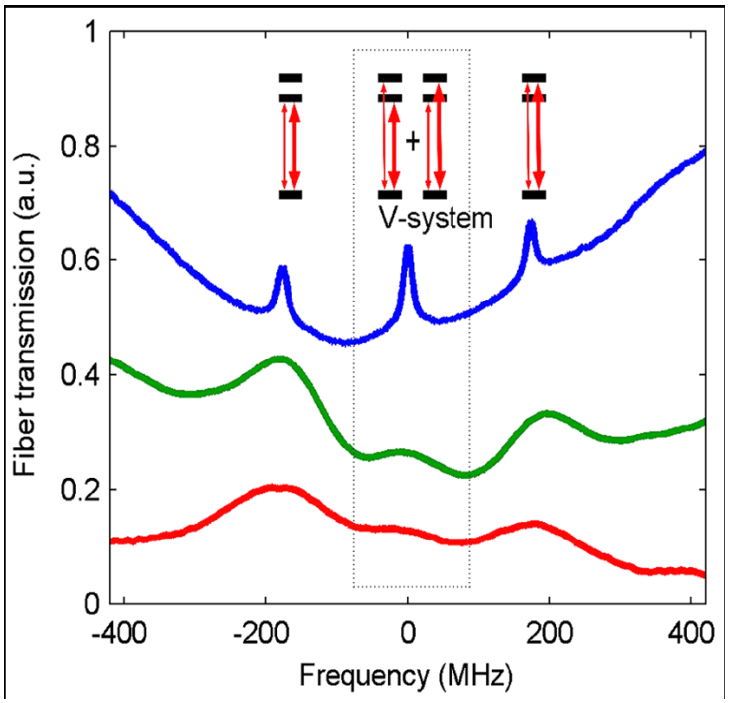

Figure 32.3: Saturated absorption observed in TNF with a probe power of 1 nW and a pump power of 10 nW (green) and 30 nW (red). Also plotted is saturated absorption in a reference cell (blue).

The peaks on the left and the right correspond to self-induced transparency (SIT) for Rb85 atoms with zero axial velocities, corresponding to the F =3 to F'= 2 and the F= 3 to F'= 3 hyperfine transitions, respectively. This measurement is similar to that of conventional saturated absorption spectroscopy, with a *V*-type

three level EIT peak (with orthogonally polarized pump and probe) located at the crossover resonance location.

This peak is composed of *V*-type EIT measurements of two groups of atoms: one with an axial velocity such that the probe excites the $F = 3$ to $F'=3$ transition and the pump excites the $F= 3$ to $F'=2$ transition, and the other with an equal but opposite axial velocity so that the probe excites the $F = 2$ to $F' =3$ transition and the pump excites the $F =3$ to $F'= 2$ transition. The EIT signal for the TNF is readily apparent for the lower pump power measurement, where the peak is clearly separated from the SIT peaks. The amplitude of this peak is measurably greater than the background signal for both the low and high power spectra, even though the high power spectrum is less resolvable due to power broadening.

For the conventional vapor cell, the transparency seen at the EIT resonance is larger than that at the SIT peaks due to the larger number of atoms in the combined 180 MHz Doppler-shifted groups (there is approximately 1.5 times the number of atoms in an isotropic vapor cell, which arises from the width of the Doppler distribution) than the individual zero axial velocity groups. Furthermore, the peak widths are the power-broadened individual hyperfine transitions (~6 MHz power broadened to ~18 MHz). However, for the TNF signal, there is a noticeable difference between the linewidths and relative amplitudes of the SIT and EIT peaks. Here, the line broadening for the lower (middle) power curve is due primarily to the transit-time effect. The transit-time broadening is about 110 MHz, close to the theoretical prediction. The dramatically smaller amplitude of the *V*-system EIT peak in the TNF measurement is likely due to a nonisotropic atomic velocity distribution in the Rb-TNF cell, which leads to a smaller population of atoms with the correct longitudinal Doppler shifted velocity component for the EIT interaction. The relative magnitude of the three absorption peaks is consistent with a 210 MHz wide effective

Doppler distribution. The effective reduction of the Doppler width may be attributable to the geometry of the cell and the relative position of the TNF and the vacuum pump. Further investigation will be carried out in the future to study this effect.

In conclusion, we have shown that a TNF coupled to a Rb vapor exhibits optical saturation and EIT at very low pump power levels below 10 nW, comparable to the best results in any Rb-waveguide system. Numerical modeling indicates that the TNF's small mode area results in a significant linewidth broadening due to the short transit time of hot Rb atoms through the evanescent field, which combined with Doppler broadening increases the threshold for nonlinear optical effects. However, this is a limitation of the large atomic velocities in a high temperature Rb vapor, which can be reduced in principle. In particular, the use of cooled atoms from a magneto-optic trap [55,56] will allow the elimination of transit time and Doppler broadening, which should lead to nonlinear interactions with pW level optical powers.

33.) Switching in a Tapered Nanofiber

The following section will show experimental results of fast microwatt all-optical switching in an atomic vapor embedded TNF. The switch discussed exploits the transit time and Doppler broadening to its advantage to increase switching bandwidth, at the expense of a slight increase in the switching beam power. The result expands upon previous observations of saturated absorption in a TNF in atomic vapor described above, using the same basic principle for switching.

The experimental apparatus for the experiment is identical to the experiment previously reported and is shown below.

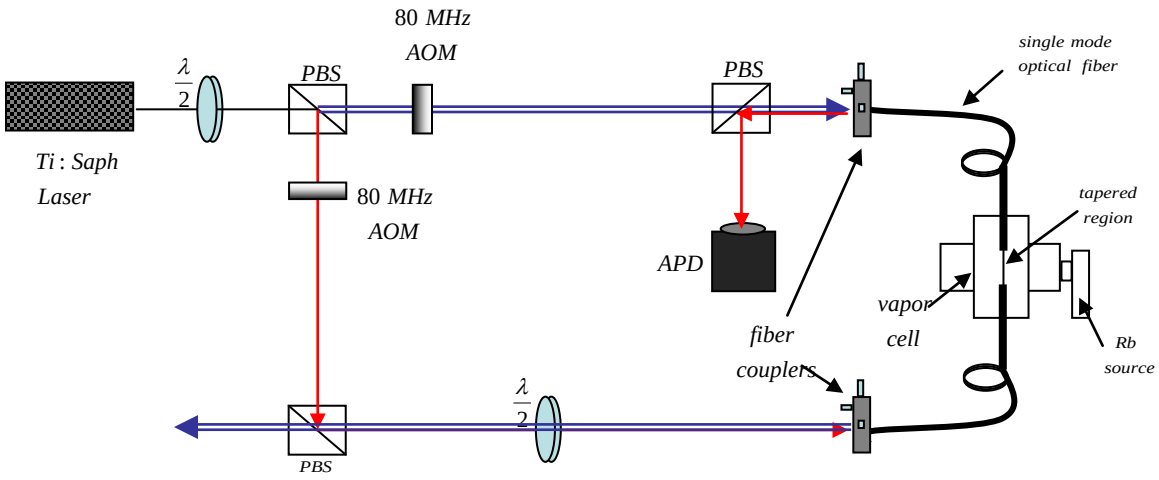

Figure 33.1: Apparatus for observing broadband switching in TNF

An input beam from an Argon pumped Ti: Sapphire laser is first split into a pump and probe by a PBS, and these are sent through 80 MHz AOMs to allow for switching. A half wave plate positioned before the PBS is used to adjust the relative powers between the two beams. The orthogonally polarized beams traverse separate paths and are sent through another set of polarizing beam cubes. Due to their relative polarizations, the probe is reflected off the PBS whereas the pump transmits through the PBS. The beams are sent into the tapered fiber from separate ports, counter-propagating as they interact with

rubidium vapor within the cell. The beams then exit from opposite ports, and take separate paths through the respective beam splitters. The probe is reflected into an APD so that its intensity may be measured as a function of frequency.

We find that as the fiber is heated within the cell (to prevent rubidium condensation) the probe field, within the fiber, experiences temperature dependent polarization rotation. For this reason another halfwave plate is positioned before the fiber coupler to ensure the probe is reflected into the APD.

With the pump blocked, the Ti: Sapphire is scanned and the 100 nW probe is monitored by the APD. The evanescent mode of the probe is allowed to interact with Rubidium vapor within the hot cell, and a linear absorption intensity profile is measured at the output of the fiber. This absorption profile has a line width on the order of a GHz, and is shown below in figure 33.2 as the red curve.

As discussed earlier, a counter propagating pump can be used to resolve megahertz wide hyperfine transitions by saturating the zero velocity group atoms. As the pump power is increased above saturation intensity, section 10 shows that power broadening may become significant. More atoms within the Doppler profile may be saturated, widening the saturated absorption peak. Furthermore, it was shown that for $\Omega \approx 100\Gamma$, corresponding to $I \approx 10,000 I_{sat}$, the entire Doppler profile would be depleted by the pump, creating a medium which is transparent to a probe pulse with GHz bandwidth. We have also seen that the V-type EIT light shift effect can induce transparency over the entire Doppler profile with sufficient pump power as well. In general both processes will occur.

To detect the transparency induced by the pump, we unblocked the 10 μW pump beam and allowed it to counter-propagate through the TNF relative to the probe. By scanning the Ti: sapphire laser, and monitoring the probe intensity as a function of frequency, this induced transparency can be directly observed. The transmission of the probe is shown below in figure 33.2 as the black curve. We find that within one Doppler profile we obtain almost 50% transmission. The noise seen on this trace was due to interference effects between the probe and back reflections of the pump off of the fiber coupler. A background intensity due to these stray reflections of the pump was subtracted from the probe transmission data in order to generate the plot shown.

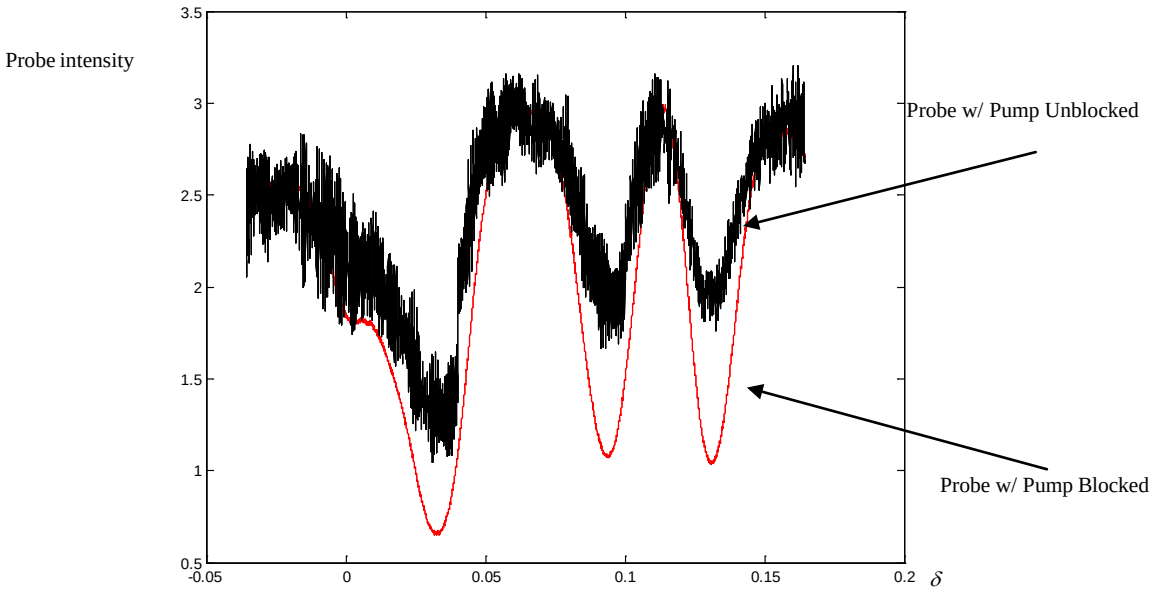

Figure 33.2: Linear absorption of probe observed in TNF over D1 spectrum with pump beam blocked (red) and with pump beam unblocked (black)

To demonstrate switching, the 100 nW, CW probe was held fixed at a frequency centered within the Doppler profile. The 10 microwatt counter propagating pump (derived from the same laser and tuned to the same frequency) is pulsed, and the probe output is monitored by the APD. We expect probe transmission when the pump is pulsed on, and probe absorption when the pump is absent. Results from the experiment below show the switching of the probe and the control signal of the pump for reference. We observed microwatt switching with pump pulses as short as .025 ms with repetition rates up to 10 kHz. Switching speeds were limited by the modulation bandwidth of the AOM, and detection of the switching was limited by the slow response time of the APD used.

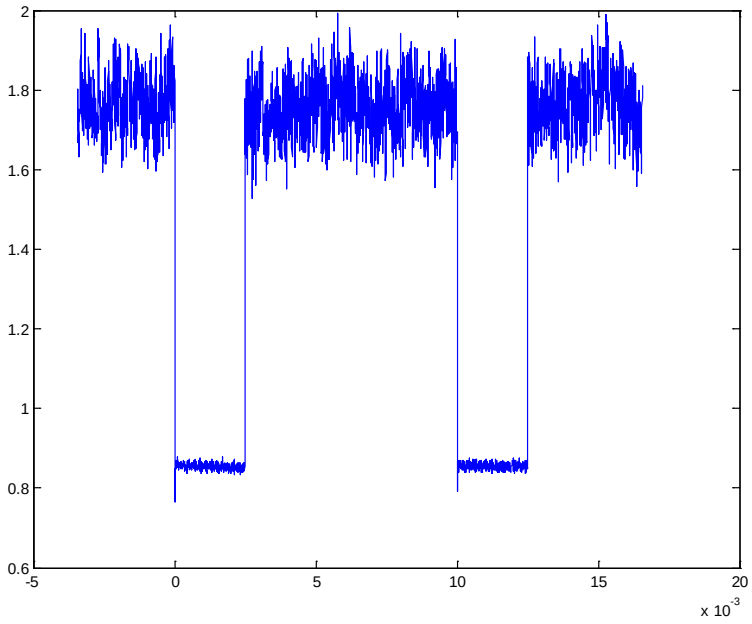

Figure 33.3: Probe switching at 100 Hz, 2.5 ms pulse length

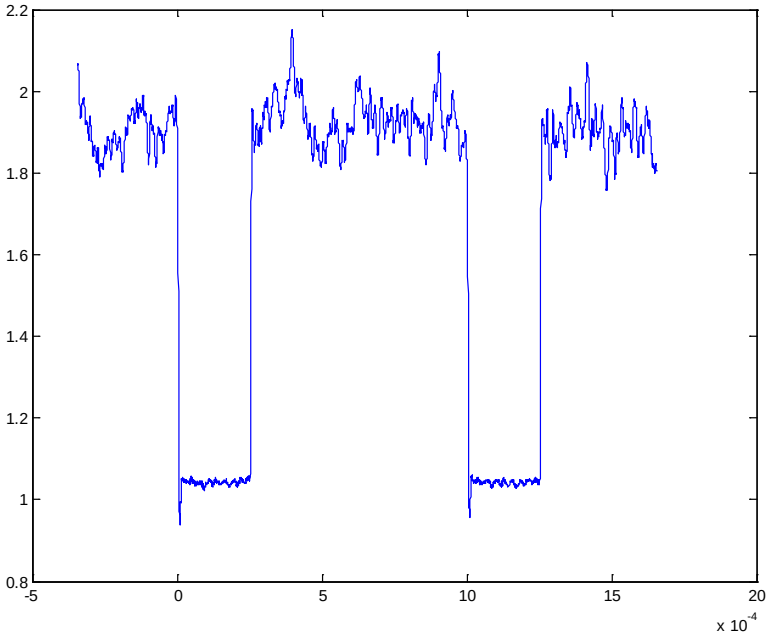

Figure 33.4: Probe switching at 1 kHz, .25 ms pulse length

Ongoing experiments involve the use of EOMs for faster pump intensity modulation as well as side band detection methods and higher speed detectors to measure faster switching speeds.

The concepts demonstrated by this experiment show that TNF may be used for fast switching. For the typical absorption width due to Doppler and transit time broadening of approximately 1 GHz, it follows that nanosecond probe pulses may be switched at GHz rates using all optical switching at microwatt switching beam powers.

CONCLUSIONS AND FUTURE WORK

Tapered nano-fibers and optical resonators have shown themselves to be promising technologies in the implementation of efficient all-optical switching. We have developed methods for inserting TNF into atomic vapor as well as into cold atoms in order to build various types of switches. We have reported low-power saturated absorption in the tapered nano-fiber, and done proof-of-principle light-shift switching experiments with freespace beams in a vapor cell. We have observed saturated absorption and broadband microwatt light-shift switching in a TNF embedded in a Rubidium vapor cell. Detection of high speed switching, however, was limited by the bandwidth of the APD used. High speed pulse production was also limited, by the bandwidth of the AOM used for pulsing. Ongoing experiments will make use of higher speed detectors, as well as an EOM for high speed pump intensity modulation.

We have seen evidence of EIT in a MOT using freespace beams. The next experimental goal for the TNF-MOT experiment is to observe absorption of the TNF guided mode by the cold atoms. Since the density of atoms in the trap is much less than that in vapor, fewer absorption events will occur for a given probe power in the MOT than in the vapor cell. For this reason, to observe complete absorption in the MOT, much lower probe powers (tens of photons) must be used. This will necessitate a more sophisticated detection system consisting of a photon counter rather than the APD used for the vapor experiments.

After TNF guided absorption is observed in the MOT, the next step would be to implement the four level switching scheme. This would first consist of setting up the EIT condition using the weak TNF guided mode as a probe, and a stronger free space beam as the pump. A weak switching beam would then be

sent through the TNF, counter-propagating to the probe, in a configuration similar to that of the four-level switch demonstrated in the vapor cell. With the switching beam present, the EIT condition would then be destroyed and the weak probe would be absorbed, as described in section 12 above.

We have also developed the tools for four level-switching in an optical resonator, including the dual-traveling wave cavity, moving molasses, atomic fountain, the FORT, coil design, and the experimental beams necessary for switching. These tools can be used for a variety of different cavity experiments in the MOT.

In all of these experiments, intense field strengths are achieved with low input power. By increasing the field strength we increase the strength of interactions between light and matter. This makes for efficient switches useful in a range of applications. We have demonstrated several different types of all-optical switches in atomic media, some appropriate for high bandwidth applications, and some which serve as proofs of principle for low photon number switching.

REFERENCES

[1] A. M. C. Dawes, L. Illing, S. M. Clark, D. J. Gauthier, "All-Optical Switching in Rubidium Vapor," Science, **308**, 672 (2005)

[2] A. Melloni, M. Chinello, and M. Martinelli, "All-Optical Switching in Phase-Shifted Fiber Bragg Grating" IEEE Photonics Technology Letters, **12,** 42 (2000)

[3] X. Hu, P. Jiang, C. Ding, H. Yang, Q. Gong, "Picosecond and low-power all-optical switching based on an organic photonic-bandgap microcavity", Nat. Photon, **2**, 185 (2008)

[4] A. M. C. Dawes, L. Illing, S. M. Clark and D. J. Gauthier, "All-Optical Switch Controls Strong Beams with Weak Ones," OPN, Dec. 2005, p 24, (2005)

[5] D. J. Griffiths, *Introduction to Quantum Mechanics,* Benjamin Cummings, London, 2004

[6] L. Allen and J. H. Eberly, *Opticla Resonance and Two-Level Atoms,* Dover, New York, NY, 1975

[7] R. Shankar, *Principles of Quantum Mechanics,* Springer, New York, 1994

[8] A. Yariv, *Quantum Electronics,* Wiley, Hoboken, NJ, 1989

[9] M.S. Shahriar, P. Pradhan, G.S. Pati, and K. Salit, "Light-Shift Imbalance Induced Blockade of Collective Excitations Beyond the Lowest Order," Optics Communications, **278** (2007), 94-98.

[10] M.S. Shahriar, G.S. Pati, and K. Salit ,"Quantum Communication and Computing With Atomic Ensembles Using Light-Shift Imbalance Induced Blockade," Physical Review A **75** (2): Art. No. 022323 FEB 2007.

[11] E. Hecht, *Optics,* Addison Wesley, London, 1997

[12] "Demonstration of a Tunable-Bandwidth White Light Interferometer using Anomalous Dispersion in Atomic Vapor," G.S. Pati, M. Messal, K. Salit, and M.S. Shahriar, Phys. Rev. Lett. **99**, 133601 (2007).

[13] "Demonstration of Tunable Displacement-Measurement-Sensitivity using Variable Group Index in a Ring Resonator," G.S. Pati, M. Messal, K. Salit, and M.S. Shahriar, Optics Communications (2008), Accepted/In-Press.

[14] M. Salit, G.S. Pati, K. Salit, and M.S. Shahriar, "Fast-Light for Astrophysics: Super-sensitive Gyroscopes And Gravitational Wave Detectors," Journal of Modern Optics, **54** 2425 - 2440.

[15] S. E. Harris, "Electromagnetically Induced Transparency" Phys. Today **50**, No. 7, 36 (1997).

[16] M. Fleischhauer, A. Imamoglu, and J. P. Marangos, “Electromagnetically induced transparency: Optics in coherent media,” Rev. Mod. Phys. **77**, 633 (2005).
[17] B. Kaltenhauser, H. Kubler, A. Chromik, J. Stuhler, T. Pfau, and A. Imamoglu, "Narrow bandwidth electromagnetically induced transparency in optically trapped atoms," J. Phys. B: At. Mol. Opt. Phys. **40**, 1907, (2007)

[18] J. P. Marangos, "Topical Review: Electromagnetically Induced Transparency," Journal of Modern Optics, 45, 471 (1998)

[19] G.S. Pati, K. Salit, and M.S. Shahriar, “Experimental Observation Raman Ramsey Fringes using Time Delayed Optical Pulses in Rubidium vapor,” Optics Communications (2008)

[20] L. V. Hau, S. E. Harris, Zachary Dutton,C. H. Behroozi, "Light speed reduction to 17 metres per second in an ultracold atomic gas," Nature **397**, 594, (1999)

[21] R. Tripathi, G.S. Pati, M. Messall, K. Salit and M.S. Shahriar, “Experimental constraints of using slow-light in sodium vapor for light-drag enhanced relative rotation sensing,” Optics Communications. **266**, (2006) 604-608.

[22] "Ultrahigh Precision Absolute and Relative Rotation Sensing using Fast and Slow Light", M.S. Shahriar, G.S. Pati, R. Tripathi, V. Gopal, M. Messall and K. Salit, Physical Review A **75** (5): Art. No. 053807 MAY 2007
[23] D.A. Steck, "Rubidium 87 D Line Data," http://steck.us/alkalidata/

[24] Alan Corney, *Atomic and Laser Spectroscopy*, Oxford University Press, USA, 1977

[25] M.E. Rose, *Elementary Theory of Angular Momentum*, Dover, New York, 1995
[26] E.U. Condon and H. Odabasi, *Atomic Structure*, Cambridge University Press, Cambridge, 1980
[27] H. Metcalf, and P. Ver der Straten,, *Laser Cooling and Trapping*, Springer, New York, 1999

[28] W.D. Phillips, “Laser Cooling and Trapping of Neutral Atoms,” Proceedings of the International School of Physics, Italian Physical Society, North Holland 1992
[29] A. Ashkin, “Acceleration and trapping of particles by radiation pressure”, Phys. Rev. Lett. **24,** 156 (1970)

[30] E. L. Raab, M. Prentiss, Alex Cable, Steven Chu , and D. E. Pritchard, “Trapping of Neutral Sodium Atoms with Radiation Pressure” Phys. Rev. Lett. **59**, 2631 - 2634 (1987)

[31] C. Cohen-Tannoudji, "Manipulating atoms with photons" **T76** 33 *Phys. Scr.* (1998)

[32] P. Meyster and M. Sargent *Elements of Quantum Optics*, Springer-Verlag, Berlin, 1991

[33] S. M. Spillane, G. S. Pati, K. Salit, M. Hall, P. Kumar, R. G. Beausoleil, and M. S. Shahriar, “Observation of Nonlinear Optical Interactions of Ultralow Levels of Light in a

Tapered Optical Nanofiber Embedded in a Hot Rubidium Vapor," Phys. Rev. Lett. **100**, 233602 (2008)

[34] M. D. Lukin, and A. Imamog , "Controlling photons using electromagnetically induced transparency," Nature, **413**, 273 (2001)

[35] Y. Chen, G. Pan, and I. A. Yu, "Transient behaviors of photon switching by quantum interference," Physical Review A, **69**, 063801 (2004)

[36] Y. Chen, Y. Liao, H. Chiu, J. Su, I.A. Yu, "Observation of the quantum interference phenomenon induced by interacting dark resonances," Physical Review A, **64**, 053806 (2004)

[37] H. Kang, G. Hernandez, J. Zhang and Y. Zhu, "Phase controlled light switching at low power levels" http://arxiv.org/ftp/quant-ph/papers/0510/0510036.pdf

[38] S.E. Harris and Y. Yamamoto, "Photon Switching by Quantum Interference," Phys. Rev. Lett. **81**, 3611 (1998)

[39] M. Yan, E.G. Rickey, Y. Zhu, "Observation of absorptive photon switching by quantum interference" Phys Rev. A, **64**, 041801(R) (2001)

[40] D.A. Braje, V. Balick, G.Y. Yin, S.E. Harris, Phys. Rev. A, "Low-light-level nonlinear optics with slow light" **68**, 041801 (R) (2003)

[41] Y.F. Chen, Z.H. Tsai, Y.C. Liu, and I.A. Yu, "Low-light-level photon switching by quantum interference" Opt. Lett. **30**, 3207 (2005)

[42] K. Szymaniec, H. J. Davies and C. S. Adams, "An atomic fountain guided by a far-off resonance laser beam", Europhys. Lett, 45 (4), pp. 450-455 (1999)

[43] M. D. Lukin, "Trapping and manipulating photon states in atomic ensembles" Rev. Mod. Phys. **75**, 457 (2003).

[44] B.E.A. Saleh and M.C. Tech, *Fundamentals of photonics,* Wiley, New York 1991
[45] A. Siegman,, *Lasers*, University Science Books, Mill Valley, CA, 1986

[46] G. Brambilla, V. Finazzi, D.J. and Richardson, "Ultra-low-loss optical fiber nanotapers," Optics Express **12**, 2263 (2004)

[47] Fam Le Kien, V. I. Balykin, and K. Hakuta, "Scattering of an evanescent light field by a single cesium atom near a nanofiber" Physical Review A **73,** 013819 (2006)

[48] Fam Le Kien,V. I. Balykin, and K. Hakuta, "Light-induced force and torque on an atom outside a nanofiber" Physical Review A **74**, 033412 (2006)

[49] J.A. Buck, *Fundamentals of Optical Fibers,* Wiley, New York, 1995
[50] J. Bures and R. Ghosh., "Power density of the evanescent field in the vicinity of a tapered fiber" J.Opt.Soc.Am.A, **16**, 1992 (1999)

[51] P.N. Moar, S. T. Huntington, J.Katsifolis, L.W.Cahill, K.A.Nugent and A.Roberts, *Near Field Modelling and Measurement of Tapered Optical Fibre Devices,* LEOS 1997 - Ca, U.S.A, http://ieeexplore.ieee.org/iel3/4988/14076/00645237.pdf

[52] P.N. Moar , S.T. Huntington, J. Katsifolis, L.W. Cahill, A.Roberts, and K. A. Nugent "Fabrication, modeling, and direct evanescent field measurement of tapered optical fiber sensors" Journal of Applied Physics, **85**, 3395 (1999)

[53] E. R. I. Abraham and E. A. Cornell, "Teflon Feedthrough for Coupling Optical Fibers Into Ultrahigh Vacuum Systems," Appl. Opt. **37**, 1762-1763 (1998)

[54] T. A. Birks and Y. W. Li, "The shape of fiber tapers," J. Lightwave Technol. **10**, 432 (1992).

[55] K. P. Nayak, P. N. Melentiev, M. Morinaga, Fam Le Kien, V. I. Balykin, and K. Hakuta, "Optical nanofiber as an efficient tool for manipulating and probing atomic fluorescence." Optics Express **15.** 5431 (2007)

[56] G. Sague, E. Vetsch, W. Alt, D. Meschede and A. Rauschenbeute, "Cold Atom Physics Using Ultra-Thin Optical Fibers: Light-Induced Dipole Forces and Surface Interactions"
Phys. Rev. Lett. 99, 163602 (2007).